DISSERTATION

INSIGHTS AND METHODOLOGIES IN WALL-BOUNDED TURBULENT CHANNEL FLOWS

Submitted by

Harshit Mishra

Department of Civil and Environmental Engineering

In partial fulfillment of the requirements

For the Degree of Doctor of Philosophy

Colorado State University

Fort Collins, Colorado

Fall 2024

Doctoral Committee:

Advisor: Subhas Karan Venayagamoorthy

Timothy K Gates
Pierre Y Julien
Elizabeth Barnes

ABSTRACT

INSIGHTS AND METHODOLOGIES IN WALL-BOUNDED TURBULENT CHANNEL FLOWS

Wall-bounded channel flows are of massive interest to civil and environmental engineers due to their immense application for water supply and management. This dissertation addresses five key aspects of turbulent channel flows relevant to practicing engineers, laboratory researchers, fluid scientists, and consultants leveraging computational fluid dynamics for modeling turbulent flows.

In the first study, a device was developed and tested to enable Particle Image Velocimetry (PIV) for free surface flows. Measuring flows reliably requires that illumination provided by the laser sheet remains undisturbed. In open channel flows, introducing the laser sheet from the free surface can be necessary as the bed may be optically opaque. An oscillating free surface can further complicate maintaining an undisturbed laser sheet. This research has shown that the disturbance of the laser sheet, when introduced from the free surface, can be mitigated by introducing an improvised device called an optical coupler. The effect of the coupler on the measured velocity field was systematically studied using independent Laser Doppler Anemometer (LDA) measurements. The effect of the coupler on the measured velocity field was confined to its vicinity near the surface of the flow. The mean flow profile remains largely unaffected. Additionally, appropriate material for fabricating the coupler has been recommended by studying the relative performance of a glass and acrylic coupler. While the glass coupler measurements were closer to the undisturbed flow profile, the durability and ease of handling an acrylic coupler make it a viable alternative.

The second study is focused on ensuring fully developed flow in short laboratory flumes. Ensuring a fully developed flow is essential for any experimental or modeling study that involves wall-bounded flows. Flow development in pipes has been extensively studied, and empirical relationships have been widely published. Recently, similar studies on open channels have revealed

that the entrance length in laboratory flume is $\approx 100h$, where h is the depth of the flow. Such a prescription renders most laboratories unfit for experimental work. Further, the inlet configuration in the flume can also hamper flow development, even after the length requirements are met. In this study, we develop a methodology to obtain developed flow in short channels by modifying the inlet and tripping the boundary layer. Further, we also provide a robust, rapid test to confirm if the flow is fully developed using Direct Numerical Simulation (DNS) datasets. The proposed method is validated using flume experiments for flows with friction Reynolds number $Re_\tau \sim 1500 - 3000$. Against the current prescription, we show that it is possible to obtain fully developed profiles within a distance of $\approx 20h$ from the inlet.

In the next (third) study, we leverage the DNS data for closed channel flow for a range of friction Reynolds Number ($Re_\tau \sim 180 - 5000$) to develop a new One Point Friction Velocity Method (OPFVM) to calculate friction velocity U_* in terms of free-surface velocity U_m, flow depth h and kinematic viscosity ν for smooth wall-bounded flows. In contrast to prevalent methods that require several cumbersome near-boundary measurements to obtain friction velocity, the OPFVM relies on a single easy-to-measure free-surface velocity measurement. The formulation obtains friction velocity for a closed channel flow (CCF) DNS regime with $Re_\tau = 10049$ and on four open channel flow (OCF) DNS regimes with $Re_\tau \sim 180 - 2000$. The same formulation was then experimentally verified in our laboratory. To avoid being prescriptive, a sensitivity analysis was performed to determine the permissible variation in U_m to restrict the error in estimated U_* to 2%. The relationship between the depth-averaged velocity U_b and the maximum free-stream velocity U_m is also explored using the DNS datasets and an approximate relationship between U_b and U_m is proposed. With advances in remote sensing technology that enables free-stream velocity measurements, this method extends the potential to measure even the friction velocity remotely.

Computational Fluid Dynamics (CFD) is an essential tool for analyzing fluid flows. The $k - \epsilon$ model is a turbulence model used in Raynold-Averaged Navier-Stokes simulations to close the Reynolds stress terms. The empirical constants used in $k - \epsilon$ model were obtained using experiments conducted at low Reynolds numbers several decades ago. In this study, we revisit the

turbulent viscosity parameter C_μ, based on the stress-intensity ratio $c^2 = \frac{|\overline{uw}|}{k}$. Here, $\overline{|uw|}$ and k are the absolute values of the Reynolds stress and turbulent kinetic energy, respectively. Through *a-priori* comparisons, we find that the widely accepted value of $C_\mu = 0.09$, does not agree with the latest DNS and experimental datasets of wall-bounded turbulent planar flows. Therefore, a new value is suggested by averaging c^2 in the equilibrium region, where the production ($\mathcal{P}$) of k is within 10% of the dissipation rate(ϵ), and consequently, $c^4 \approx C_\mu$. We evaluate flows up to friction Reynolds number $Re_\tau \approx 10000$ and find that with increasing Re_τ, C_μ approaches a value of 0.06, which is 50% lower than the prevalent value of 0.09. Finally, we perform an *a-priori* test with the new (proposed) value of $C_\mu = 0.06$ to show that the estimated turbulent viscosity ν_T for wall-bounded flows is in much closer agreement with the exact (DNS) values than when ν_T is estimated using $C_\mu = 0.09$.

The final study develops a new scaling law for wall-bounded turbulent flows. This formulation eliminates all arbitrary constants and depends only on physical parameters, namely, the free-stream velocity U_m, the friction velocity U_*, the kinematic viscosity ν, and the distance from the wall z. This is a significant step towards describing the velocity profile using these pertinent parameters.

ACKNOWLEDGEMENTS

As I present this dissertation for examination and approval by my committee, I am short on words to express my gratitude to the amazing people I have met during my Ph.D. program. First of all, I would like to express my immense gratitude to my advisor, Prof S Karan Venayagamoorthy, whose mentorship has transformed my life in both tangible and intangible ways. Prof Karan has supported me wholeheartedly in this journey through thick and thin and provided valuable guidance at every critical step of my Ph.D. It is through his excellent mentorship that I feel confident in discussing challenging problems and have a strong foundation in fluid mechanics. Prof Karan has gone out of the way to ensure that I remain funded during my Ph.D. and provided me with unique opportunities to showcase my abilities. Prof Karan's outstanding teaching methodology has greatly helped me improve my teaching skills so that I am well equipped for the career path I have chosen. His commitment to excellence in research, to the welfare of his students, and his humility to accommodate new perspectives have greatly inspired me and have made my experience at CSU a life-changing one. I am extremely grateful to Prof Karan for admitting me to his research group and providing this invaluable experience.

I am indebted to my committee members, Prof Tim Gates, Prof Pierre Julien, and Prof Elizabeth Barnes. They have kindly consented to be on my doctoral committee despite their immensely busy schedules and research commitments. Their guidance and support have been invaluable assets. My classes with Prof Tim Gates and Prof Pierre Julien have significantly widened my perspective and provided me with profound insights into open-channel flows and river mechanics.

Further, I am grateful to my colleagues at the Environmental Fluid Mechanics Laboratory, Joe Pugh, Dr. Jessica Baker, Dr. Dapo Asaperi, Dr. M.R.Klema, Daniel Sanchez, Kasun Sahabandu, Joey Sinclair, Kiarash Nayeb Pashei, Khem Bhattarai, and Faisal Al-Sultan for their continual support and understanding. These are some of the relationships that would last a lifetime.

The support from the Department of Civil and Environmental Engineering has been remarkable. I am grateful to Susheela Mallipudi for her consistent and active support as a graduate advisor.

I am thankful to Todd Atedero, who has always supported me with any of the requirements I had regarding the experimental setup. I would also like to thank Steve Johnson and Justin Hollis from the mechanical engineering department for their help in fabricating experimental tools. Further, the dean's office at the College of Engineering gave me plentiful opportunities to develop as a good teacher. I am thankful to Bert Vermeulen, who steadily mentored me in harnessing my teaching abilities and has been a consistent advocate of mine.

More importantly, I would like to thank my parents, my brother, and everyone in my extended family who shared all the joys with me wholeheartedly and trusted my abilities to pursue a challenging course. I am also grateful to my Sanskrit fraternity, which has provided me with avenues to take a break from my research and discuss some exciting intricacies of the Sanskrit language. Finally, I thank the Almighty for providing me with the wisdom and the intellect to pursue a noble profession of engineering, teaching, and research.

There are so many people whose names I have certainly missed in this acknowledgment. I greatly acknowledge their support throughout this endeavor.

DEDICATION

This thesis is dedicated to the all-powerful Almighty whose magnificent creations continue to humble us with its expanse, complexity, and perfection.

TABLE OF CONTENTS

LIST OF TABLES

LIST OF FIGURES

LIST OF ACRONYMS

ADCP	=	Acoustic Doppler current profiler;
ADV	=	Acoustic Doppler velocimetry;
BSA	=	Burst spectrum analyzer;
CCF	=	Closed channel flow;
CFD	=	Computational Fluid Dynamics;
DNS	=	Direct numerical simulation;
DPSS	=	Dual pumped solid-state;
LDA	=	Laser doppler anemometry;
LSPIV	=	Large scale particle image velocimetry;
OCF	=	Open channel flow;
OPVFM	=	One point friction velocity method;
PIV	=	Particle image velocimetry;
RANS	=	Reynolds averaged Navier Stokes;
SNR	=	Signal-noise ratio;
TKE	=	Turbulent kinetic energy; and
ZPG	=	Zero pressure gradient

LIST OF SYMBOLS

The following symbols are used in this dissertation:

A	=	Cross-sectional area (m^2);
B	=	Townsend and Perry's constant;
b	=	Width of the flume (m);
C_μ	=	Turbulent viscosity parameter;
c^2	=	Stress-intensity ratio $\overline{uw}/k$;
d	=	Diameter of the pipe (m);
δ_ν	=	Inner length scale ν/U_*;
ϵ	=	$100 \times \left(1 - \frac{U_{*est}}{U_*}\right)$ Percentage error in U_* estimation;
ϵ	=	Dissipation rate of k;
ϵ_{loglaw}	=	Error in U_* calculation using log-law method with respect to OPFVM;
$\epsilon_{avgshear}$	=	Error in U_* calculation using average shear stress method with respect to OPFVM;
h	=	Flow depth (m);
κ	=	Von Karman's factor;
k	=	Turbulent kinetic energy;
k_{max}	=	Maximum wave number (m^{-1});
L_e	=	Entrance length (m);
L_x	=	length scale (m);
μ	=	Dynamic molecular viscosity kg/ms;
n	=	Manning's coefficient;
ν	=	Kinematic molecular viscosity m^2/s;
ν_T	=	Turbulent viscosity m^2/s;
ν_T^+	=	Non-dimensional turbulent viscosity ν_T/ν;
$\mathcal{P}$	=	Production rate of k;

P = Wetted perimeter (m);

Q = Flow rate (m^3/s);

R = A/P Hydraulic Radius (m);

Re_τ = $\frac{U_* h}{\nu}$ Friction Reynolds number;

Re_b = $\frac{U_b h}{\nu}$ Bulk Reynolds number;

Re_m = $\frac{U_m h}{\nu}$ Reynolds number based on free-surface velocity U_m;

ρ = Density (kg/m^3)

S_0 = Bed slope;

S_e = Equivalent slope;

σ = Standard deviation in velocity profiles;

σ_{max} = Maximum standard deviation in velocity profiles;

τ_b = Bed shear stress (N/m^2);

τ_{avg} = Average bed shear stress (N/m^2);

τ_{local} = Local bed shear stress (N/m^2);

u_{ac} = Velocity measured with acrylic-coupler in place;

u_{nc} = Velocity measured with coupler in place;

u_{nc} = Velocity measured with no coupler in place;

u_{gc} = Velocity measured with glass-coupler in place;

U = Streamwise mean velocity (m/s);

U_* = Local friction velocity (m/s);

U_b = Depth averaged velocity (m/s);

U_f = Velocity scaling function (m/s);

U_m = Maximum free-surface velocity (m/s);

U^+ = $\frac{U}{U_*}$ Scaled streamwise mean velocity;

u = Streamwise fluctuations (m/s);

u^+ = $\frac{u}{U_*}$ Scaled streamwise fluctuations;

$\overline{uw}$ = Reynolds shear stress (m^2/s^2);

$\overline{uw}^+$ = $\frac{\overline{uw}}{U_*^2}$ Scaled Reynolds shear stress;

ς = $\frac{z}{h}$;

W = Wake function;

w = Wall-normal fluctuations (m/s);

w^+ = $\frac{w}{U_*}$ Scaled wall-normal fluctuations;

x = Streamwise coordinates (m);

z = Wall-normal coordinate (m); and

z^+ = $\frac{zU_*}{\nu}$ Scaled z-coordinate.

Chapter 1

Introduction

1.1 Motivation

Wall bounded turbulent flows are ubiquitous in our environment. Some examples of wall-bounded flows are atmospheric boundary layer flows, flows in natural and artificial conduits, flows over flat-plates, etc. Most processes responsible for life, whether chemical, physical, or biological, occur in the near-wall region. However, due to the imposed no-slip condition by the wall, sharp gradients and anisotropy are introduced in the flow (Townsend, 1951; Bradshaw, 2013), which makes their understanding difficult. Additionally, the nature of the surface of the wall interacting with the fluid can have a pronounced effect on the flow (Raupach et al., 1980; Coleman and Alonso, 1984). The fluid is often laden with particles, ranging from clay ($\sim O(10^{-6})$) to boulders ($\sim O(10^{1})$). While the smaller particles are passive, the larger particles interact actively and affect the flow (Berk and Coletti, 2020; Brandt and Coletti, 2022). The natural flows result from these interactions occurring simultaneously, along with many other chemical, biological, and physical processes. These processes, driven and controlled by turbulence, have implications on water conveyance, drinking and irrigation water quality, pollutant diffusion, operation of hydraulic structures, stability of river works, flood control, power generation, bridge stability, and, possibly, every aspect of life on this planet. Significant research is required to understand them involving a multi-disciplinary approach to improve our lives sustainably.

Water is an essential component of life among two key fluids on earth. In nature, it sustains life through various processes, as discussed above, that allow water to change its form, transport certain materials, catalyze or retard reactions and cause changes in physical structures. Water, as a resource, has been managed since the advent of civilization. Numerous interventions can be observed along the rivers with different time stamps. An interesting publication by Viollet (2017)

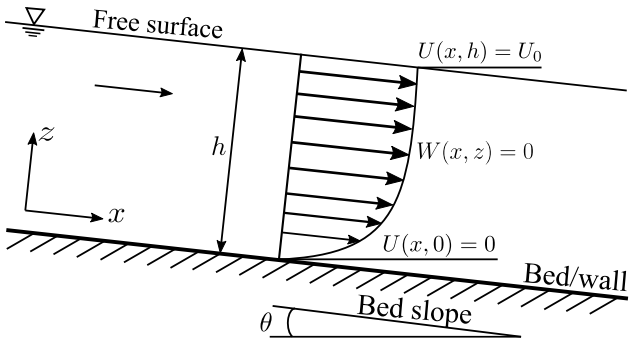

Figure 1.1: A typical open channel flow model used for analysis in civil engineering

gives an account of the developments in water engineering over the last 5000 years [1]. The main reason for studying these processes from an engineering perspective is to reveal underlying dynamics that help better model and engineer water systems. There are numerous ways in which water engineering has improved our lives. For example, urbanization is enabled by efficient conveyance of drinking water and wastewater; dams are constructed to store the water, which in turn is distributed by the pipe network; post-consumption, the wastewater carries pollutants that advect and diffuse on their way back to natural streams that also transports heavy vegetation by rare events like floods and cyclones on the one hand, and sediments on the other.

There are three types of canonical wall-bounded flows: turbulent boundary layer (TBL), pipe flows, and channel flows. Civil and hydraulic engineers usually encounter channel flows, further classified as open channel flow (OCF) and closed channel flows (CCF). OCF, as shown in Fig 1.1, is distinguished by the free surface on top, which is subject to atmospheric pressure. The difficulty in solving problems in open channel flow arises because the position of the free surface can change with respect to space and time. The discharge, depth of flow, bed slope and, water-surface elevation are interdependent (Chow, 1959a). The main driving force is gravity. Flow in sanitary sewers, drainage channels, canals, and rivers are a few examples of OCF (Fig 1.1). In this dissertation, the focus is on the channel flows, which are the prime focus of civil engineers. To effectively utilize the water resources available to us, an engineer's objectives are to ensure adequate quantity of water of acceptable quality at an affordable price. For this purpose, they require energy to treat and transport

[1]The original book was published in French. The translation in English has been referred to here.

it. The loss of energy, due to resistance in the flow, is therefore, a major cost factor. The dynamics controlling the flow resistance occur very close to the wall where the velocity changes rapidly (steep gradient), the turbulence is anisotropic (directional), measurements are difficult, and fluid particles experience maximum stress. Thus, effective estimation of shear stress, a key parameter to quantify resistance, is critical to achieving better design processes. Thus, one major objective of this dissertation is to improve the shear stress estimation for smooth channel flows in laboratory and field settings. Usually, a dissertation focuses on an experimental or a computational study. However, in this dissertation, a contribution has also been made in the domain of computational fluid dynamics (CFD) because of its growing relevance in hydraulic engineering.

1.2 Underpinning philosophy of this dissertation

The future challenges faced by hydraulic engineers will need a synergy of different methodologies that have been developed in recent years. The leaders in the profession should have a strong footing in the constitutive domains of knowledge and supplement them with their expertise. Hydraulic engineering has evolved to include more computational fluid dynamics, high-fidelity laboratory measurements, field measurements, and applied mathematics to further the understanding of fluid flows. While the classical approach in hydraulics engineering has been through empirical methods, there is heightened interest in understanding the flow mechanics. However, no approach is complete in itself. This will be evident by the following comparison between computational fluid dynamics and experimental investigations as shown in Table 1.1. Therefore, it is important to take advantage of complementing abilities. A combined analysis leveraging CFD and experiments is called composite modeling. The term composite modeling was coined by the Hydralab consortium to represent the integrated and balanced approach of field measurements, physical modeling (laboratory measurements), and numerical simulations (Frostick et al., 2011; Muste et al., 2017). The process and goals of composite modeling are shown in Fig 1.2.

Thus, in this dissertation, contributions are made to field methodology, laboratory measurements, and RANS modeling using direct numerical simulation (DNS) data. Further, a laboratory

Table 1.1: Comparative assessment of CFD and experiments

Parameter	**CFD**	**Experiments**
Physics	Reveals physics based on mathematical model	Can reveal actual physics
Cost	Low : Comprises of license and computational infrastructure	High : Instruments are expensive
Error	Is caused due to discretization, grid size, and inadequacy of the model	Caused due to instrument, user, and uncontrolled factors
Detail	High : Every parameter can be obtained up to the resolution of the grid	Low : Limited by resolution and access of the instrument
Repeatability	Easy	Requires same effort as running a new experiment.
Modification	Easy and quick	Requires re-run
Scale	Scaling is possible with little adjustments	Expensive to conduct field-scale but reveals additional system dynamics

device has been developed, and the measurements have been verified using an independent laboratory instrument. Finally, a mathematical scaling law has been developed using the fundamentals of hyperbolic geometry and tested using DNS and experimental data.

1.3 Layout of the dissertation

This dissertation has been divided into seven chapters. Chapter 1 details the motivation, philosophy, and layout of the dissertation. The next five chapters are the studies conducted on different aspects of wall-bounded turbulence.

- Chapter 2 describes a new laboratory device developed to study wall-bounded flows using Particle Image Velocimetry (PIV) that allows the laser sheet to be passed into the flow through the free surface.
- Chapter 3 describes a method to obtain fully developed flows in short laboratory flumes.
- Chapter 4 details a new method to estimate friction velocity in field and laboratory settings.
- Chapter 5 provides an improved Reynolds Averages Navier Stokes (RANS) simulation model for modeling wall-bounded turbulent flows.
- Chapter 6 discusses a new universal scaling relationship for wall-bounded flows.

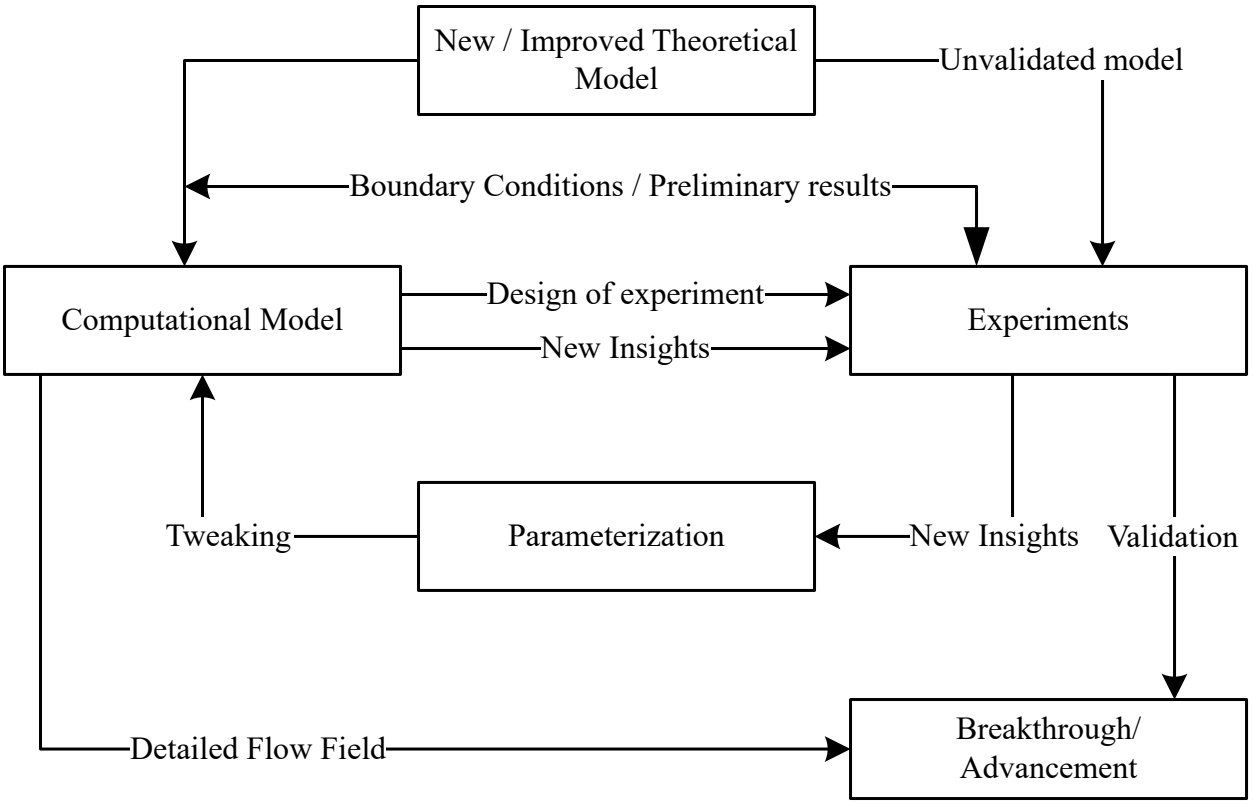

Figure 1.2: The flowchart explaining composite modeling with each component receiving feedback and direction

Since each of the studies has a distinct literature, the pertinent literature review is incorporated in each of the respective chapters. The findings of the dissertation are summarized in chapter 7 along with directions for future study.

1.4 Conclusion

This chapter highlights the motivation and the underpinning philosophy and outlines the lay-out of this dissertation. It brings out the synergy between fluid mechanics and hydraulics, CFD and experiments, theory and data. The philosophy of this dissertation can be summarized in the words of the famous hydraulician Hunter Rouse, as, *"One can continue to hope, if not predict, hydraulics will continue to widen its break with pure empiricism, which long since reached a point of diminishing return, and to strengthen its with physical analysis, for the latter is still unlimited in possibilities."*

Chapter 2

Enabling Particle-Image-Velocimetry measurement for Free Surface Flows[1]

2.1 Introduction

In the last two decades, Particle Image Velocimetry (PIV) has become an essential tool to obtain velocity fields in various types of fluid flows (Adrian, 1991; Adrian and Westerweel, 2011; Westerweel et al., 2013; Raffel et al., 2018). Among the three main methods used in experimental fluid dynamics (i.e., hot-wire anemometry, laser Doppler anemometry (LDA), acoustic Doppler velocimetry (ADV), and PIV. PIV has shown a steady rise in its application and usage since the late 1990s (Westerweel et al., 2013). Each experimental method has its own strengths. For example, hot-wire anemometers can be used to measure flows at low turbulent intensity, especially near walls and obstacles. The LDA effectively measures very high turbulent fluctuations over a long period. However, both of these instruments are limited in that they can only take point measurements. PIV overcomes this limitation with the ability to simultaneously quantify velocities at multiple points within the flow field. It has enabled scientists to analyze complex flow structures spread over different length scales, and has also aided the visualization of flow at very small time scales.

A PIV system requires optical access along two, preferably orthogonal, planes (Adrian and Westerweel, 2011; Raffel et al., 2018). A glass-bottom flume is usually recommended for PIV measurements, and many experimental studies have been conducted using this approach (Prooijen et al., 2000; Westerweel et al., 2013; Cameron et al., 2020; Rousseau and Ancey, 2020; Zampiron et al., 2021). However, emerging trends in experimental hydraulics necessitate modifications to the channel bed, such as the introduction of roughness, gravels, vegetation, sand grains, and sediments. Additionally, opportunity exists for studying the flow field around hydraulic structures such as

[1] A substantial part of this study will be submitted to the journal *Experiments in Fluids* with co-authors J.E.Pugh, M.R.Klema, and S.K.Venayagamoorthy.

weirs and gates (Shayan et al., 2021). These modifications curtail the optical passage of the laser sheet through the bed. Therefore, it becomes necessary to bring the laser sheet through the free surface. Since the free surface causes alternate bands of high and low intensities (see Fig 2.1) in the optical sheet, flumes need an optical device to transmit the laser sheet and allow it to overcome the disturbance caused by surface fluctuations. If the images are taken through the free surface, surface fluctuations shield the tracer particles. In that case, a coupler is required to prevent the shielding of tracer particles. The latter issue requires further investigation.

Since PIV is used to study a variety of problems in fluid dynamics, researchers have used improvised devices for their specific requirements and evaluated them for safety, effectiveness, and uncertainty (Landreth and Adrian, 1988; Gurka et al., 1999; Foucaut and Stanislas, 2002; Schrijer et al., 2006; Wilson and Smith, 2013). However, the methods to pass the laser sheet through the free surface have been either very costly or are makeshift arrangements whose effects on the flow are not documented rigorously.

One way of avoiding passing the laser sheet through the free surface is by leveraging downstream optical access (Wang et al., 2018). However, the downstream of the flume is often used as a control, and as such, a translucent material cannot be used. Slightly more leverage is available while using a stereoscopic PIV setup. In this scenario, the two cameras can be aligned at an angle to the illuminated plane, and the same wall may be used for providing optical access to both the laser sheet and the camera (Amir et al., 2014; Cameron et al., 2017). The introduction of the coupler from the free surface creates an intrusive effect on the flow. The extent of the influence of the coupler on the flow will depend on the coupler dimensions relative to the overall dimensions of the flow being analyzed. Even though the effect may be minimal, it is necessary to quantify the effect of the coupler by comparing flow measurements made with the optical coupler influencing the flow to measurements of the undisturbed flow. These flow measurements must be made using an independent, non-intrusive flow measurement device.

In this study, we have introduced a device called a 'coupler' and systematically studied its effect on the mean flow profile across different flow regimes. We also investigate couplers constructed from two optically similar materials to arrive at a suggestion of the preferred material.

2.2 Coupler Design

Introduction of the laser sheet directly into the free surface results in alternate dark and light bands due to the optical refractions generated by fluctuations in the free surface as shown in Fig 2.1a. To overcome this challenge, we designed a coupler with streamlined ends, as shown in Fig 2.2a. The design was based on the length of the laser sheet, feasibility in fabrication, and an ability to resist shear when in suspension, as well as vibrations caused by momentum flux from the flow. We fabricated two couplers using two unique materials, glass and acrylic. Manufacturing of the glass coupler requires high expertise and thus, was fabricated by a professional (see Fig 2.2b). The upstream and downstream corners were streamlined to avoid flow separation. The acrylic coupler represents a more cost-effective option and was manufactured in-house using stock acrylic. The couplers are mounted on the frame of the flume and suspended using threaded rods. As the flow depth changes, the couplers can be moved in either direction using mounting screws.

2.3 Experimental Setup

The experimental setup is shown in Fig 2.3. It comprises three instruments. The flow section as measured by the two instruments is shown in Fig 2.4.

2.3.1 Flume and Seeding

The study was conducted using a recirculating Armfield (S6MKII) 5 m long tilting flume with a sediment loop. The width (b) of the flume is 300 mm and can accommodate flow depth (h) up to 350 mm. The bed of the flume is made of high-precision steel, representing a smooth surface. The flume has glass walls on the sides, which permit the use of non-intrusive optical devices such as an LDA.

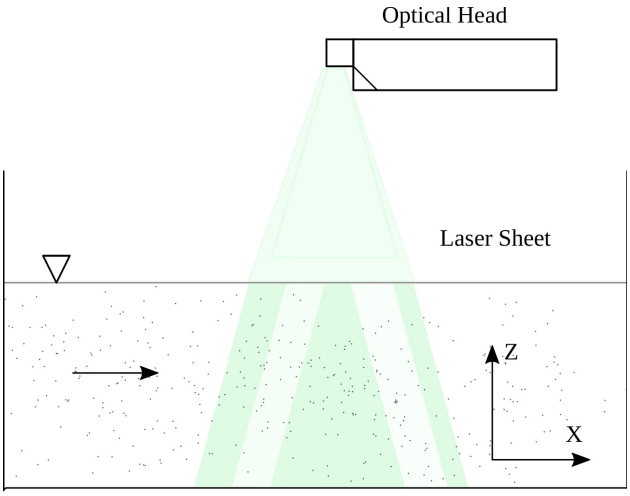

(a) Illustrative depiction of the dark and light bands of light within the laser sheet due to the optical refraction created by the oscillations of the free surface (surface waves) on the laser sheet.

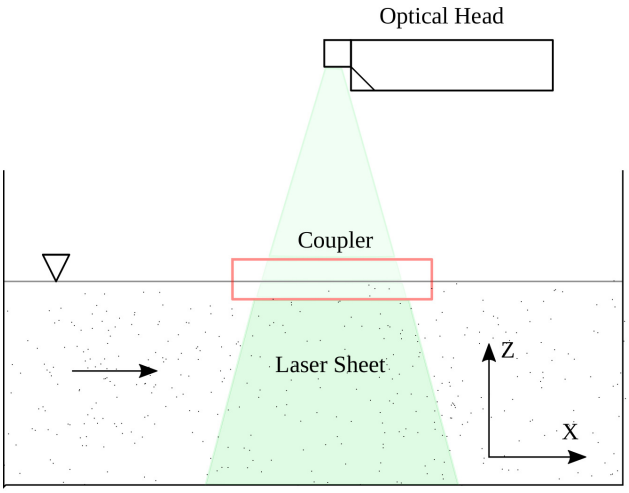

(b) Depiction of the uniform laser sheet created with use of the coupler. The coupler removes the fluctuations in the light-sheet caused by the free surface.

Figure 2.1: Effect of coupler on laser sheet

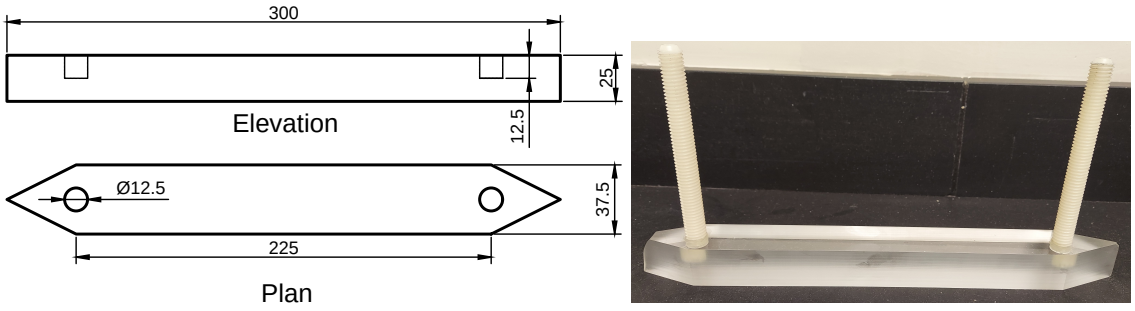

(a) Coupler dimensions (in mm) **(b)** Machined Glass Coupler

Figure 2.2: The dimensional details of the coupler have described in the image on the left. Threaded plastic rods are glued in the grooves to allow screw-mechanism as shown in the figure on the right.

The flow was seeded using 20 μm spherical, uncoated polyamide particles. In this study, PIV and LDA were used to evaluate the performance of the two couplers described in section 2.2. The different components of the PIV and LDA apparatus are described in the following subsections.

2.3.2 Laser Doppler Anemometer (LDA)

The 2D - LDA setup is provided by `Dantec Inc.`. It has a dual-pumped solid-state (DPSS) laser connected to a photo-multiplier assembly that contains the probe. The frequency shift is processed by a Burst Spectrum Analyzer (BSA) connected to a computer. The DPSS laser emits two beams of wavelength 513 mm and 495 mm, respectively. Each beam has a maximum power of 120 mW, split by the photo-multiplier into four total beams and then passed into the flow using a probe. The laser is connected to the Bragg cell that provides the Bragg frequency shift of 40 MHz. The beam has a focal length of 398.4 mm, beam diameter of 1.35mm, and beam spacing of 38.3 mm. The beam intersection angle is 20°. An *iSEL*-s8 traverse controller moves the probe in the X-Z plane with an accuracy of ± 0.1 mm. The operational arrangement of the LDA system is shown in Fig 2.3b. For details on operation of an LDA system refer to Durst et al. (1981); Muste et al. (2017).

2.3.3 Particle Image Velocimeter (PIV)

The *LaVision* PIV arrangement uses a *Photonics* DM 30 dual head Nd: YLF DPSS, 527 nm, green laser system. It has a laser controller connected to the laser head and can operate at a

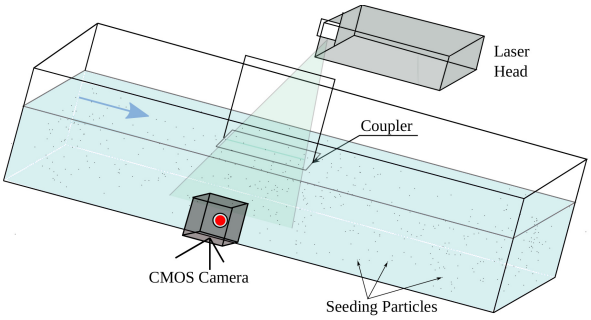

(a) Experimental setup of the PIV with the laser sheet passing through the coupler

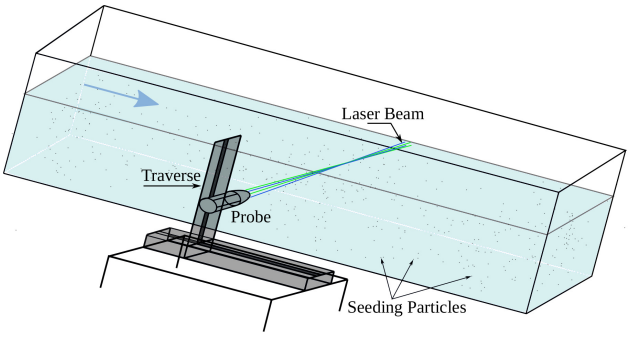

(b) Experimental setup of LDA system with four laser beams

Figure 2.3: Experimental Setup

frequency of up to 10 kHz, delivering 100 mJ of energy per pulse. The laser head has been mounted above the flume (see Fig.2.3a). The laser sheet is directed into the flume using a 90°mirror and a 10 mm lens. The length of the laser sheet at the bed is 250 mm. The images are captured using a Phantom VEO 340 L camera (4 MP, monochrome, 800 fps (Hz)) that uses a 60 mm *Nikkor* lens with a maximum aperture of f/2.8. The laser and the camera are synced using a programmable timing unit (PTU) connected to a computer. The operational arrangement of the PIV system is shown in Fig. 2.3a. The images were collected at rates calculated by guidelines based on the flow rates. Further details regarding the development and functioning of a PIV system can be found in Westerweel et al. (2013), Muste et al. (2017), and Raffel et al. (2018), and references therein.

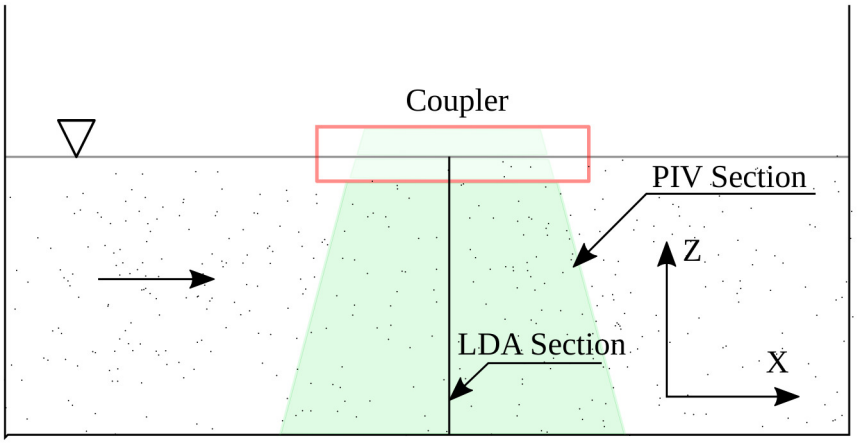

Figure 2.4: Illustration of the measured cross-section using the PIV and the LDA. The LDA along the vertical section as shown by the black line.

Table 2.1: Flow Regimes used in this study

Regime	Discharge Q (l/s)	Depth h (m)	$U_0 = \frac{Q}{bh}$ (m/s)	Slope (m/m)	$Fr = \frac{U_0}{\sqrt{gh}}$	$Re_0 = \frac{U_0 h}{\nu}$
1	28.3	0.150	0.69	0.050	0.57	5.18×10^4
2	26.8	0.085	1.14	0.050	1.25	6.20×10^4
3	20.8	0.100	0.85	0.033	0.86	5.10×10^4
4	12.5	0.106	0.45	0.000	0.44	2.79×10^4

Table 2.2: The different arrangements of instrument and coupler used in this study.

Profile	Instrument	Coupler
1	LDA	No Coupler
2	LDA	Acrylic
3	LDA	Glass
4	PIV	Acrylic
5	PIV	Glass

Table 2.3: Image Sampling Rate in PIV

Regime	Sampling Frequency (Hz)	Total Imaging Time (s)	Total Images	Time Interval (s)	Spatial Resolution (pixel $\times$ pixel)
1	800	8	6400	240	48×48
2	800	8	6400	240	64×64
3	800	8	6400	240	48×48
4	400	8	3200	240	64×64

2.4 Data Collection, Processing and Statistical Analysis

Four regimes as per Table 2.1 were run in the flume with a water temperature of 24 °C. The was flow ensured to be uniform using an improvised packing net with porous materials at the inlet. The flow was measured at a section 2.5 m downstream of the inlet, where it was found to be statistically stationary.

2.4.1 Data Collection with LDA

Three profiles, listed in Table 2.2, were obtained in each regime using the LDA . Data was processed using BSA Flow Software provided by Dantec as per configuration described in section 2.3. The data collection mode was set to 'burst' to obtain high temporal resolution and a high data rate. Measurements were taken at a single cross section for all twelve configurations for four minutes or 10000 samples, whichever is achieved earlier. The data rate fluctuated across different regimes, with higher data rates occurring in fast (supercritical/free-stream) flows and low data rates in slow (subcritical/near boundary) flows). It was ensured that the coincidence was at least 50%, even when the data rate is low. Parameters such as record length, sensitivity of photo-multiplier, and gain were optimized for data rate and coincidence as per flow requirements. The LDA measures both stream-wise and vertical velocities, however in this study only stream-wise velocities were considered.

2.4.2 Data Collection and Processing with PIV

Two profiles were obtained for each regime using the PIV arrangement listed in Table 2.2. The image rate and, subsequently, the total number of images were determined to ensure that sufficient images are available over four minutes to capture the largest scales in the flow. The measurement interval over LDA and PIV has been kept the same (240 seconds). The image rate and the total number of images are listed in Table 2.3.

Processing of PIV images was completed using the *Davis 10* software (provided by *LaVision Inc*). The images were pre-processed using the sliding background subtraction tool to remove

any background features. This tool removes any object that is static or moves very slowly in comparison to the tracer particles. A rectangular geometric mask was applied to filter the relevant flow region for speeding up the computations.

Since we were interested only in first-order statistics, and a prior estimate of velocity was available, the images were processed using the standard time-resolved PIV operation (Adrian, 1991; Westerweel et al., 2013). The pixel displacement estimated the spatial resolution for each profile and accordingly was set for the analysis (see Table 2.3). It was ensured that the tracing particle did not move more than a quarter of the interrogation window between two correlated frames. The standard time-resolved PIV operation uses the standard cross-correlation method, where each image has a single frame, and subsequent images are used for obtaining the velocity vectors. The cross-correlation is done by 75% image overlap.

The velocities were measured in the region around the vertical LDA section and averaged using techniques stated in the next section.

2.4.3 Average Velocity

The assessment of the coupler effect is made by comparing the mean velocity profiles obtained by either of the instruments. The mean velocity profile for LDA is obtained using an ensemble average over four minutes at each point. The point mean velocity, $< u_z >$, is obtained by taking the average over the duration of the measurement.

$$< u_z >= \sum_{i}^{n} u_i \tag{2.1}$$

The ensemble-average, depth-averaged velocity, $\overline{U}$ is defined

$$\overline{U} = \frac{\sum_0^h < u_z >}{h}, \tag{2.2}$$

where h is the flow depth. The velocity profile obtained using PIV along the same section has spatial and temporal range. A cross-section is sampled at a frequency of 400Hz/800Hz (see Table

2.3, and eight sets of images were taken, each for one second. The eight sets were evenly spread over four minutes. The images are processed using the cross correlation technique as discussed in the previous section and suggested by Muste et al. (2017) and Raffel et al. (2018). The ensemble average is obtained as in Eq. 2.1. This velocity is different from the mean velocity U_0 listed in Table 2.1, as depth-averaging is not an exact integral. U_0 is calculated by dividing the discharge Q by the cross-sectional area of the flume

$$U_0 = \frac{Q}{bh}, \tag{2.3}$$

2.4.4 Standard Deviation

The standard deviation for each point velocity measured by the LDA was calculated using Eq (2.4).

$$\sigma_z = \sqrt{\frac{1}{N-1}\sum_{i=1}^{N}|u_i - < u_z >|^2} \tag{2.4}$$

The standard deviation obtained for LDA measurements is strictly over time. However, in PIV measurements, the velocity field is obtained by cross-correlation of several images; see Table 2.3. The velocity field obtained is averaged over a cross-section to get the first and second-order statistics using Eq (2.3) and Eq (2.4).

2.4.5 Normalization

The profiles are normalized by the average velocity $\overline{U}$ obtained using LDA as per Eq. (2.2).

The distance from the bed has been normalized using the total depth h. The standard deviation σ in each profile has been normalized using the maximum standard deviation σ_{max} in each profile. This normalization factor was chosen to assess behavior across the profile in a particular regime.

2.5 Results

2.5.1 Effect of the coupler evaluated using LDA

Mean Velocity Profile

The normalized mean velocity profiles obtained by averaging methods stated in section 2.4 are shown in Fig. 2.5 against the normalized depth. It can be seen that all the profiles follow the established boundary layer profile and the measurements by all instruments are in close qualitative agreement with each other. However, deviations from the accepted profile are seen in Regime 4, in the region very close to the coupler, which will be discussed in section 2.6.

Standard Deviation

The standard deviation is a useful tool to measure the variability in the measurements. In the figures 2.7 and 2.9, the standard deviation is plotted against the depth. The trend in standard deviation in LDA measurements is consistent across the regimes. The standard deviation is highest near the boundary, is minimum close to mid-depth, and then increases marginally towards the surface. The higher deviation towards the surface is explained by the existence of surface fluctuations and intrusion of the coupler. Higher velocities near the surface overcome the boundary condition imposed by the coupler and therefore, even in the presence of a coupler, standard deviation remains lower than the near-bed region.

Performance of couplers

Since LDA measurements are possible without a coupler, the deviation from the mean velocity profile obtained without using the coupler is calculated using Eq. (2.5) and is plotted in Fig 2.6.

$$\%\text{Difference} = \left(1 - \frac{u_{\text{coupler}}}{u_{\text{no coupler}}}\right) \times 100 \tag{2.5}$$

It can be seen that the glass coupler performs better than the acrylic coupler in all regimes, although the performance is only marginally better.

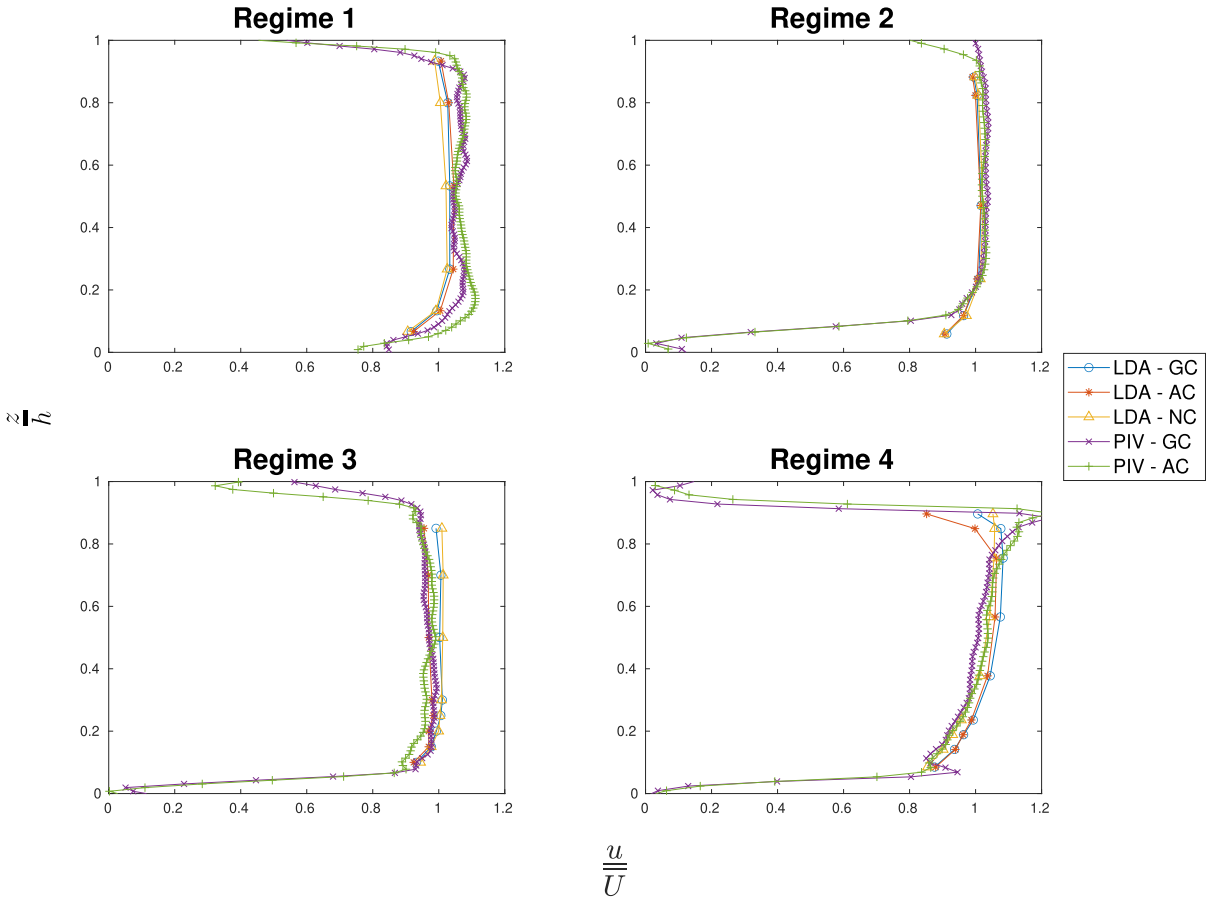

Figure 2.5: Illustration of mean velocity profiles measured using the PIV and the LDA with configurations as per Table 2.1

2.5.2 Relative Performance of Couplers in PIV

In order to choose an appropriate material for designing a coupler, it is important evaluate the relative performance. Hence, we choose here to further evaluate the relative performance of glass and acrylic couplers for PIV measurements by computing the deviation of measurements taken using acrylic coupler as compared to that of glass coupler. The aim is to evaluate the agreement of the two couplers using a similar relationship as Eq (2.5).

$$\%\text{Difference} = \left(1 - \frac{u_{ac}}{u_{gc}}\right) \times 100 \tag{2.6}$$

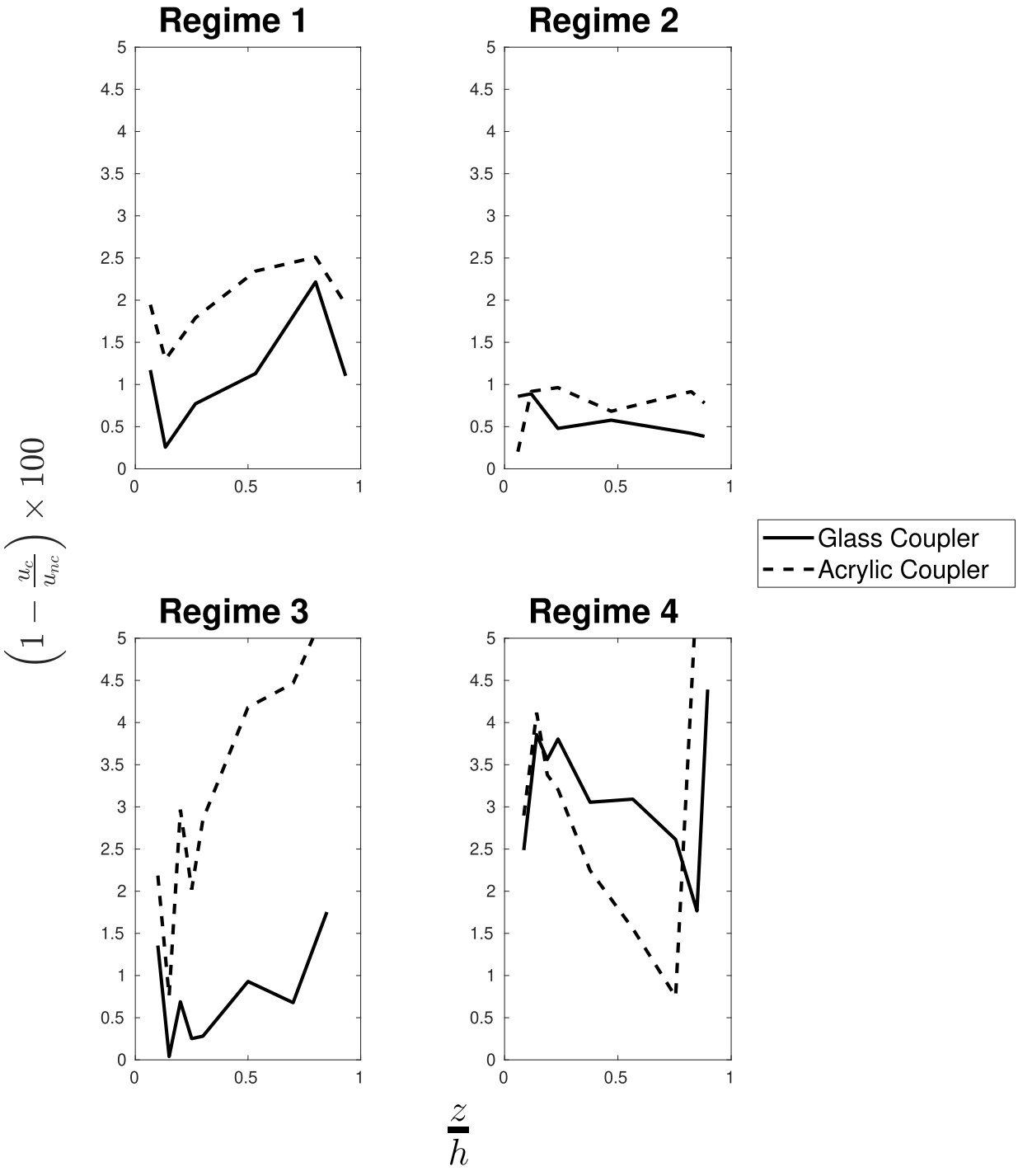

Figure 2.6: Plot of the deviation observed in velocity measured using LDA with each type of coupler placed in the flow.

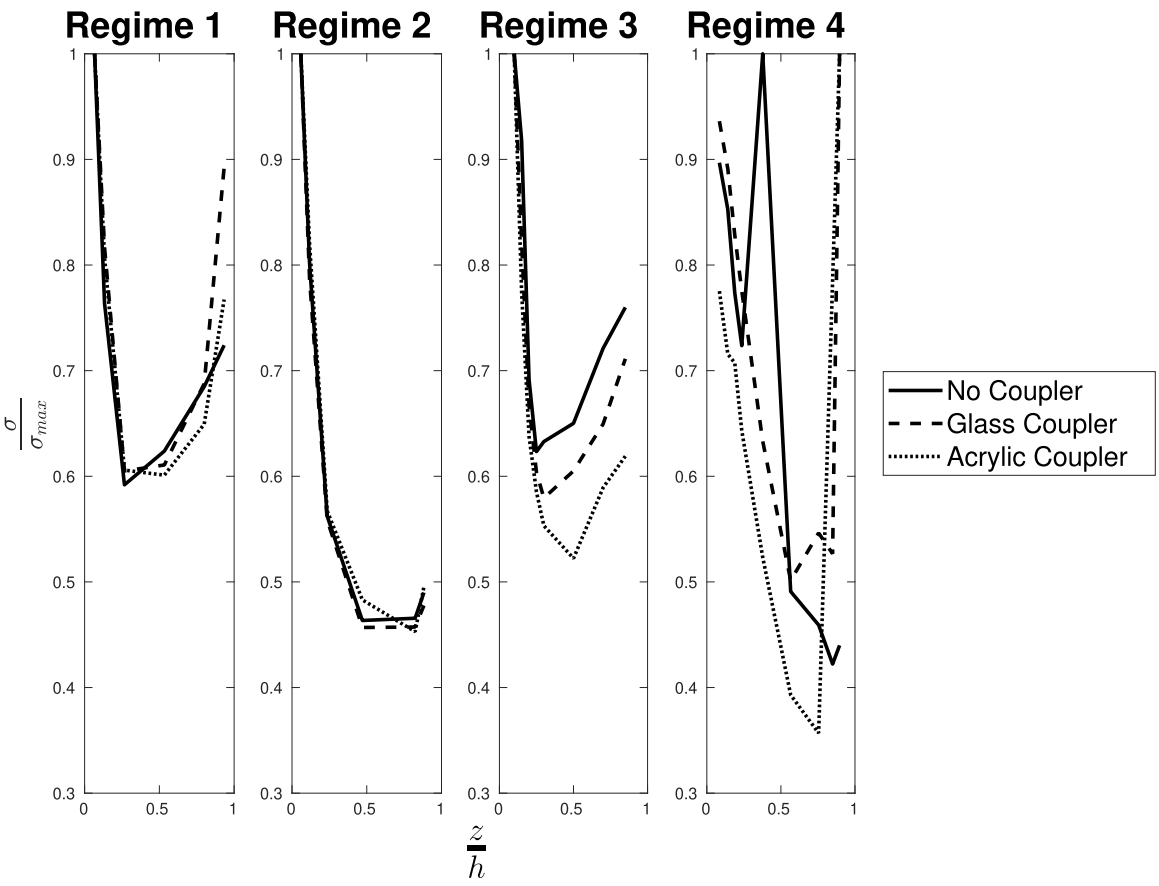

Figure 2.7: Standard Deviation of velocity measured by the LDA with different couplers.

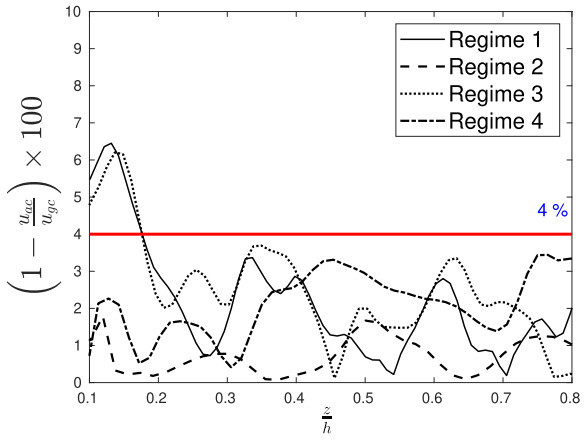

Figure 2.8: Plot of relative Performance of couplers evaluated by taking the glass coupler as a reference.

Fig.2.8 plots the percent agreement of the PIV data taken with the less-expensive acrylic coupler with the more-expensive glass coupler across the cross-section depth for each of the four regimes studied. It can be observed that most measurements lie within 2% of error and therefore, the choice of material can be made solely on the basis of cost and feasibility. The recommendations by the authors is discussed in section 2.6.

2.6 Discussion

The four regimes shown here have different levels of criticality. With these metrics, no clear trend on criticality could be obtained. However, in the PIV measurements, the criticality of the flow does affect the measurements. Even though no clear trend is seen, based on the propagation of disturbances in the flow regimes, the near bed measurements are most unreliable in supercritical flows, while the disturbance due to the coupler has a more considerable impact in subcritical flows.

2.6.1 Highly Subcritical Regime - Regime 1 and 4

In Regime 1 and Regime 4, the Froude Number is close to 0.5. The profile measured by the PIV reports higher velocity in comparison to that measured by LDA. The coupler behaves as a lid; therefore a slight acceleration in the flow can be expected in the section covered by the coupler. As the LDA takes only point measurements, and the minuscule acceleration is distributed across

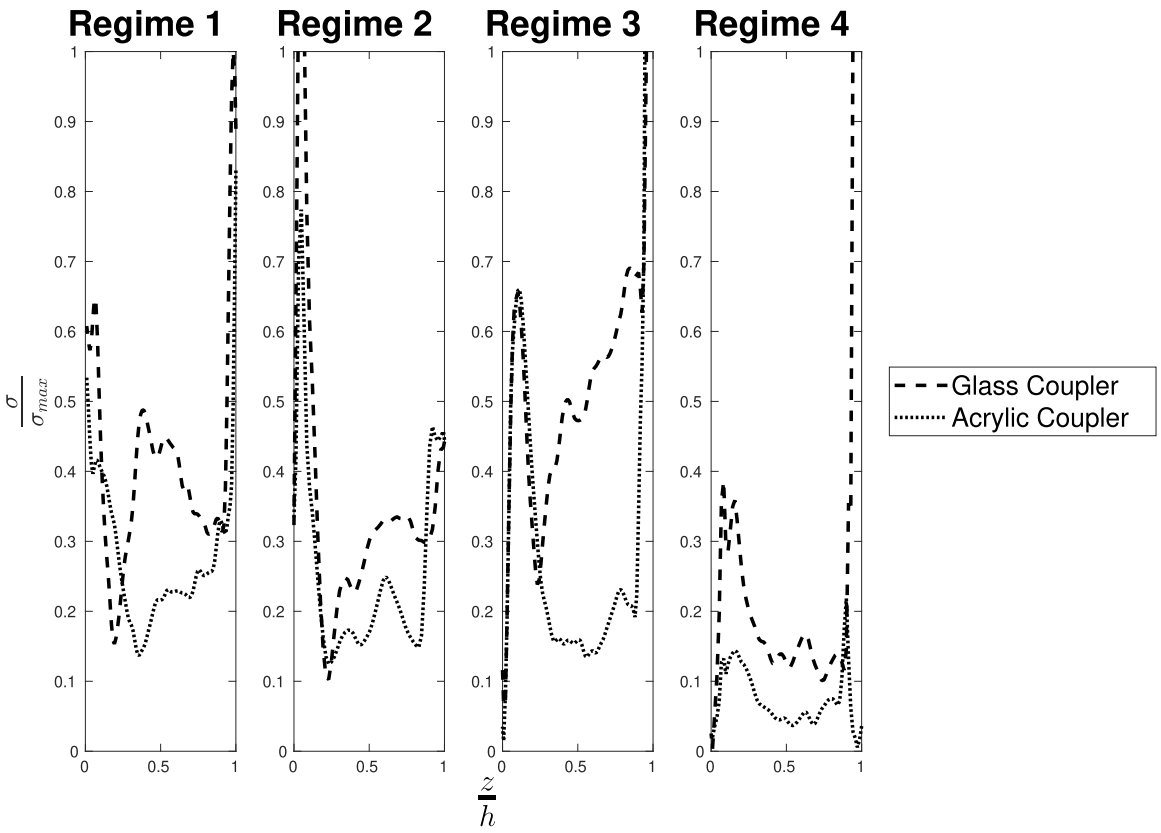

Figure 2.9: Plot of standard deviation of mean velocity profile measured using PIV with different couplers

the stream-wise section below the coupler, the PIV measurements capture the acceleration better than the LDA. However, this acceleration is within the acceptable range of 3% for most of the flow profiles. The LDA measurements show a deviation from the mean undisturbed profiles near the bed and the coupler. Fig. 2.7 suggests that the standard deviation in LDA measurements is maximum at the boundary. The performance of LDA is remarkably subdued near the bed due to insufficient sampling because of low velocities.

At high Reynolds numbers, the standard deviation in the velocity increases, which denotes increased fluctuation in the velocity field. However, at low local Reynolds Numbers, the higher standard deviations are not due to fluctuations but uncertainty in measurements.

In contrast, the measurements in the PIV system have a low standard deviation near the boundary and maximum at the surface where the effect of the coupler is most pronounced. The coupler is slightly submerged to ensure that the water surface never separates from the bottom surface of the coupler. As the Froude number decreases, a large departure from the mean profile in the PIV measurements is observed (see Fig 2.9) because the disturbance caused by the coupler travels upwards due to subcriticality. It is an example of a negatively progressive flow (Chow, 1959b). Among the two profiles measured by the PIV, the regime under the glass coupler experiences more deviation because of the glass coupler's sharp edges, which induce a greater disturbance.

The subcritical regime is most important for hydraulic engineers as most natural flows are subcritical. A good agreement among couplers instills confidence that they can be used without compromising the accuracy of the measurement. However, care must be taken when measurements are taken near the surface.

2.6.2 Effect of large gradients in PIV measurements

In a boundary layer flow, spatial gradients are significant. Accelerating particles in the interrogation window decrease the accuracy of PIV measurements. When a complete profile is measured, such particles cannot be avoided. Therefore, the near boundary measurements are complicated by the boundary flow bursting into the free-stream. In order to get reliable boundary estimates, the

resolution near the boundary must be increased. The other option is to introduce multi-pass vector processing, which increases the computational time and cost.

2.6.3 Super Critical Flow - Regime 2

In supercritical flow, the performance of LDA is optimal as the flow receives sufficient seeding across the profile. Qualitatively, excellent agreement is observed in the mean profile across all configurations. Even near the coupler, the disturbance consistently gets washed downstream as it is a case of positively progressive flow. However, the challenge lies in handling the large fluctuation in the surface, which forces deeper submergence of coupler to avoid separation. In such flows, the spatial velocity gradients are even higher, therefore, the near-bed standard deviation (see Fig 2.7, 2.9) is very high but the couplers show great agreement in their performance with respect to PIV measurements (see Fig 2.8).

2.6.4 Near - Critical Regime

The near-critical regime has instabilities that cause large fluctuation in the surface profile. Such large waves tend to separate the flow from the coupler. The mean flow profile shows an excellent agreement. However, the flow region very close to coupler are affected by the instabilities in the flow. Small disturbances generated by the coupler cause the acrylic coupler to have a larger departure from the undisturbed flow profile.

2.6.5 Effect of the material

We see that the performance of the glass coupler, both in terms of mean and standard deviation, is better than that of the acrylic coupler, except near the surface in subcritical flows. Solely on optical properties, the acrylic coupler was expected to perform better as its refractive index is closer to water (1.49), and its luminous transmittance as per ASTM D1003 is greater than 92%. On the other hand, the glass has a higher refractive index (1.57), and its luminous transmittance is in the range of 75%-92%. Since the performance of glass is better despite its inferior optical prop-

erties, we conclude that they do not affect the measurements. It is suggested that the mechanical properties of the material have a larger impact on the performance of couplers.

The performance of the glass coupler near the boundaries can be further improved by changing the design to avoid extremely sharp edges but, adequate streamlining must be ensured.

However, despite its higher error, acrylic offers practical advantages in conducting the experiments. It is durable, easy to fabricate or modify, safe to operate, and less expensive. Therefore, it offers an excellent functional alternative.

2.7 Conclusion

To tackle the problem of the fluctuating laser sheet in free surface flows when the channel bed is optically obstructed for PIV measurement, an improvised device called a coupler was used and its effect was evaluated on the mean velocity profile using LDA and PIV flow measurements. The LDA was used to obtain the velocity profile with and without the couplers. Since PIV cannot operate without a coupler, profiles with each respective coupler design were obtained. It was found that the mean velocity profiles show close agreement in most parts of the flow section except near the flow boundaries. The deviation at the boundaries was analyzed to show that the criticality of the flow affects the performance of couplers in PIV measurements. Among the two couplers used, the glass coupler showed a better performance. However, the acrylic coupler offers advantages which may outweigh the gains in accuracy by using the glass coupler. These results show that methods presented in this study for PIV measurements from the free surface can be used for accurate flow measurements in the open channel flow setting where the introduction of the laser sheet from the flow's bed surface is obstructed or opaque.

Chapter 3

Flow development in short laboratory flumes[2]

3.1 Purpose of the study

This paper has leveraged the boundary-layer tripping phenomenon to develop a methodology for laboratory experimental and modeling studies. The current state-of-art prescribes the minimum length of the channel to be $\approx 100h$, which is not feasible for many laboratories worldwide. Such a prescription may lead to the closure of many facilities. Therefore, this study provides a method to obtain fully developed flow in short channels, allowing a broader scientific community to pursue modeling and experimental fluid mechanics. Secondly, many professionals overlook the necessity of ensuring the same dynamic flow conditions when modeling fluid flows. We provide a new methodology to verify if the flow is indeed developed. Together, these two laboratory techniques will allow access to many laboratories to conduct good-quality experiments and amplify the reliability of such studies as they are appropriately benchmarked to the same set of conditions.

3.2 Introduction

Flow development in canonical wall-bounded flows has been a matter of interest for several decades. Many empirical relationships for entrance length L_e, defined as the minimum length required before the flow gets fully developed, in pipes have been published, mainly as a function of Reynolds number Re_τ. With advances in measurement technology, scientists have attempted to understand the mechanics of flow development and improve the hitherto known values for entrance length. Li (1965) provides an exhaustive review of the early works, which state that the entrance length of pipe $L_e \approx 50d$, where d is the diameter of the pipe. This value was initially suggested by Rouse (1946) and has been used in many textbooks.

[1]A substantial part of this study is submitted to the journal *Flow-Applications of Fluid Mechanics* with co-author S.K.Venayagamoorthy.

However, in open channels, the concern of flow development is more recent. Raju et al. (2000), by comparing the hydraulic ratio of pipe and channel flows, hypothesized that the entrance length in channels should be $\approx 200h$, where h is the depth of the flow. They reported by their experiments that entrance length in open channels should range between $100h$ to $200h$. Lien et al. (2004) conducted extensive laboratory experiments and recommended a value between $150h$ to $200h$ for flow development. For example, if the flow depth is 20 cm, then the minimum length required for a flume will be 30 m, which is not feasible for most experimental facilities. Further, Zampiron et al. (2023) have also recommended similar values for entrance length in rough walls. While the initial formulations for entrance length in pipes had a dependence on Reynolds number (Latzko, 1944) and shape of entrance (Deissler, 1950), the specifications for the open channel flow are in terms of asymptotic values, where the flow is assumed to be at very large Reynolds numbers, which may not be valid for laboratory setups.

Therefore, this paper demonstrates an engineered design to obtain a fully developed flow in short flumes. We leverage our understanding of boundary layer tripping to inform this intervention that allows the flow to develop within the required distance. However, the more significant concern, even when the required development length is available, is to confirm if the flow is fully developed. The configuration of the flume can significantly influence flow development. Therefore, as a standard practice, all experimental facilities should ensure they can produce benchmark results. We develop a simple qualitative methodology to verify whether the flow is developed. Thus, the two key messages of the paper are: (i) Short flumes ($\sim$ 5m) can be engineered to obtain a fully developed flow for experimental studies, and (ii) Since flows in all flumes at all test sections must be verified for development to ensure consistency and reproducibility of results, a qualitative method, explained in this paper, can be used to confirm if the flow is developed.

3.3 Part A: Physical intervention to flow

The flume used in this study is a recirculating Armfield (S6MKII) 5 m long tilting flume with a sediment loop. The flume is 300 mm (B) wide and can accommodate flow depths up to 350 mm,

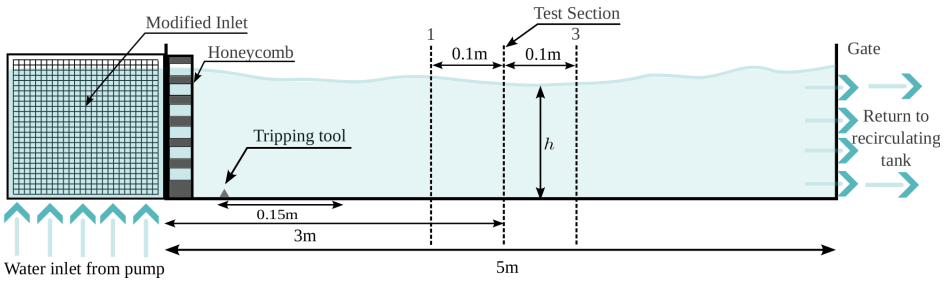

Figure 3.1: Schematic of the laboratory flume setup that also shows the modifications therein.

and has a high-precision steel bed, representing smooth walls. The flume has glass walls on the sides, which permit the use of non-intrusive optical devices such as a Laser Doppler Anemometer (LDA). The pump provides a maximum discharge of 33 l/s. It has a tailgate that can be raised to achieve the desired depth for a given discharge. A schematic of the flume is shown in Fig 3.1. The modifications shown in the flume are discussed in what follows.

In the initial configuration of the flume (not shown here for brevity), we measured several profiles that did not converge at the required cross-section located at 3 m downstream of the inlet. One such regime, measured using an Acoustic Doppler Velocimeter (ADV) along the length of the flume, is shown in Fig 3.2a. It can be observed that the flow is continuously evolving, with the flow at the boundary decelerating significantly.

The physical intervention to allow quick development is two-fold as the development is affected by two phenomena. Firstly, the inlet can be modified to ensure sufficient momentum dissipation at the inlet. The excess momentum causes the boundary region to be accelerated, and the flow takes longer to develop. The second aspect is the tripping of the boundary layer to induce instability. The instability helps the flow to acquire a classical boundary layer profile within a short distance.

Modifying the inlet is a familiar practice across different laboratories and must be tailored to the facility. Most of the existing guidelines suggest straightening the flow using a honeycomb. Many laboratories have used porous devices to remove the jet-like characteristic in the flow, but the designs have not been documented. We have used random packing materials (RPM) that diffuse the momentum at the inlet, as shown in Fig 3.3a.

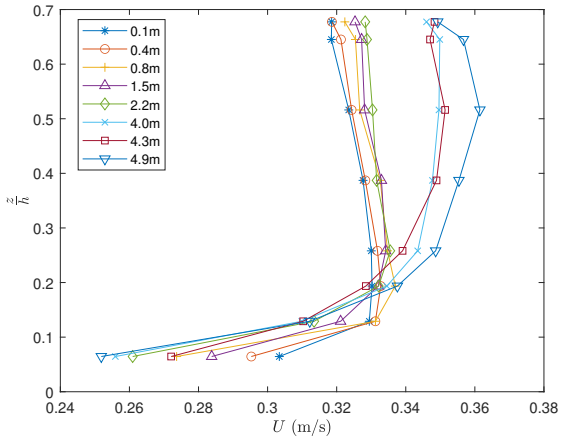

(a)

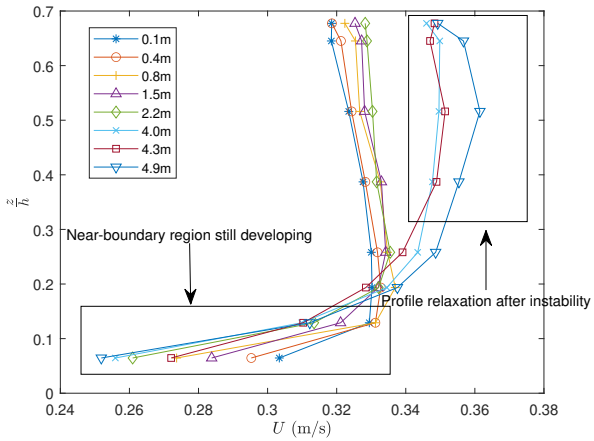

(b)

Figure 3.2: (a) Plot of velocity profile measured using an ADV along the length of the channel (b) Plot of the velocity profile highlighting the influence of incoming momentum and the change in velocity profile after the instability has been induced.

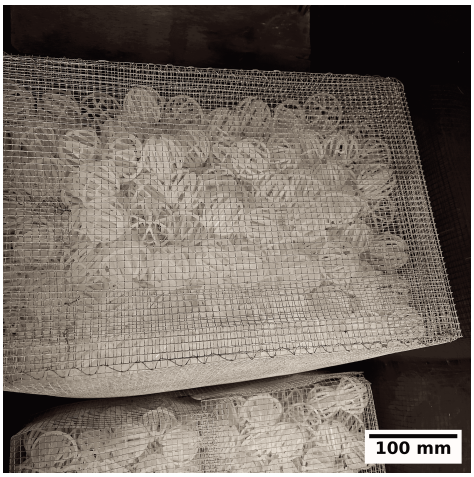

(a)

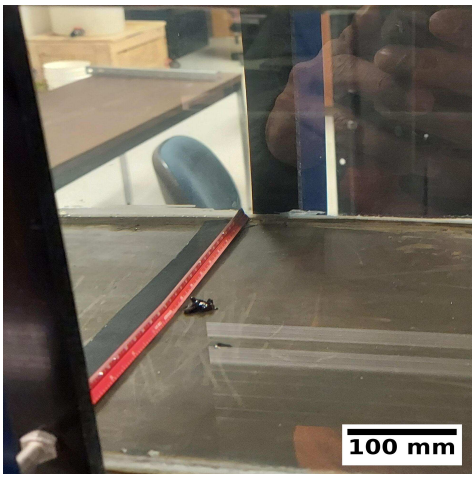

(b)

Figure 3.3: (a) Random packing material box to dissipate the incoming momentum (b) a sharp roughness element to trip the boundary layer.

Table 3.1: Flow regimes used in this study are listed in this table. The DNS profiles are non-dimensionalized and are indicated by the abbreviation ND.

Label	Re_τ	Depth (mm)	Source
ADV	2220	155	Author
DNS	1000,2000,5200	ND=1	Lee and Moser (2015)
Expt	1576	150	Author
Expt	1976	118	Author
Expt	1963	147	Author
Expt	2996	125	Author
Expt	3167	121	Author

The tripping of the boundary layer is implemented in wind tunnels using sand-grain roughness. Extensive studies have examined the effect of tripping in boundary layers. Ye et al. (2018) have shown that micro-ramps can induce transition more effectively in moderate Reynolds numbers. Thus, tripping is relevant for laboratory experiments that meet these flow conditions. Silvestri et al. (2017) recommended that the tripping element be smaller than the boundary layer thickness to be effective and, when done correctly, can reduce the development length by 50%. However, the application of tripping to hydraulic engineering research involving water is rarely observed in the literature. The tripping element needs to be higher than the one required for air. In our flume, we have utilized a sharp triangular element to trip the boundary layer, as shown in Fig 3.3b. It must be noted that this paper is focused on ensuring that the flow at the desired section is developed. For mechanics and quantitative aspects of different tripping configurations, one may refer to Elsinga and Westerweel (2011); Das et al. (2022b) and Chen and He (2023). The placement of the RPM and tripping in the flume is shown in Fig 3.1. The measurement section was chosen 3 m downstream of the inlet. To minimize side-wall effects, the measurements were made at a section equidistant from the walls.

3.4 Part B: Qualitative verification of flow development

The DNS datasets provide highly resolved, fully developed channel profile data. They can be used to ascertain whether the flow in the laboratory flume is fully developed. The DNS of

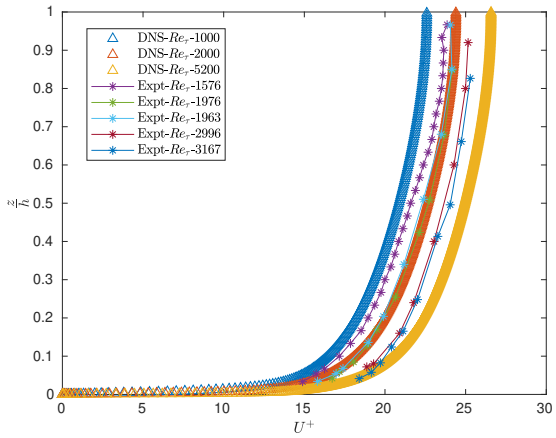

(a)

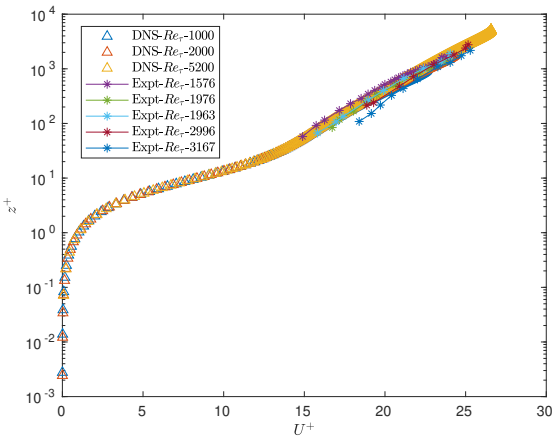

(b)

Figure 3.4: (a) Plot of non-dimensional velocity profiles with z/h (b) Plot of non-dimensional velocity profiles with the z^+ on a semi-log scale.

turbulent channel flow is performed using free-slip conditions on the walls, representing a wide channel. Since the DNS profiles are non-dimensional, the experimental profiles must also be non-dimensionalized for comparison. The verification of velocity profiles can be performed using the following procedure:

1. Calculate the friction velocity U_* using any popular method (such as the log-law method, bed-shear stress method, etc.). We have used the method as described in Mishra and Venayagamoorthy (2024).
2. Non-dimensionalize the velocity profile using the calculated friction velocity and the depth in terms of wall units $z^+ = zU_*/\nu$, where z is the distance from the wall.
3. Plot the profiles along with the DNS datasets as shown in Fig 3.4. A complete collapse of experimental profiles onto the DNS profiles ensures a fully developed flow.

The experimental velocity profiles will collapse on DNS profiles if and only if they are similar, i.e., (i) the flow in the flume is fully developed, and (ii) there are no side wall effects.

When implementing the engineered design, the influence of each behavior can be qualitatively assessed using the plot shown in 3.4a, and two cases are possible (see Fig 3.2b). If the flow near the boundary is accelerated, one must modify the inlet. Otherwise, the tripping must be adjusted to allow the flow to develop completely. The iterative procedure has been illustrated in Fig 3.5.

3.5 Results

It can be observed in Fig 3.4b that post-intervention, all, except for one, but LDA (experimental) profiles collapse completely on the DNS velocity profiles. This provides necessary and sufficient evidence that the flow is fully developed. It must also be noted that these developed profiles are obtained at $\approx 20h$, against the prevalent prescription in the literature of $\approx 100h$.

The need for a semi-log plot is evinced by the profile LDA - 3167. In Fig 3.4a, it is difficult to ascertain which profiles readily converge, especially if the Re_τ of the experimental profile is different from the available DNS profiles. Thus, we must plot the non-dimensionalized velocity with the depth non-dimensionalized by inner length scale $\delta_\nu = \nu/U_*$ to obtain a semilog curve.

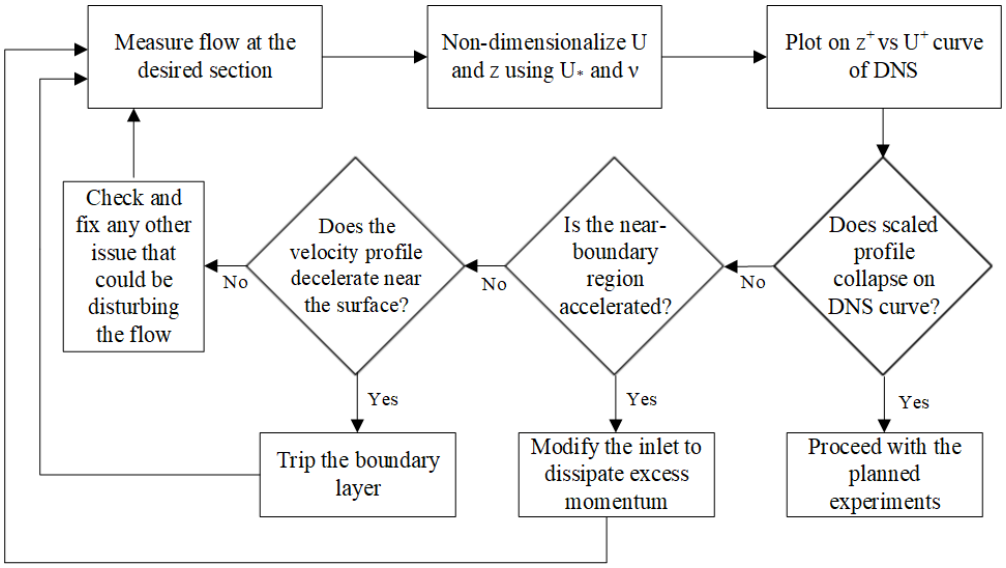

Figure 3.5: A flowchart to illustrate the procedures to ensure developed flow conditions at the required cross-section.

The departure from the semi-log curve of Expt-3167 confirms that a fully developed flow has not been obtained at that Reynolds number.

3.6 Limitations

This study limits the focus of a developed flow in terms of mean velocity profile for smooth walls. This methodology should not applied at specific instances where very large-scale flow structures need to be investigated, as by Hutchins and Marusic (2007); Nikora et al. (2007). Further, the facility is bound by the range of Reynolds numbers. In our case, the upper bound was found to be $Re_\tau \approx 3000$ after which the developed flow could not be obtained at the desired cross-section (see Fig 3.4b).

3.7 Conclusion

Contrary to the prevalent scientific thought declaring short flumes unfit for studying turbulent channel flows, we show that short flumes can be engineered to obtain fully developed flow and conduct experimental investigations. The channel modification must be specific to the facility and allow adequate dissipation of incoming momentum, followed by the tripping of the boundary layer

to induce instability. The suggested modification was implemented in our laboratory. Against the current prescription of development length, we obtained multiple fully developed profiles within a distance of $\approx 20h$ for a certain range of Reynolds numbers. Further, the measured velocity and depth profiles should be non-dimensionalized and plotted against the DNS dataset. The collapse of the measured velocity profile onto the DNS dataset confirms that the flow is fully developed. We show a complete collapse of the experimental profiles on the DNS datasets to verify the methodology.

Chapter 4

A new methodology to estimate friction velocity in smooth channel flows[3]

4.1 Purpose of the chapter

Measuring friction velocity U_* is difficult in both laboratory and field settings for engineers and scientists. The proposed new method overcomes this challenge to estimate the friction velocity U_* by measuring the velocity U_m close to the free surface, flow depth h, and temperature (for viscosity). Since near-surface measurement of velocity is not difficult, this method greatly simplifies the measurement of U_* with better accuracy than other prevalent methods in practice. Additionally, direct numerical simulation (DNS) data has been used to estimate the average velocity U_b using the measured free-stream velocity U_m, which further enables measurement of discharge using a single point measurement of velocity near the free surface in smooth channels.

4.2 Introduction

Bed shear stress τ_b, (or equivalently friction velocity U_*) is a critical parameter in the study of canonical wall-bounded flows. The friction velocity U_* acts as a scaling factor for both the velocity and length scales in the inner region of wall-bounded turbulent flows. The bed shear stress determines the extent of sediment transport and resistance to flow. Therefore, the necessity of accurately determining the bed shear stress cannot be overemphasized. However, measuring bed shear stress, even in the current state of the art, remains a major challenge for scientists and engineers. Researchers have approached this problem from different perspectives in the last five decades. Haritonidis (1989); Fernholz et al. (1996); Aberle et al. (2017) provide a comprehensive

[1]This study has been published as Mishra, H., & Venayagamoorthy, S. K. (2024). New Method to Calculate Friction Velocity in Smooth Channel Flows Using Direct Numerical Simulation Data. Journal of Hydraulic Engineering, 150(4), 04024019

review of the different techniques used for measuring bed shear stress. While direct measurements (Frei and Thomann, 1980) are preferred for their accuracy, lack of access to the near-boundary region makes such methods infeasible. The alternative is to measure bed shear stress indirectly using the velocity field. The velocity based methods are attractive since they do not require access to the bed. Much of recent research has focused on improving the estimation of bed shear stress using measured velocity profiles (Bergeron and Abrahams, 1992; Cox et al., 1996; Wilcock, 1996; Sime et al., 2007; Volino and Schultz, 2018; Womack et al., 2019).

The accuracy of velocity-based estimation of bed shear stress depends on the understanding of inner-outer layer interactions due to the lack of a universal scaling law, as well as precise measurement of the velocity field. A reliable relationship must exist to use the measured velocity U_m to calculate U_*. The uncertainty in measuring U_* can come from the technological limitation of the instrument. For example, the signals received by a popular field device called Acoustic Doppler Current Profiler (ADCP) are contaminated by a lot of noise near the boundary due to interference, rendering the measurements useless (Morlock, 1996; Biron et al., 1998). Additionally, the use of optical instruments such as Large Scale Particle Image Velocimetry (LSPIV) is restricted by the presence of suspended sediments; and intrusive devices (e.g. Ackerman and Hoover (2001); ZJ You (2007)) alter the local velocity field whose effect cannot be isolated. Even when high accuracy and precision in the measurement are ensured, the estimates of U_* can be inferior due to blind application of the theoretical framework. An example of such practice is the widespread application of the log-law method even when the measured velocity points are outside the logarithmic region. Together, these uncertainties are compounded and the estimates of U_* get worse.

In a laboratory setting, the quality of measurements can be improved by using sophisticated instruments (e.g. Laser Doppler Anemometer (LDA) and PIV, or high temporal resolution Acoustic Doppler Velocimeter (ADV) e.g., the Vectrino). However, even measurements by LDA and PIV have high uncertainty near the boundary because of low-seeding of particles, sharp velocity gradients and limited optical access. Noise due to reflection of signals hampers the performance of acoustic devices near the boundary.

Since near-wall velocity measurements are difficult, an experimental description of the velocity field down to the viscous sublayer is not readily possible with current state of the art. A complete description of the velocity field resolving all the scales was achieved using direct numerical simulation (DNS). Kim et al. (1987) performed the first, seminal, DNS of a smooth wall turbulent channel flow, albeit for a very low friction Reynolds number $Re_\tau = U_* h/\nu \approx 180$, where, h is the flow depth and ν is the kinematic viscosity. Direct Numerical Simulations (DNS) solve the Navier Stokes equations by resolving all the scales of motion. DNS requires enormous computational resources as the small scale turbulence requires the time steps to be very small. Conceptually, DNS is the simplest approach to all numerical modeling as it obviates all the complex work-arounds needed to model the flow. DNS is unparalleled in the accuracy and description provided. DNS is yet to be applied to complex geometries and coupled flows because of the computational expense. The cost of DNS increases with Reynolds numbers ($\sim Re^3$) (Pope, 2000).

Thus, in early 1990s, the first DNS was far from describing any real turbulent flow due to paucity of computational resources. With the advancement in computational capabilities, Lee et al. (2014); Hoyas et al. (2022) have performed DNS for higher Re_τ that are more in line with the realistic flows found in nature. By providing a high-resolution velocity field near the wall, DNS has drastically improved our understanding of near-wall turbulent flows. After Kim et al. (1987), Nezu and Nakagawa (2017) performed extensive turbulence measurements in open channel flow that validated the findings of DNS in the outer region but any insight in the inner-wall (near boundary) region could come only from DNS. Therefore, DNS has since proved to be an indispensable tool in providing insights on turbulent flows. However, even after three decades since the first DNS of channel flows, the potential has not been fully exploited to benefit the hydraulic engineering community.

In a pioneering attempt, Wilcock (1996) used the first DNS dataset to estimate friction velocity U_* using velocity profile and reported relationships using the (Reynolds) shear stress profile, dynamic pressure, and turbulent kinetic energy. However, measurements had to be made in the log-layer to use this method. Since, the logarithm region is only valid for $z^+ = \frac{zU_*}{\nu} < 0.2Re_\tau$

(Nezu and Rodi, 1986), it cannot be located unless U_* is known. This oversight is routinely made in practice when log-law method or Clauser's method (Clauser, 1954) is used to obtain U_* without ensuring that the points of measurement are within the logarithmic layer. Such inappropriate application of log-law method leads to significant errors in estimates of bed shear stress that manifest in incorrect calculations of sediment load, resistance to flow, and other applications.

In light of the aforementioned constraints, the strategy to estimate the bed shear stress using velocity measurements should be non-iterative, use velocity measurements away from the boundary at independent locations, and be less sensitive to errors in the measured quantities. Therefore, in this paper, we propose a new method to obtain U_* from a single near-surface maximum velocity measurement U_m, flow depth h, and kinematic viscosity ν. This method will be named as the One-point Friction Velocity Method (OPFVM). As per the strategy, we will later show that the friction velocity is sensitive only to the measurement of U_m and insensitive to the rest of the parameters. Since the velocity near the surface can be measured with high precision in both field and laboratory settings (see Aberle et al. (2017)), the accuracy in the calculation of U_* is also assured. In what follows, it will be shown that the OPFVM is more accurate than prevalent methods, simplifies friction velocity measurements, demonstrates a practical application of high-accuracy simulations, and paves the way for remote measurements of friction velocity.

With the help of experiments and DNS data, trends in the second-order statistics (fluctuations, correlations) have shown the potential to be used for estimating friction velocity. The correlation $\overline{uw}$ (where u and w are the streamwise and wall-normal velocity fluctuations respectively) follows a linear distribution in the outer layer. The linear distribution can be exploited to obtain friction velocity with reasonable accuracy. We describe the method and report associated error in the section entitled Reynolds Stress Extrapolation Method. Additionally, Nezu and Nakagawa (2017) reported that scaled fluctuations $u^+ = u/U_*$, $w^+ = w/U_*$ asymptote to 2.3 and 1.7 respectively, in the outer layer and become independent of Re_τ. The trend is confirmed by a recent DNS study at higher Re_τ, albeit with different asymptotes (Monkewitz, 2022). Some examples of application of second-order statistics to determine U_* include Pope et al. (2006), who used the turbulent kinetic

energy (TKE) to assess the suitability of laboratory flumes for studying sediment transport using ADV on natural stream beds. Johnson and Cowen (2017) have used turbulent dissipation of kinetic energy near the surface to estimate friction velocity. A similar approach has been followed by Pieterse et al. (2015) to measure shear stress in tidal channels. While the approach is innovative and exploits the understanding of turbulence for practical purposes, it is limited by the measurement capabilities of the instruments. We demonstrate that first-order statistics (mean) is sufficient to calculate U_*, obviating the need for complicated second-order statistics.

Most of the literature in this paper comes from the fluid mechanics community. The hydraulic engineers in the 1700s and 1800s tried to apply basic fluid mechanics but did not find them of practical use (Ettema, 2006). Hunter Rouse was arguably the first to leave a legacy of highly innovative and novel research in hydraulics by leveraging fluid mechanics principles. In this paper, we present an example that utilizes results obtained from fundamental fluid mechanics to improve hydraulic flow measurements in both laboratory and field settings.

4.3 Current theoretical framework and methods to estimate U_*

In a canonical turbulent flow (pipe or channel), the viscous sublayer and buffer layer are extremely thin. The maximum shear stress at the bed is caused by shear resistance due to the imposed no-slip condition. The relative size of surface protrusions to the viscous sublayer determines if the flow is hydraulically smooth or rough. In this paper, only smooth walls are considered in which roughness elements are confined within the viscous sublayer.

For a statistically stationary fully developed flow (see Wilkerson et al. (2019); Das et al. (2022b) for characteristics of fully developed flow), the bed shear stress in a Newtonian fluid is proportional to the mean strain rate and is denoted by Eq.(4.1), where μ is the dynamic molecular viscosity.

$$\tau_b = \mu \left(\frac{dU}{dz} \right) \Bigg|_{z=0} \tag{4.1}$$

4.3.1 Friction Velocity

The bed shear stress can be expressed in the dimensions of velocity $[LT^{-1}]$ and is called friction velocity U_*as shown in Eq.(4.2), where ρ is the density of the fluid.

$$U_* = \sqrt{\frac{\tau_b}{\rho}} = \sqrt{\nu \left(\frac{dU}{dz}\right)\Big|_{z=0}} \tag{4.2}$$

4.3.2 Log-law

Log-law is the most commonly used relationship in the field to determine bed shear stress. The log-law was modified to include the wake in the outer region by introducing a wake function by Coles (1956). The modified logarithmic distribution of the velocity profiles in smooth bed channels in non-dimensional form is given by Eq. (4.3).

$$U^+ = \frac{1}{\kappa}\log\left(z^+\right) + B + \frac{2\Pi}{\kappa}W\left(\frac{z}{h}\right) \tag{4.3}$$

Here, $U^+ = \frac{U}{U_*}$, U is the streamwise velocity, U_* is the friction velocity, κ is the von-Kármán's constant, $z^+ = \frac{zU_*}{\nu}$, where z is the distance from the wall, W is the wake function, h is the depth of the flow and B is the Townsend and Perry's constant.

Eq.(4.3) requires an iterative solution to obtain U_*. However, by applying Eq.(4.3) to two points, U_* can be obtained explicitly.

$$U_* = \kappa\left[\frac{U_2 - U_1}{\log\left(\frac{z_2}{z_1}\right)}\right] \tag{4.4}$$

At a sufficiently high Reynolds number, the two-point log-law method (Eq.(4.4)) becomes very effective as the wake function becomes a constant and it can be eliminated (Guo, 2014), along with the Townsend and Perry's constant B. However, it also suffers from several limitations that contribute to the uncertainty in U_*. First, the von Karman's factor κ can range from 0.37 to 0.40 (Guo et al., 2005; Nagib and Chauhan, 2008; Gaudio et al., 2010). Second, the choice of the points

z_1 and z_2 is arbitrary. The DNS datasets (refer Table 4.1) were used to study the impact of the choice of points in the friction velocity estimation using the two-point log-law method. In this analysis, different combinations of points were used to calculate U_* and the associated error ϵ as defined in Eq.(4.5).

$$\epsilon = \left(1 - \frac{U_{*calc}}{U_*}\right) \times 100 \tag{4.5}$$

The results are presented in Fig 4.1 and Fig 4.2 for both closed channel flow (CCF) and open channel flow (OCF) respectively. For each Re_τ, the first point z_1 is represented as a series and the second point z_2 has been plotted on the x-axis. Every point represents a combination of z_1 and z_2. The points are chosen in increments of $0.1h$, from $0.1h$ to $0.9h$. The percentage error ϵ is plotted on the y-axis. On OCF plots, we can observe that no two points provide the same value of U_*. For points $z_1 \leq 0.4h$, the minimum error is obtained for $z_2 = 0.7h$. Contrary observations are found for CCF where the error for $z_2 = 0.7h$ is maximum. Additionally, for some values of z_2, at $z_1 = 0.2h$, the estimate of friction velocity is quite accurate ($\epsilon \approx 0$). However, for higher Re_τ, no generalizable trend can be observed. Even if we ignore the possible variation in the von-Karman's factor κ, the lack of prescription and arbitrariness in choice of points introduces significant error in the calculation of U_* using the two-point log-law method. Thus, the methodology to calculate U_* needs improvement.

4.3.3 Reynolds Stress Extrapolation Method

The instantaneous Navier-Stokes equations are time-averaged to obtain the Reynolds-Averaged Navier Stokes (RANS) equations. For a steady, fully-developed channel flow, the Reynolds stress (turbulent momentum flux) is given by $\overline{uw}$. In the outer layer, the Reynolds stress varies linearly and can be approximated by Eq.(4.6).

$$\overline{uw} \approx U_*^2 \left(1 - \frac{z}{h}\right) \tag{4.6}$$

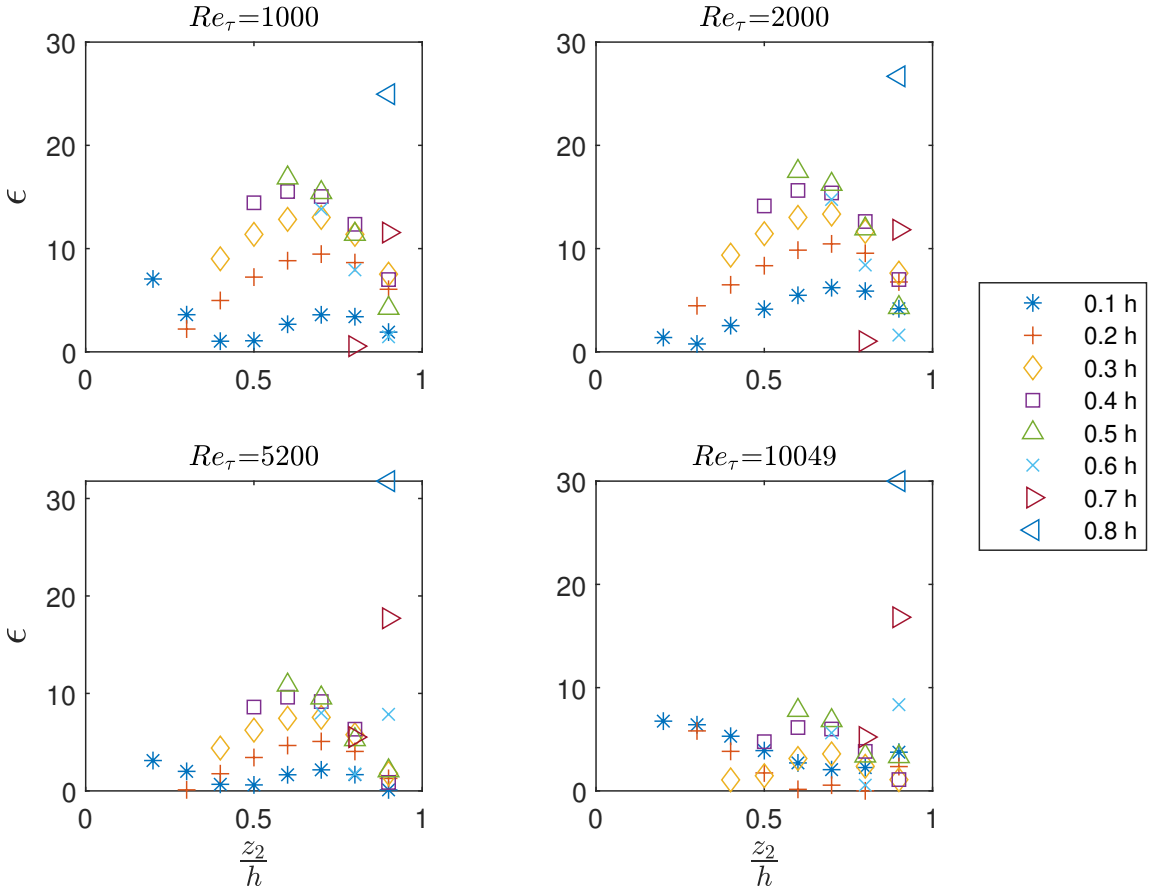

Figure 4.1: Influence of the location of velocity measurement points on U_* estimation using the two-point log-law method for CCF is illustrated. In each sub-figure, the first point (z_1/h) is plotted as a series on each graph and the second point (z_2/h) is plotted on the x-axis for a specific Re_τ. The y-axis shows the percentage error ϵ in estimates of U_* estimation for the chosen set of two points.

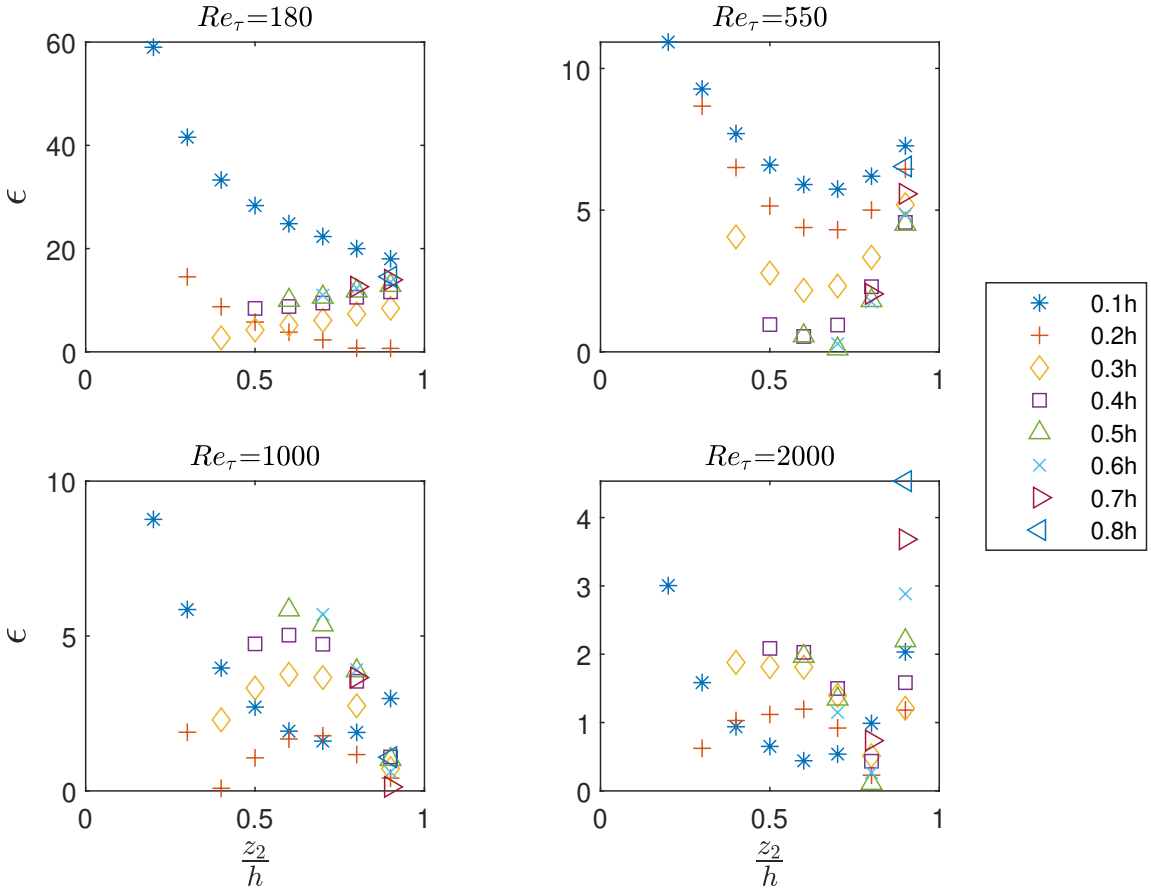

Figure 4.2: Influence of the location of velocity measurement points on U_* estimation using the two-point log-law method for OCF is illustrated. In each sub-figure, the first point (z_1/h) is plotted as a series on each graph and the second point (z_2/h) is plotted on the x-axis for a specific Re_τ. The y-axis shows the percentage error ϵ in estimates of U_* for the chosen set of two points.

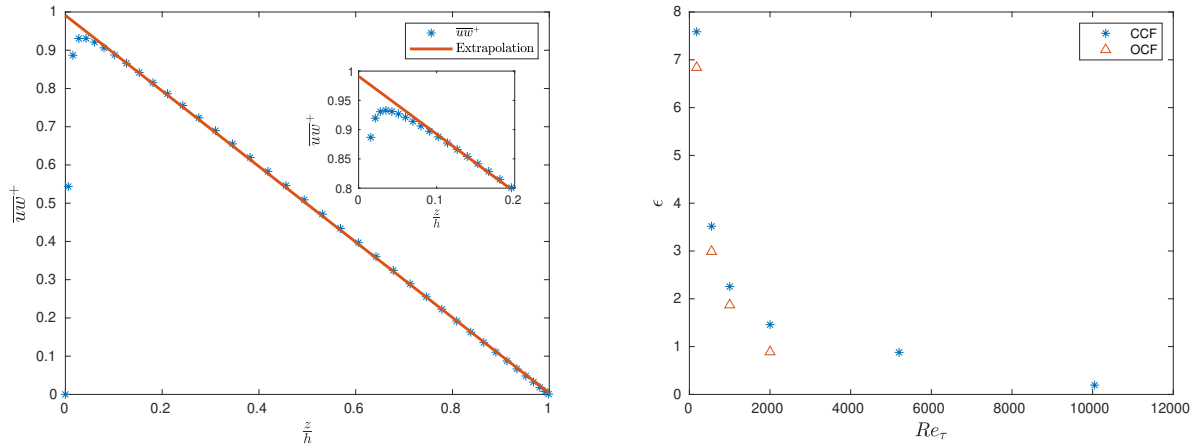

Figure 4.3: (Left panel) The Reynolds stress extrapolation method is demonstrated using DNS CCF - 5000 profile. The non-linear distribution near the boundary (shown in the inner box) causes an error in U_* estimation. The percent error ϵ in estimating U_* is shown in the right panel as a function of Re_τ

Through extrapolation, the linear distribution of Reynolds stress $\overline{uw}$ can be used to estimate the friction velocity by obtaining the stress at $z = 0$. This method is shown in Fig 4.3. The extrapolation does not lead to the exact value of U_* because the Reynolds stress is not linear near the boundary. The non-linear portion shrinks as Re_τ increases, and $\overline{uw}$ approaches U_*^2. The error in estimating U_* using this method is shown in Fig 4.3. At high $Re_\tau(\geq 2000)$, the error is less than 2%.

While the Reynolds stress extrapolation is a powerful method in a laboratory setting, it is limited in the field due to the small magnitude of wall-normal velocity fluctuations w and low signal-noise ratio (SNR). Filtering noise signals leads to the loss of useful data points. The problem is further exacerbated by the low temporal resolution of field devices (usually 1 Hz) that is grossly inadequate to capture the complete spectral distribution. The dimensionless wave number $L_x k_{max}$, where L_x is the length scale and k_{max}, is the maximum wave number, must be at least 100 to analyze the spectral distribution down to the viscous subrange (Nezu and Nakagawa, 2017). Since L_x scales with the depth h in the outer layer, the maximum frequency response can be approximated to $(50/\pi)(U/h)$. With increase in depth, the time-scale gets longer and the frequency decreases. Therefore, it becomes more difficult in the field to measure the Reynolds stress.

4.3.4 Manning's equation and the average shear stress method

In absence of velocity measurements and under the assumption of a steady uniform flow, the average velocity U_b can be calculated using Eq.(4.7) by measuring the the cross sectional area A, wetted perimeter P, and the bed slope S_0. The Manning's constant n can be obtained once the material of the bed is known.

$$U_b = \frac{1}{n} R^{2/3} S_0^{1/2} \tag{4.7}$$

In Eq.(4.7) $R = A/P$ is the hydraulic radius. The average shear stress in a steady uniform open channel flow is given by $\tau_{avg} = \gamma R S_0$, where γ is specific weight of water (see Chow (1957); Nezu and Nakagawa (2017)). Then, U_* is calculated as,

$$U_* = \sqrt{g R S_0} \tag{4.8}$$

Eq.(4.8) utilizes the net momentum balance to obtain the average shear stress and is useful in determining average shear resistance to the flow. Application of Eq.(4.8) is explained in the section entitled Quasi-field analysis and comparison of OPFVM with prevalent methods. While Eq.(4.8) provides an efficient method to calculate U_*, the calculated value of U_* using this method is an average that is different from the local friction velocity. The local friction velocity is a more relevant parameter because the average shear stress method (Eq.(4.8)) involves the spatial average of the bed shear stress across the width of the channel. Whereas, the friction velocity calculated using either the log-law method or the proposed OPFVM is the local friction velocity since it is based on the velocity profile at a particular section along the width of the channel. The difference between average shear stress (τ_{avg}) and local shear stress (τ_{local}) has been reported by Yang (2010); Replogle and Chow (1966); Yen (2002). Therefore, it may be more appropriate to use the local friction velocity as obtained using the log-law method or preferably, the OPFVM, as will be shown. For example, sediment transport is a local process and depends on local friction velocity. The use of average friction velocity instead of local friction velocity causes underestimation in the sediment transport because the incipient motion relies on a breach of threshold initial shear stress, i.e. if

$\tau_{local} > \tau_c$, the sediment should move. However, the bed shear stress based on average friction velocity will not suggest movement, while in reality the stress associated with the local friction velocity has already breached the threshold. Recently, Patel et al. (2020) suggested incorporating maximum shear stress for stable channel designs instead of average shear stress (Guo and Julien, 2005) using similar reasoning. Thus, even though the method is popular, it does not provide the local friction velocity, which is required for most engineering applications.

Evidently, prevalent methods to estimate bed-shear stress suffer from serious limitations. Therefore, a new method called the One-point Friction Velocity Method (OPFVM) is proposed in this study and presented in the following section.

4.4 One Point Friction Velocity Method (OPFVM)

The friction velocity U_* must depend on a velocity scale U_m, a length scale h, dynamic viscosity μ and, density ρ. Therefore, $U_* = f(U_m, h, \rho, \mu)$. The dynamic viscosity can be expressed as $\mu = \rho\nu$. Dimensional analysis using the Buckingham-pi theorem will result in two non-dimensional parameters namely $Re_m = \frac{U_m h}{\nu}$ and $Re_\tau = \frac{U_* h}{\nu}$. Here, U_m, U_*, h, and ν are as defined previously. Therefore,

$$Re_\tau = f(Re_m) \tag{4.9}$$

The functional relationship between Re_τ and Re_m cannot be established theoretically. Therefore, an empirical relationship is obtained between the Reynolds number based on maximum free-surface velocity $Re_m = \frac{U_m h}{\nu}$ and the friction Reynolds number $Re_\tau = \frac{U_* h}{\nu}$ using five DNS CCF datasets provided by Lee and Moser (2015); Hoyas et al. (2022). The empirical relationship is well described by a power-law given as

$$Re_\tau = 0.1068 Re_m^{0.912} \tag{4.10}$$

The relationship given by Eq.(4.10) is shown in Fig 4.4 with a coefficient of determination R^2 of 0.99. Twenty years ago, Pope (2000) suggested a similar relationship when DNS was only

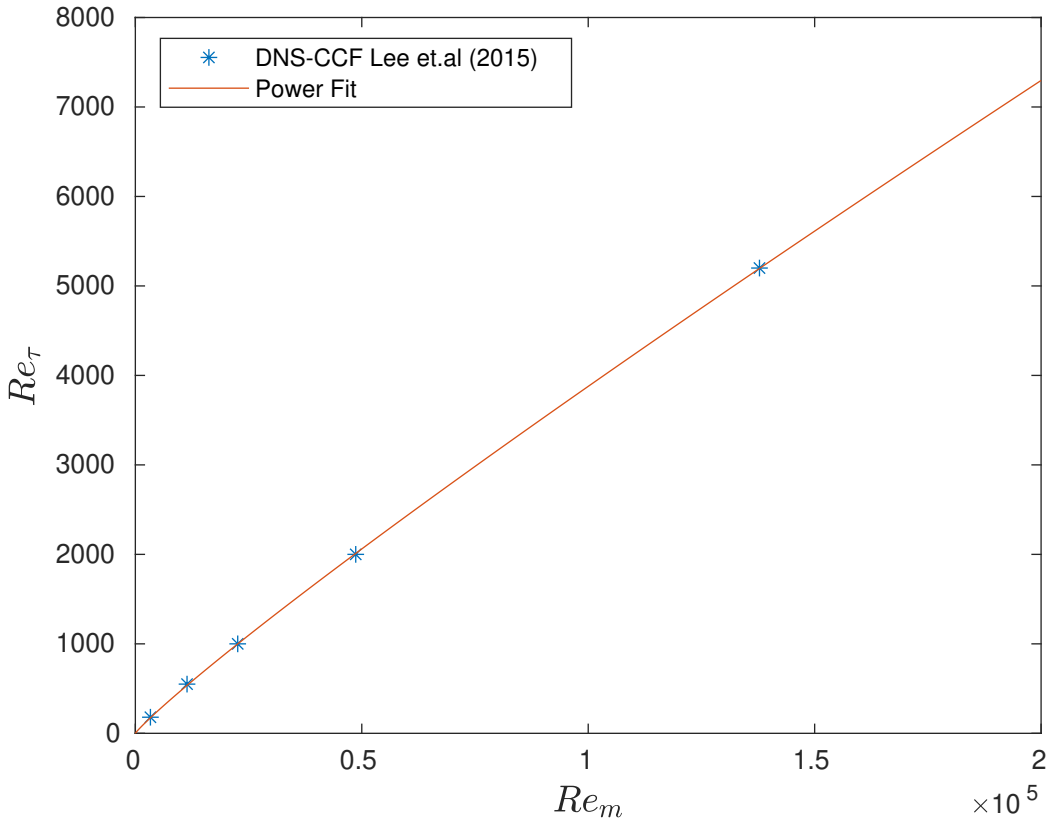

Figure 4.4: A power-law relationship between Re_m and Re_τ using CCF DNS dataset. The relationship is given in Eq.(4.10).

available for Re_τ=180-550. The DNS datasets used by Pope (2000) were limited by low Re_τ values and did not correspond to any realistic turbulent flows. Nevertheless, he reported $Re_\tau = 0.09Re_m^{0.88}$, which, although appears similar to Eq.(4.10), diverges significantly with increase in Re_τ. Eq.(4.10) can be rearranged using the definition of $Re_m = \frac{U_m h}{\nu}$ and $Re_\tau = \frac{U_* h}{\nu}$ to obtain the friction velocity U_*.

$$U_* = 0.1068{U_m}^{0.912}\left(\frac{\nu}{h}\right)^{0.088} \tag{4.11}$$

4.4.1 DNS dataset

The DNS code accomplished by Lee and Moser (2015) used a Fourier-Gelarkin method in streamwise (x) direction and B-spline collocation method in the wall normal (z) direction. The

Table 4.1: Datasets used in this study. The depth for DNS datasets has been non-dimensionalized and denoted by ND=1.

Study	Flow Type	Re_τ	Re_m	U_* (m/s)	Depth (mm)	Source	Symbol
DNS	CCF	180	3326	0.0637	ND=1	Kim et al. (1987)	CCF 180
	CCF	550	11414	0.0543		Lee and Moser (2015)	CCF 550
	CCF	1000	22604	0.0500		Lee and Moser (2015)	CCF 1000
	CCF	2000	48664	0.0459		Lee and Moser (2015)	CCF 2000
	CCF	5200	137817	0.0415		Lee and Moser (2015)	CCF 5000
	CCF	10049	257143	0.0346		Hoyas et al. (2022)	CCF 10000
	OCF	180	3343	0.0639		Yao et al. (2022)	OCF 180
	OCF	550	11391	0.0547		Yao et al. (2022)	OCF 550
	OCF	1000	22612	0.0502		Yao et al. (2022)	OCF 1000
	OCF	2000	48579	0.0462		Yao et al. (2022)	OCF 2000
LDA	OCF	1963	38133	0.0122	147	Author	LDA 1963
	OCF	2996	58667	0.0219	125	Author	LDA 2996

time advancement used a third-order Runge Kutta based semi-implicit scheme for the non-linear terms of the Navier Stokes equation and Crank-Nicolson for viscous terms. It should be noted that all of these simulations follow the seminal work of Kim et al. (1987). Please refer to Lee and Moser (2015); Hoyas et al. (2022) for more details on the code and methodology of the simulations.

4.4.2 Experimental Setup

The experimental setup is shown in Fig 4.5. The study used a recirculating Armfield (S6MKII) 5 m long tilting flume with a sediment loop. The flume is 300 mm wide and can accommodate flow depth of up to 350 mm. It consists of a fabricated high-precision stainless steel bed with bed deformations of less than 1 mm, resembling a smooth bed. The flume has glass walls on the sides which permit the use of non-intrusive optical devices such as an LDA. The flow was seeded using 20 μm spherical, uncoated, polyamide particles. Fully developed conditions were obtained at the test section after tripping the boundary layer. The test section was located at 3.0 m downstream of the inlet.

The *Dantec Inc.* 2D - LDA apparatus consists of a dual-pumped solid-state (DPSS) laser connected to a photo-multiplier assembly. The frequency shift is processed by a Burst Spectrum

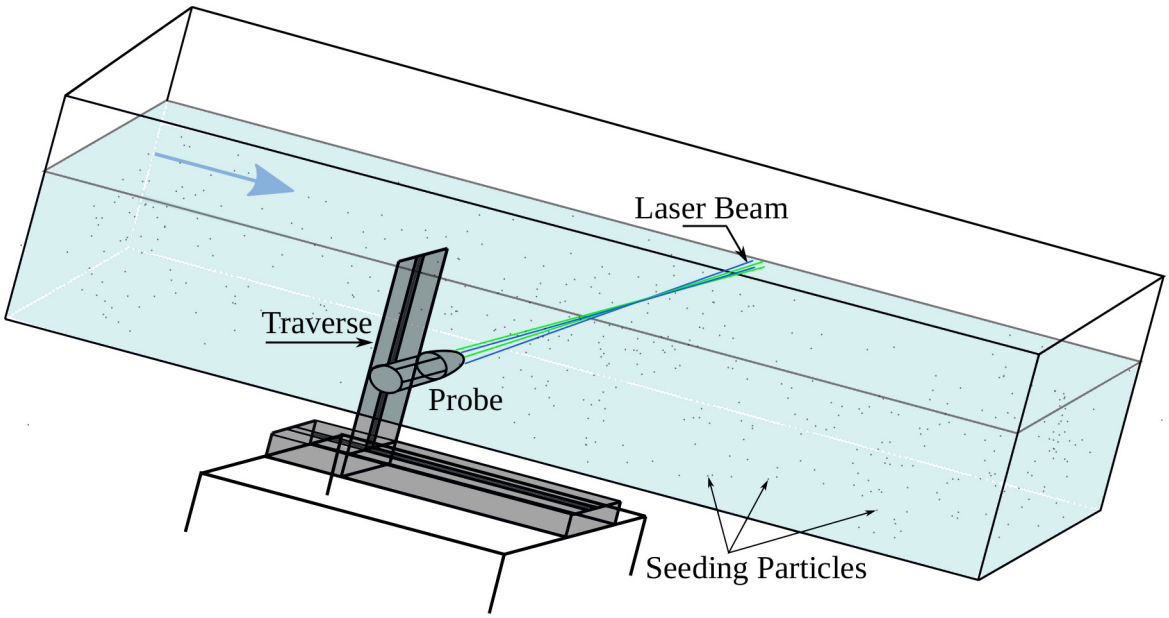

Figure 4.5: Schematic diagram of experimental setup consisting of a laboratory flume and LDA system. The arrow denotes the streamwise direction, X. The wall normal direction is denoted by Z. The traverse moves in the X-Z plane.

Analyzer (BSA) connected to a computer. The DPSS laser emits two beams of wavelength 513 mm and 495 mm, respectively. Each beam has a maximum power of 120 mW and is split into two by the photo-multiplier. The beams are passed into the flow using a probe. The laser is connected to the Bragg cell that provides the Bragg frequency shift of 40 MHz. The beam has a focal length of 398.4 mm, beam diameter of 1.35 mm, and beam spacing of 38.3 mm. The beam intersection angle is 20°. An *iSEL*-s8 traverse controller moves the probe in the X-Z plane with an accuracy of ± 0.1 mm. The operational arrangement of the LDA system is shown in Fig 4.5. For details on operation of an LDA system refer to Durst et al. (1981); Aberle et al. (2017).

4.5 Results

The U_* obtained using Eq. (4.11) is subsequently applied to one independent CCF DNS dataset, four OCF DNS datasets, and two experimental profiles measured using the LDA. The performance of Eq. (4.11) is discussed in the following subsections.

4.5.1 Application to CCF data

To test if Eq.(4.11) is applicable for flows with $Re_\tau > 5000$, we calculate U_* of an additional dataset DNS CCF-10049 (listed in Table 4.1) using Eq.(4.11) and compare it with the friction velocity provided in the DNS dataset. As shown in Fig 4.7, the error ϵ in calculating U_* is less than 1%, providing confidence in the use of proposed method.

4.5.2 Application to OCF DNS data

Recently, Yao et al. (2022) published the OCF DNS data for moderately high Reynolds numbers ($Re_\tau \approx 2000$). The dataset provides insights into how the OCF differs from the CCF. In open channels, there is a marked anisotropy near the surface. However, the trend suggests that both canonical flows converge after a certain Reynolds number. We investigated mean velocity profiles for the OCF and CCF data and observed adequate convergence, as shown in Fig 4.6, to apply Eq.(4.11) to the OCF dataset for calculating U_*. The calculated U_* shows remarkable agreement as shown by the low percentage error ϵ (Eq. (4.5)) in Fig 4.7.

4.5.3 Application to OCF - Laboratory data

Experimental velocity profiles (LDA 1963 and LDA 2996 as shown in Table 4.1) were obtained for two different flow rates and Eq.(4.11) was used to estimate U_* using the point closest to the free surface. Unlike the DNS flow datasets, U_* is not available for experimental profiles. The only independent method to test if U_* is reasonably close to the actual value is to scale the velocity profiles in terms of U^+ and z^+. If U_* is correct, the scaled experimental profiles will collapse on the scaled DNS profiles. Using the above procedure, the velocity profiles were non-dimensionalized using U_*. It is evident from Fig 4.8 that the measured experimental velocity profiles collapse on both CCF and OCF DNS profiles. The collapse confirms that the estimation of U_* is correct and the flow is fully developed in the measured section.

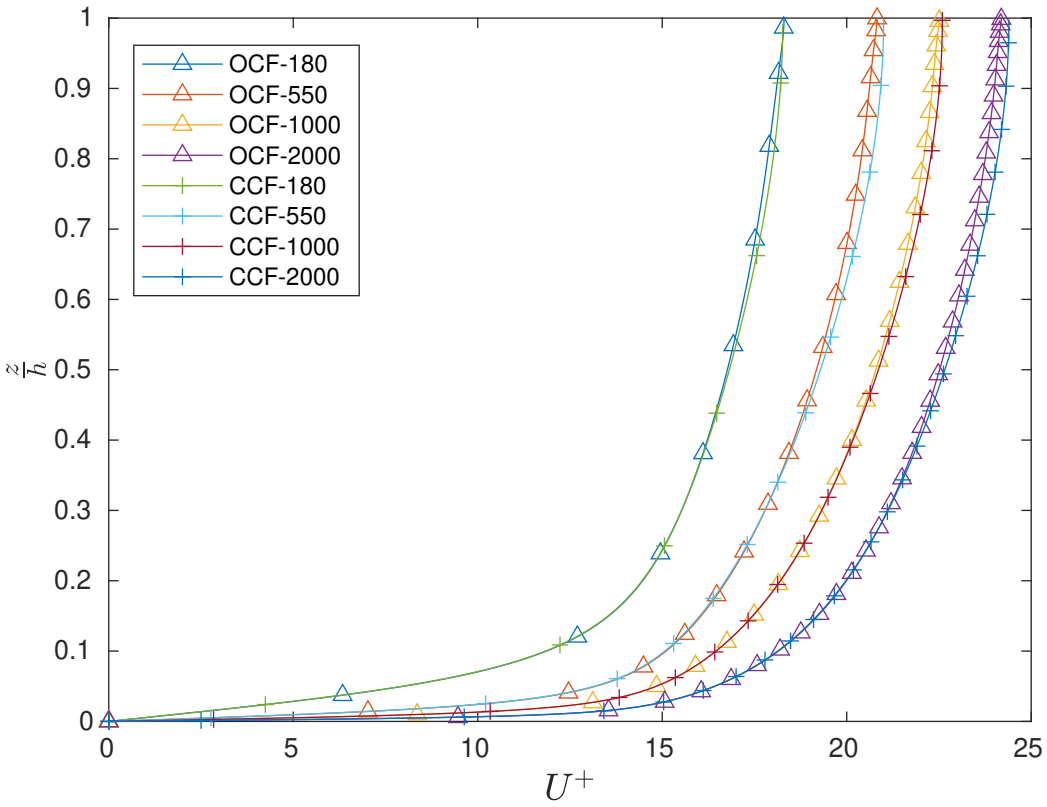

Figure 4.6: The non-dimensional mean streamwise velocity profiles for OCF and CCF from DNS data. The OCF and CCF profiles are almost identical to each other.

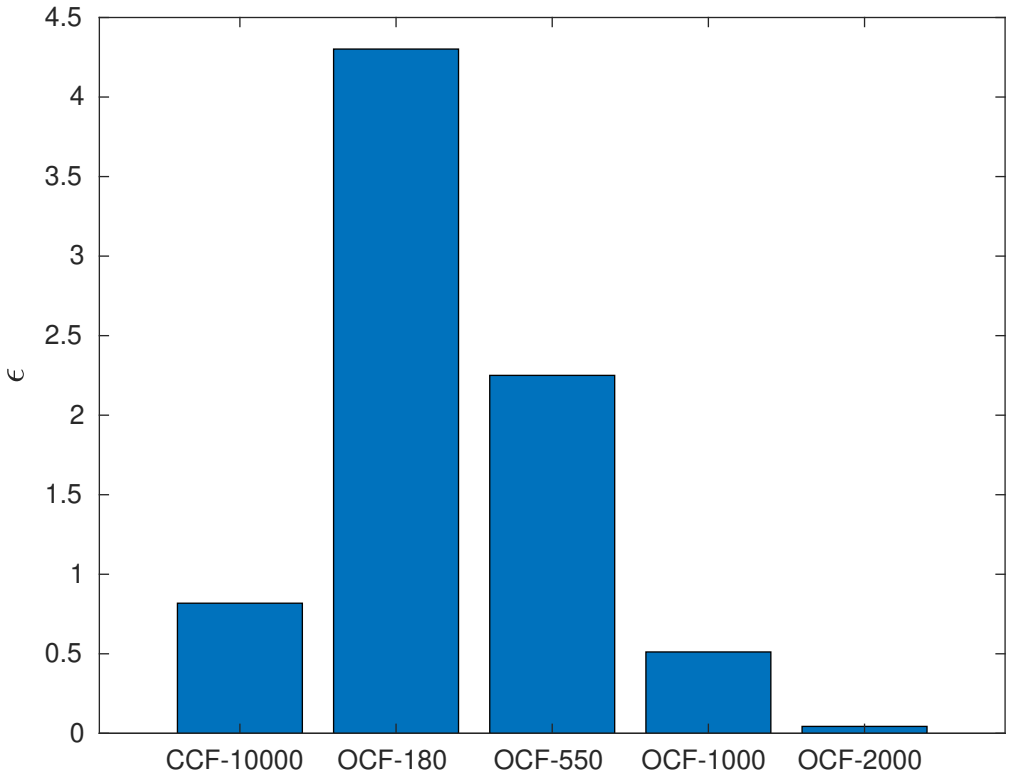

Figure 4.7: Percentage error ϵ in estimates of friction velocity using Eq.(4.11). The error is calculated using Eq.(4.5).

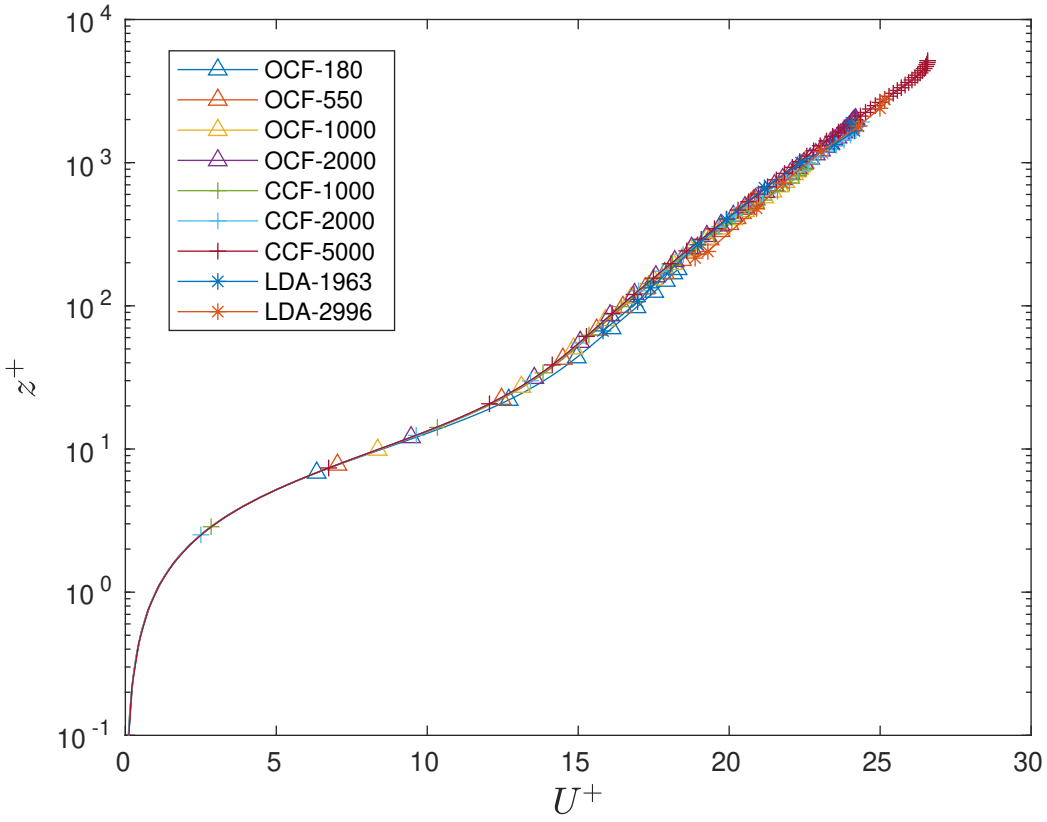

Figure 4.8: Illustration of the collapse of experimental profiles scaled using the friction velocity U_* calculated using Eq.(4.11) on top of DNS-CCF and DNS-OCF profiles.

Table 4.2: U_* obtained using the methods are listed in this table. The scaled non-dimensional velocity profiles $U^+ = U/U_*$ are shown in Fig 4.9. ϵ_{loglaw} and $\epsilon_{avgshear}$ are percentage errors with respect to U_* calculated using OPFVM.

Experiment	Estimated U_* (m/s)			ϵ_{loglaw}	$\epsilon_{avgshear}$
	OPFVM	Two-point log law method	Average stress method		
LDA 1963	0.012	0.010	0.015	25	16.67
LDA 2996	0.022	0.017	0.027	22.73	22.73

4.5.4 Quasi-field analysis and comparison of OPFVM with prevalent methods

In this subsection we apply Eq.(4.7) to the laboratory data to obtain the effective slope S_e. In a laboratory, the average velocity U_b can be calculated using the measured discharge. The value of S_e is substituted in Eq.(4.8), in place of S_0 to obtain U_*. Similarly, U_* is calculated using Eq.(4.4) to assess the performance of the two-point log-law method.

The U_* calculated using Eq.(4.4) and Eq.(4.8) are listed in Table 4.2 and compared to the U_* calculated using the OPFVM. The percentage errors for Manning's equation and log-law equation are denoted by $\epsilon_{avgshear}$ and ϵ_{loglaw} respectively, and are found to be more than 20% as shown in Table 4.2. Further as shown in Fig 4.9, the scaled experimental profiles using U_* obtained by log-law and average shear stress methods deviate significantly from the DNS profile, whereas the U_* calculated using OPFVM causes a complete collapse.

4.5.5 Sensitivity Analysis of OPFVM

Eq.(4.11) is a function U_m, h, and ν. Error in the measurement of any one of the quantities will influence the estimation of U_*. We perform a sensitivity analysis to report the effect of individual errors in the estimation of U_*. Taking the logarithm of Eq.(4.11) and differentiating, we obtain the error equation of U_*.

$$\frac{\Delta U_*}{U_*} = 0.912\frac{\Delta U_m}{U_m} + 0.088\frac{\Delta h}{h} + 0.088\frac{\Delta \nu}{\nu} \tag{4.12}$$

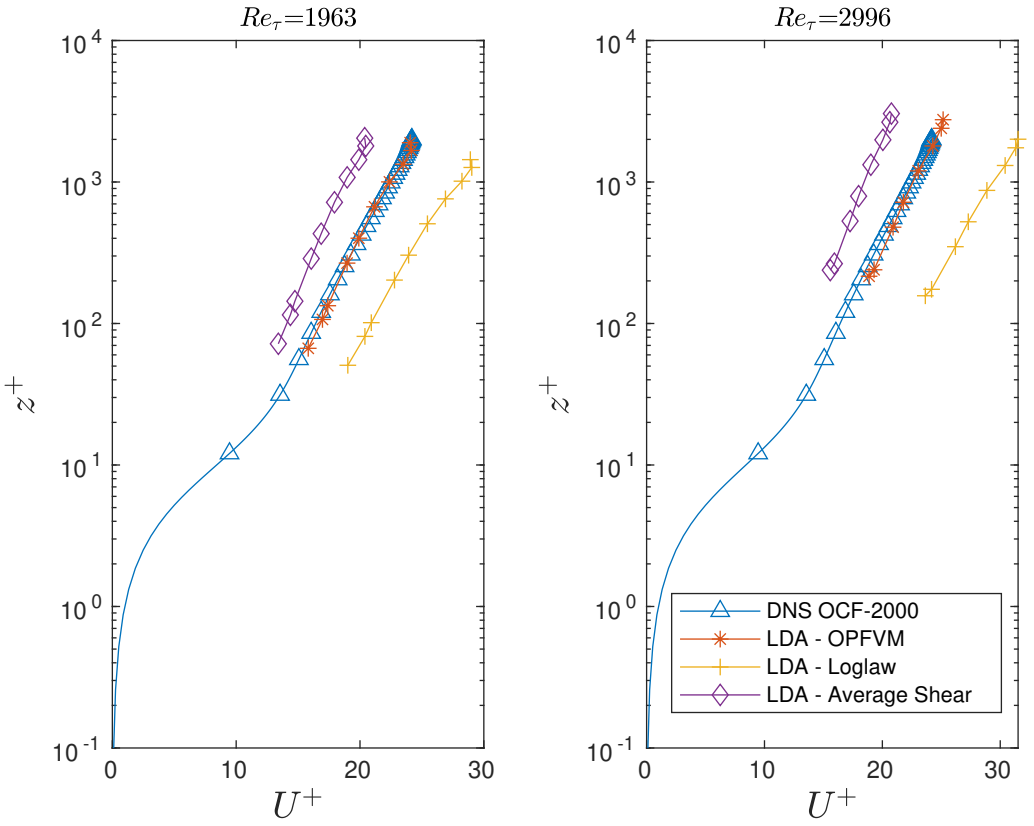

Figure 4.9: Scaling of velocity profiles using U_* calculated using methods listed in Table 4.2. The U_* calculated using the OPFVM causes experimental profiles to collapse on DNS profile.

Here ΔU_*, ΔU_m, Δh and $\Delta \nu$ are the errors in U_*, U_m, h and ν respectively; and the absolute values of relative errors must be used.

Influence of error in U_m

To estimate the influence of error in measuring U_m, assume $\Delta h = \Delta \nu = 0$. Then Eq.(4.12) reduces to Eq.(4.13).

$$\frac{\Delta U_*}{U_*} = 0.912 \frac{\Delta U_m}{U_m} \tag{4.13}$$

Eq.(4.11) has been formulated using the maximum velocity in a fully developed turbulent channel flow that occurs at the surface. During field measurements, it may not be possible to measure the velocity exactly at the surface due to fluctuations. Additionally, conventional acoustic measurement devices (ADCP and ADV) do not capture the velocity at the surface (Simpson and Oltmann, 1993; Muste et al., 2004; Aberle et al., 2017). It has also been shown that the free-stream perturbation may have a minor influence on the velocity profile (Das et al., 2022a). Therefore, any measurement of U below the surface will introduce some error in the estimation of U_*. To restrict error in U_* to 2%, we need to restrict error in the measurement of U_m to approximately 2%. The depth at which the streamwise velocity U deviates by 2% from the maximum is calculated using the DNS datasets. In this 'permissible region' for measuring U_m (shown in Fig 4.10), the deviation is less than 2%. As Re_τ increases, the depth of permissible region also increases. For $Re_\tau > 1000$, it is safe to measure U_m up to $0.75h$. The error is inevitable in laboratory and field because measurements at the surface are not possible due to fluctuations. Thus, for experimental profiles LDA 1963 and LDA 2996 the points nearest to the surface where U_m could be measured were $0.92h$ and $0.96h$ respectively. Since $0.92h$ and $0.96h$ are greater than $0.75h$, as per Eq.(4.13), the error in estimating U_* must be within 2%. This is indeed the case as shown in Fig 4.8 wherein the scaled experimental velocity profiles readily collapse onto the DNS profiles. Eq.(4.13) can also be used to calculate the influence of other systematic errors (e.g. instrument errors). However, random errors are eliminated due to averaging.

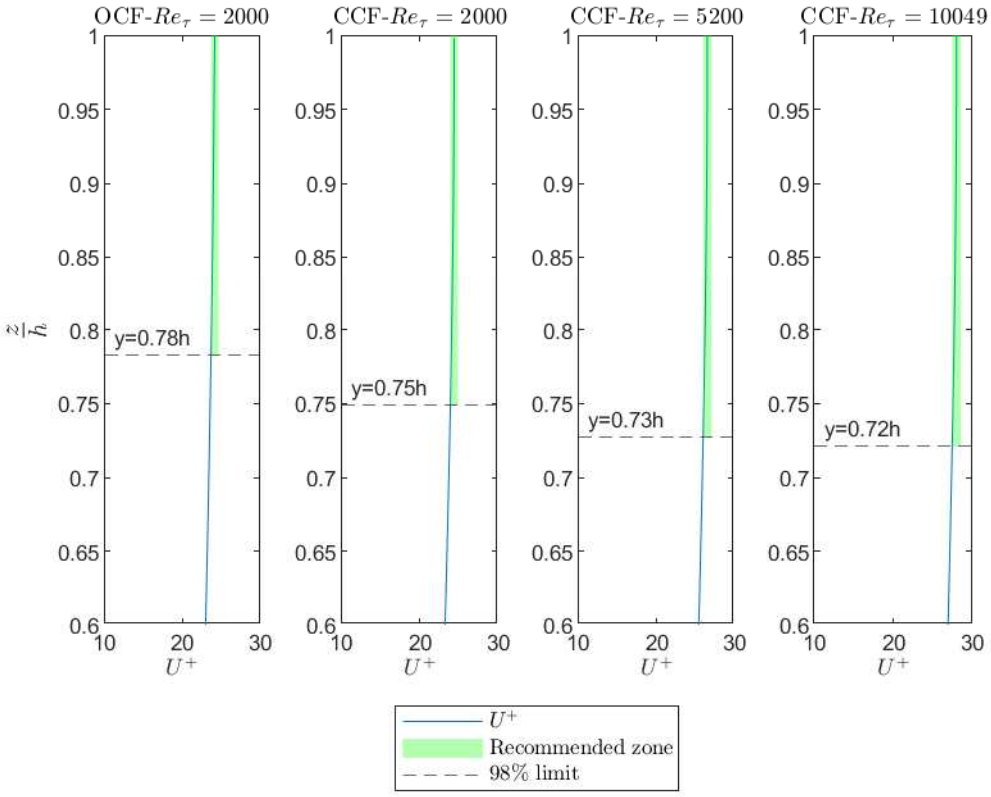

Figure 4.10: The shaded region in this figure shows the location of measurement that would restrict the error in estimating U_* using Eq.4.11. As Re_τ increases, one can measure deeper without exceeding the permissible error in U_*.

Influence of error in depth h

The influence of error in depth can be similarly calculated using Eq.(4.12) by setting ΔU_m and $\Delta\nu$ to zero. The resulting equation is given as Eq.(4.14).

$$\frac{\Delta U_*}{U_*} = 0.088\frac{\Delta h}{h} \tag{4.14}$$

U_* is not very sensitive to the error in h. E.g. an error of 10% in the measurement of h will only cause an error of 0.8% in the estimation of U_*. In the current state of the art, advanced surveying techniques can measure the channel geometry very precisely. Therefore, it is safe to assume that U_* is insensitive to errors in the measurement of depth.

Influence of error in viscosity ν

The kinematic viscosity is measured indirectly by using the functional relationship between kinematic viscosity ν and temperature T. Therefore, we include T in Eq.(4.12) by applying the chain rule.

$$\frac{\Delta U_*}{U_*} = 0.088\left(\frac{d\nu}{dT}\right)\frac{\Delta T}{\nu} \tag{4.15}$$

Since for a small range of temperature $\frac{d\nu}{dT} \sim O(10^{-5})$, the error in U_* due to uncertainties in temperature measurements will be negligible. Thus, U_* is relatively insensitive to the error in viscosity (temperature) measurement also.

4.6 Average velocity U_b vs maximum velocity U_m

In the field, an engineer is also interested in obtaining the average velocity to calculate the discharge. The average velocity usually occurs at $0.6h$ from the surface (Corbett, 1943). We test this relationship using the CCF DNS data and find this relationship to be quite robust as shown in Fig 4.11.

In this paper, we have emphasized measuring the near-surface velocity because it is easy to measure. Furthermore, it is possible to use the near-surface velocity to estimate U_b. The analysis

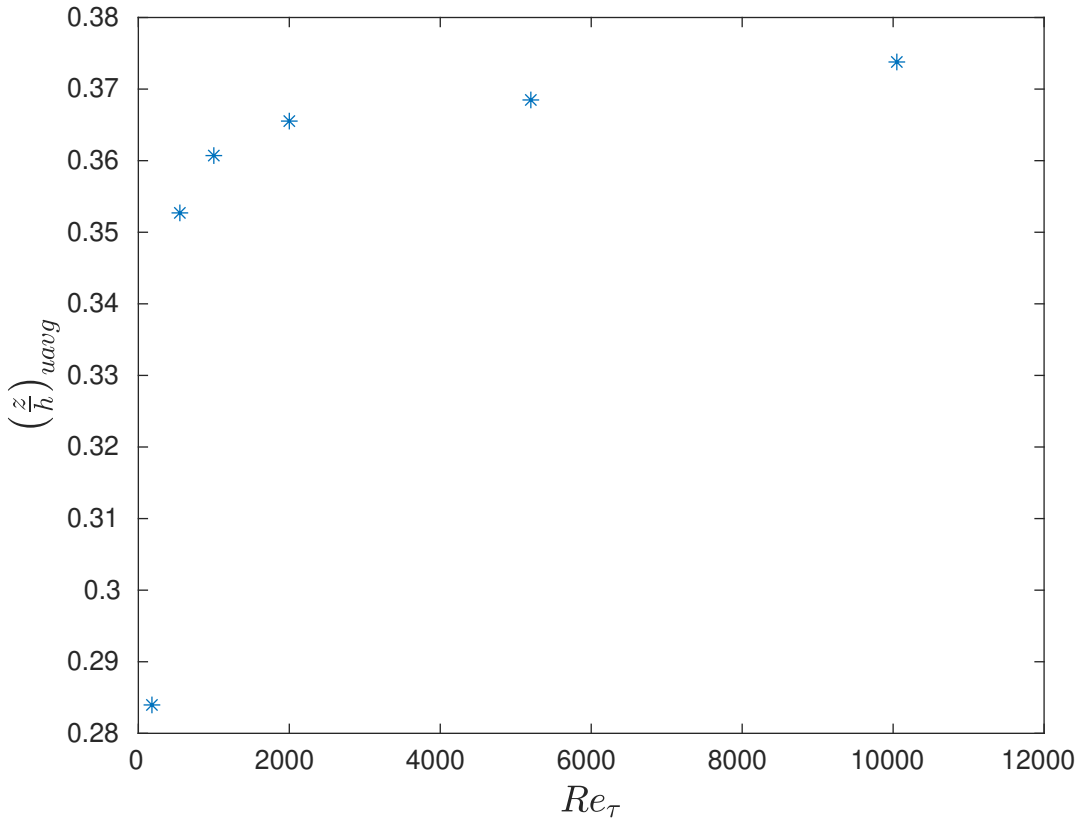

Figure 4.11: The location of average velocity U_b in velocity profiles obtained from CCF DNS data. The location of average velocity approaches $0.4h$ as Re_τ increases.

of DNS data provides a relationship $U_b \approx 0.9U_m$. This relationship is evident from Fig 4.12 and can be used to estimate the average velocity U_b and consequently the discharge.

4.7 Discussion

Even though Eq.(4.11) is obtained using an empirical relationship, it is not surprising that U_* depends strictly on U_m, h and ν. The formulation is another evidence that the inner and outer regions of a canonical flow interact with each other. Townsend (1961) suggested that the inner and outer layer are completely decoupled. The recent advances (mainly through DNS of channel flows) challenge this assertion. Studies by Morrison (2007) and Jiménez (2013) point to a weak coupling between inner and outer layers that weakens further as Re_τ increases. This weak coupling has manifested in the weak dependence of U_* on ν in Eq.(4.11). The current formulation

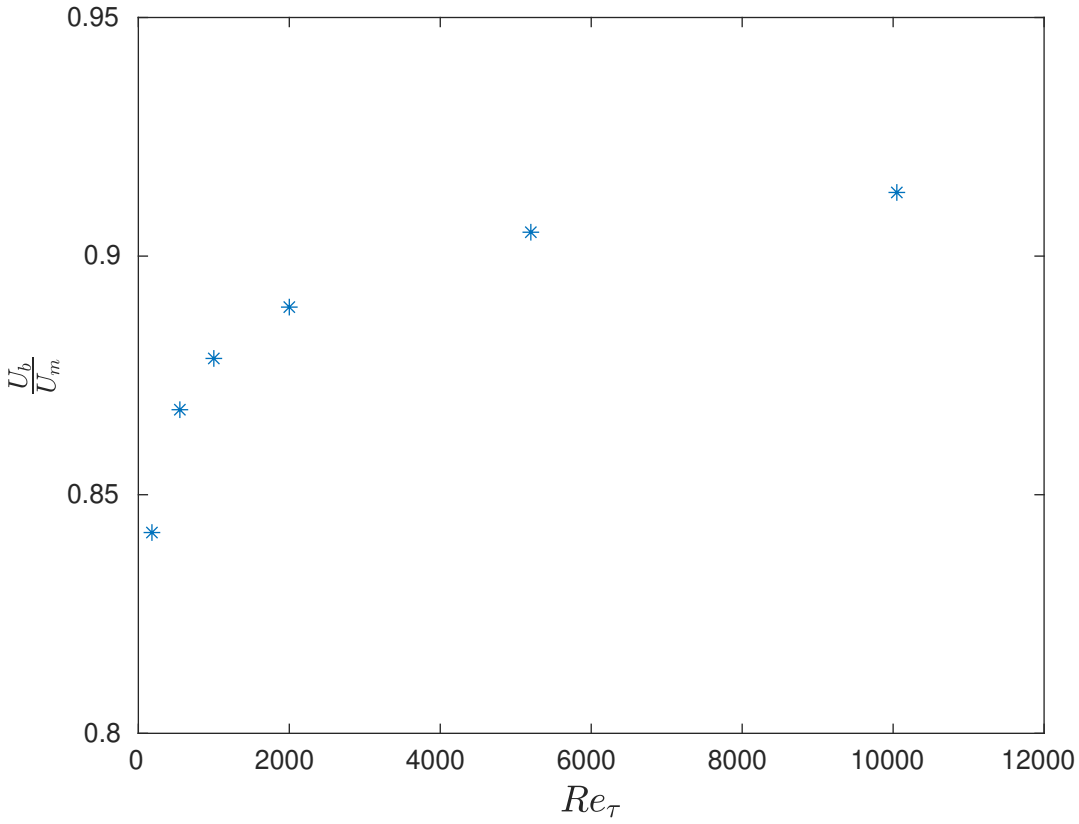

Figure 4.12: The ratio of average velocity U_b and maximum velocity U_m as a function of Re_τ.

suggests that perhaps U_* is influenced by a velocity scale that scales with ν/h. As U_m, the outer velocity scale, becomes dominant with increasing Reynolds number, the contribution of ν/h to U_* gradually diminishes to an asymptotic value but does not go to zero. This conclusion is supported by Morrison (2007). Therefore, hitherto formulations of the friction velocity do not represent this inherent coupling and U_* cannot be determined accurately unless molecular viscosity ν is considered. We are not aware of any prior relationships estimating the friction velocity that point to this fundamental lacuna. By addressing this gap, we show a significant improvement in calculating U_*.

Moreover, the use of h as the relevant length scale instead of the hydraulic radius R is a departure from the classical momentum balance approach (Eq. (4.8)). This is necessitated due to non-uniform distribution of shear stress along the wetted perimeter P. In both Eq.(4.11) and Eq.(4.8), U_* depends directly on the length scale, whether it is R or h. By definition, $h \geq R$. Since the maximum shear stress can be up to sixty percent higher than the average shear stress (Kartha and Leutheusser, 1970), using R for estimating U_* will always end up in underestimation of U_*. Even for the experimental validation of scaling laws, velocity profiles have relied on bed shear measurements that measure local shear stress (Smits et al., 2011; Schultz and Flack, 2013) (and not the average shear stress). We believe that perhaps the absence of a reliable measure of local shear stress must have compelled hydraulic engineers to use Eq.(4.8) to estimate U_*. However, in light of reasons discussed, the use of local friction velocity is more appropriate and can now be easily calculated utilizing the proposed OPFVM.

4.8 Limitations of this work

In nature, the boundary conditions and bed topography will influence the friction velocity estimation. Thus, caution must be exercised while using the OPFVM. The formulation for friction velocity reported in this paper is applicable only for fully developed channel flow in smooth or quasi-smooth beds. The accurate description of U_* highly depends on the development of the flow and the proposed formula, like any other method used in practice, will not work if the flow is developing or is under the influence of a downstream control. Additionally, this formulation is not

adequate for application in highly rough beds and tidally-driven flows. Further work needs to be done to extend the framework for universal application.

4.9 Conclusions and Recommendations

In this paper, we proposed a new OPFVM to calculate friction velocity that successfully overcomes the challenges posed by cumbersome near wall measurements. The method is tested using an additional DNS dataset of CCF and the friction velocity estimation was found to be within 1%. Then, the method was tested on a different DNS dataset for open channel flows and the estimated friction velocity was obtained within 1% of the exact value at $Re_\tau = 2000$. Further, the method was used to obtain friction velocity for experimental velocity profiles. The velocity profiles were non-dimensionalized using U_* and were found to follow the classical logarithmic scaling law for smooth walls as they collapsed on the DNS profiles. The profiles scaled by friction velocity obtained using log-law and average shear stress method did not collapse on the DNS profiles and had a deviation of more than 20%. Therefore, the OPFVM performed significantly better in comparison to existing methods and can prove to be a useful method for experimentalists and field practitioners alike. The calculation of discharge using a single measurement of U_m near the surface is also enabled by the proposed relationship between U_m and depth average velocity U_b.

Chapter 5

Improvement to RANS modeling using DNS data[4]

5.1 Purpose of the study

Reynolds Average Navier-Stokes (RANS) simulation of the fluid flow is integral to modern engineering design. It has enabled the application of Computational Fluid Dynamics (CFD) to various engineering problems. The current configuration of RANS model over-predicts the turbulent viscosity, affecting the accuracy of the model. To overcome the limitation, RANS users must calibrate their models to achieve desired results. Calibration is required to compensate for the inappropriate model constants used since the first estimate of the stress intensity ratio, five decades ago. Through this study, we motivate the need to update the value of C_μ to 0.06 to better align RANS models with the flow dynamics revealed through the latest DNS and show that the correction of turbulent viscosity parameter C_μ leads to better prediction of turbulent viscosity ν_T for wall-bounded flows. A similar correction is required for other canonical flows when suitable high-fidelity datasets are available. We hope that the insights from this paper will motivate the CFD community to revisit the other empirical constants used in RANS models to reflect the latest findings obtained from DNS and experiments that will keep the RANS modeling relevant.

5.2 Introduction

The $k-\epsilon$ model is one of the most popular turbulence models used in engineering over the last several decades to close the Reynolds Average Navier Stokes (RANS) equations. RANS turbulence models' robustness and computational efficiency have led to their wide acceptance in commercial codes. Even though they are imperfect, RANS models provide preliminary insights that greatly reduce the cost of engineering design for practical applications. However, in the last

[1]A substantial portion of this study has been published as Mishra, H., & Venayagamoorthy, S. K. (2024). On the turbulent viscosity parameter Cμ in the $k-\epsilon$ model. Flow, 4, E16. https://doi.org/10.1017/flo.2024.15

few decades, there has been little advancement in RANS modeling. The limitations of RANS models have not been adequately addressed and essential updates in light of improved experiments and Direct Numerical Simulations (DNS) have eluded the research community's focus. Therefore, due to stagnation in RANS modeling, the focus has now shifted to more computationally expensive techniques such as Direct Numerical Simulations (DNS) and Large Eddy Simulations (LES) (Bush et al., 2019) to solve the emerging problems in fluid dynamics.

We believe that RANS, while not a panacea, provides valuable insights into flows of practical interest as shown in recent works by Rodi (2017); Sinclair et al. (2022), and Boikos et al. (2024). Twenty years ago, Hanjalic (2005) correctly predicted that despite the growth of Large Eddy Simulations (LES), RANS will continue to be a popular design tool. Durbin (2018) highlighted that developments in RANS modeling have not kept up with their increasing use in the industry, and RANS will remain relevant for CFD applications. Therefore, instead of discarding them in favor of advanced techniques, critical revisits as shown in this paper, will improve RANS modeling and keep it relevant for solving engineering problems.

5.2.1 Mean Flow Equations

The fundamental laws that govern all flows are conservation of mass, momentum, and energy. The instantaneous velocity is decomposed such that the fluctuations are denoted u and v respectively and the mean flow equation is obtained by the technique called Reynolds averaging. Details of Reynolds averaging can be found in Kundu et al. (2015); Nezu and Nakagawa (2017). For a two-dimensional steady flow,

Conservation of mass

Consider the channel as shown in Fig.1.1.

$$\frac{dU_i}{dx_i} = 0 \tag{5.1}$$

This is known as the continuity equation in the differential form.

Conservation of momentum

The conservation of momentum is expressed by the Navier-Stokes equation for 2D steady flow with viscous and gravitational forces acting are given by :

$$U_j \frac{\partial U_i}{\partial x_j} = -g\delta_{i2} - \frac{1}{\rho}\frac{\partial P}{\partial x_i}\delta_{ij} + \frac{\partial}{\partial x_j}\left(2\nu S_{ij} - \overline{u_i u_j}\right) \tag{5.2}$$

$$\tag{5.3}$$

Here, P is the mean pressure, ρ is the fluid density, g is the gravitational acceleration, ν is the kinematic viscosity.

5.2.2 RANS modeling and $k-\epsilon$ model

RANS modeling is required to close the Reynolds stress term $\overline{u_i u_j}$ obtained by ensemble averaging of instantaneous Navier-Stokes equation. In a fully developed planar shear flow, as discussed in this paper, the non-diagonal terms of tensor $\overline{u_i u_j}$ reduce to $\overline{uw}$. Here u_i is the velocity fluctuation, with u, v, and, w, are fluctuations in the streamwise, spanwise, and wall-normal directions, respectively. Among different techniques used to model the Reynolds stress term (refer Pope (2000) and Durbin and Shih (2005) for an overview of closure methods), the $k-\epsilon$ model (Launder and Spalding, 1974) has emerged as one the most ubiquitous and popular closure model.

5.2.3 Turbulent energy and its transport

For 2D fully developed flows, the rate of turbulent kinetic energy (TKE) production P and rate of direct dissipation ϵ of TKE are given by

$$P \equiv -\overline{uw}\frac{dU}{dz} \tag{5.4}$$

$$\epsilon \equiv \nu\left(\frac{dU}{dz}\right)^2 \tag{5.5}$$

These two components are extracted from the mean flow energy. The mean flow energy can be lost via viscous dissipation directly or by the generation of turbulent kinetic energy (TKE). This TKE is generated at the large scale and cascades to smaller scales. It is lost by heat due to molecular viscosity (Pope, 2000) The schematic mechanism of turbulent energy transport is given in Fig 5.1 (Nezu and Nakagawa, 2017) [2]. Using the turbulent viscosity hypothesis (TVH) in a linear eddy-viscosity model, the Reynolds stress $\overline{uw}$ is expressed in terms of turbulent viscosity ν_T and mean shear $S = \frac{dU}{dz}$, where U is the mean streamwise velocity, as

$$\overline{uw} = -\nu_T \frac{dU}{dz}. \tag{5.6}$$

For closure, S can be measured but ν_T needs to be estimated. Dimensional reasoning implies that $\nu_T \sim [L^2/T] \sim [L/T \times L]$, therefore, ν_T can be expressed as a product of a length scale l^* and a velocity scale u^*. As suggested by Kolmogorov (1941) and Prandtl (1945), u^* can be assumed to scale as $ck^{1/2}$, where $k = \frac{\overline{u_i u_i}}{2}$ is the turbulent kinetic energy. In the near-wall region, $u^* = l^* S$. From the definition of ν_T, (Eq.(5.6)), $u^* = \left(\overline{|uw|}\right)^{1/2}$. Thus, $c = \left(\frac{\overline{|uw|}}{k}\right)^{1/2}$ and its square $c^2 = \frac{\overline{|uw|}}{k}$, is called the stress-intensity ratio. If a length scale l^* is defined, then the transport equation for k can be solved. Under the assumption of equilibrium (Richardson-Kolmogorov cascade), $\epsilon \sim u^{*3}/l^* \Rightarrow \epsilon \sim k^{3/2}/l^* \Rightarrow \epsilon = Ck^{3/2}/l^*$, where C is another model constant. Therefore,

$$\nu_T = cC\frac{k^2}{\epsilon}. \tag{5.7}$$

Alternatively, as suggested by Harlow and Nakayama (1968), $\epsilon \sim \frac{k^{3/2}}{l^*} \Rightarrow l^* \sim \frac{k^{3/2}}{\epsilon}$. Since $u^* \sim k^{1/2}$, $\nu_T \sim \frac{k^2}{\epsilon}$. By assuming that ν_T depends only on k and ϵ, a turbulent viscosity parameter, C_μ, is introduced to obtain Eq.(5.8).

$$\nu_T = C_\mu \frac{k^2}{\epsilon}. \tag{5.8}$$

[2]The original volume was published in 1993 as a monograph of IAHR

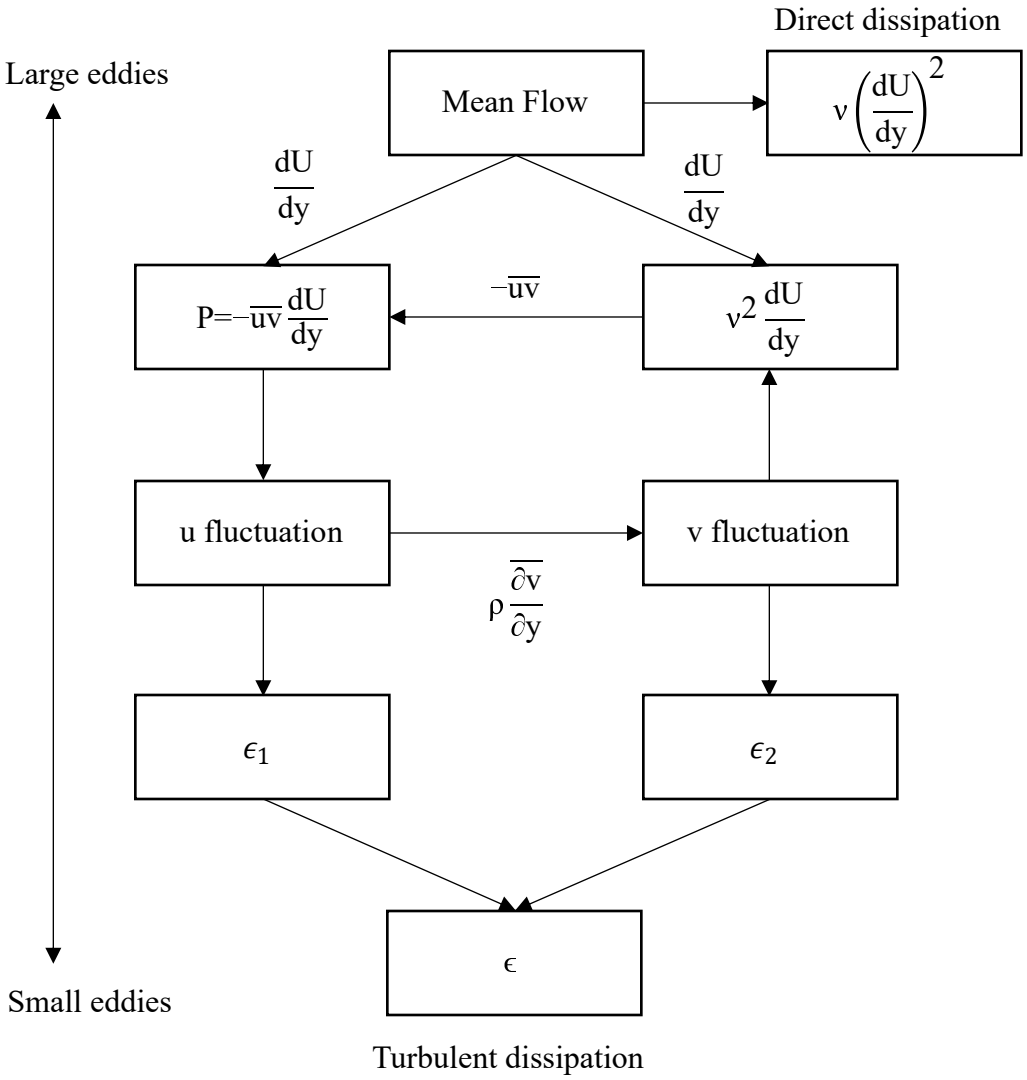

Figure 5.1: Schematic mechanism of turbulent energy transport (adopted from Nezu and Nakagawa (2017))

Eq.(5.8) is the specification of ν_T in the $k-\epsilon$ model. The standard $k-\epsilon$ eddy-viscosity model uses $C_\mu = 0.09$, proposed by Jones and Launder (1972). From Eq.(5.6) and Eq.(5.8), $C_\mu = -\frac{\overline{uw}}{Sk^2/\epsilon}$. Evidently, this is not a constant. To obtain closure for $\overline{uw}$, an independent estimation of C_μ is required. After the initial proposal of a constant C_μ, a minor correction to the C_μ was implemented based on the turbulent Reynolds numbers $Re_T = k^2/\nu\epsilon$ for low-Reynolds number flows such that at higher Re_T, C_μ approached 0.09 (Jones and Launder, 1973). For free shear flows, a correction to C_μ based on Rodi (1972)'s work was made by Launder et al. (1973) based on S. Additionally, in wall-bounded flows, to improve the near-wall behavior, parameterization of C_μ in terms of S was proposed by Cotton et al. (1992) and later improved by Cotton and Ismael (1998); Suga (1995); Karimpour and Venayagamoorthy (2014). Further, Reynolds (1987) and Shih et al. (1995) have argued that parameterization of C_μ is necessary as the model becomes unrealizable in the presence of a large S due to reduction in the value of C_μ. However, the parameterization of C_μ has not been popular because away from the wall, S reduces dramatically and poses numerical challenges in the implementation. Further, all such parameterizations of C_μ have not been derived independently but are based on the local equilibrium value of 0.09. We will henceforth demonstrate the inaptness of the hitherto used value of $C_\mu = 0.09$ using an *a-priori* test and suggest improvements.

5.2.4 *A-priori* test of ν_T using DNS data

We perform an *a-priori* test using the DNS of high Reynolds number channel flow ($Re_\tau = 10000$). In Fig 5.2, it is evident that $C_\mu = 0.09$ causes an over-prediction of ν_T by almost 50%. Thus, the current value of C_μ must be revised to align RANS model with the latest experimental and DNS values.

5.2.5 Equilibrium region and relationship between c, C and C_μ

The transport equation of k for a fully developed flow contains production $\mathcal{P} = -\overline{uw}S$ and dissipation rate term ϵ. When $\mathcal{P} \approx \epsilon$, the flow is said to be in equilibrium. The dissipation follows the Richardson-Kolmogorov cascade (Vassilicos, 2015). Fig. 5.3 shows the ratio $\mathcal{P}/\epsilon$ for different Re_τ across the depth of the flow. For the majority of the flow depth, $\mathcal{P}$ is within 10% of ϵ. We

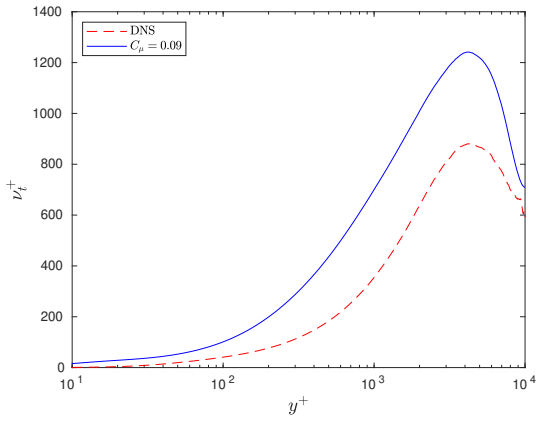

Figure 5.2: *A-priori* test showing the turbulent viscosity ν_T using DNS data for $Re_\tau = 10000$ (Hoyas et al., 2022).

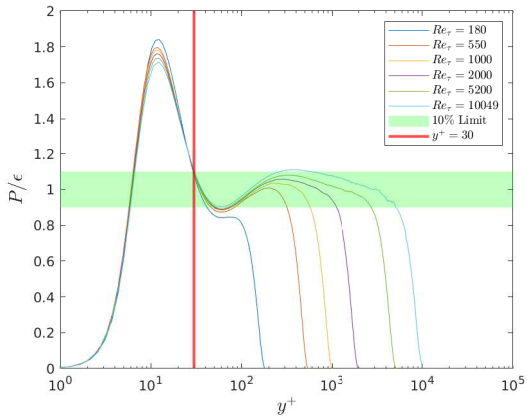

Figure 5.3: The ratio of production to dissipation of the turbulent kinetic energy P/ϵ for different Re_τ values from DNS of channel flow. The equilibrium region with 10% tolerance is shown in the green patch.

know that in the logarithmic region, $u^* = l^* S \Rightarrow l^* = u^*/S$. By equating Eq.(5.8) and Eq.(5.6), and using $u^* = ck^{1/2}$, we get $C = c^3$. Therefore, by careful rearrangement and substitution, the relationship between constants c, C, and C_μ, as shown in Eq.(5.9) and Eq.(5.10), are obtained.

$$c^2 = C_\mu^{1/2} \left(\frac{\mathcal{P}}{\epsilon} \right)^{1/2}, \tag{5.9}$$

with $\mathcal{P} \approx \epsilon$,

$$C_\mu \approx c^4. \tag{5.10}$$

The value of the turbulent viscosity parameter C_μ has been determined using empirical estimates

of the stress intensity ratio c^2. The hitherto value of C_μ emanates from the experimental findings of Champagne et al. (1970), who reported asymptotic values of $\overline{|uw|}$, u, v, and w using wind-tunnel experiments from which c^2 could be calculated as 0.32 for $Re_\tau \approx 3000$. Jones and Launder (1973); Launder and Spalding (1974) used 0.33 to close their model. The experiments by Harris et al. (1977); Tavoularis and Corrsin (1981) confirmed the findings of Champagne et al. (1970) at low Reynolds numbers. Even before Jones and Launder (1972), Bradshaw et al. (1967) used an approximate value of 0.3 to substitute for c^2, but he cautioned against indiscriminate use of this constant. Later, Yakhot and Orszag (1986) theoretically derived a value of $C_\mu = 0.085$ for a variant of $k - \epsilon$ model for large Reynolds number flows. As will be shown later, turbulent viscosity ν_t predicted using $C_\mu = 0.085$ does not agree with the high Reynolds number DNS results. Thus, Champagne et al. (1970)'s experimental observations are unsuitable for high Reynolds numbers flows. The latest findings using the DNS datasets suggest much lower values of c^2, as shown in Fig 5.4a and Fig 5.4b.

In Fig 5.4a, it can be observed that c^2 is not a constant, and the peak is just under 0.25. Moreover, as inferred from Fig 5.4b, the peak values of c^2 decrease with increasing Re_τ, and even for the lowest $Re_\tau = 180$, the peak is lower than 0.3. Therefore, C_μ must be less than 0.09 (Eq.(5.10)). Recently, Xu et al. (2020) analyzed the behavior of c^2 for different canonical flows but did not discuss its implication on C_μ.

Despite their limitations, linear eddy-viscosity models, such as the $k - \epsilon$ model have been extremely popular because of the ease of implementation and their computational efficiency. Therefore, a constant C_μ simplifies the model and adds to its acceptance in widely used commercial codes. However, since c^2 is not a constant, using an obsolete constant for C_μ can lead to high uncertainties in the RANS model. Duraisamy et al. (2019) have emphasized that model constants (C_μ, $C_{\epsilon 1}$ etc.) are the major source of uncertainty in RANS modeling. Several works have attempted to quantify the uncertainty in RANS models due to the model constants using statistical methods such as Emory et al. (2013); Edeling et al. (2014); Poroseva et al. (2016); Wang et al.

(2016). The major takeaway from these studies is that the uncertainty in RANS model constants can be very high. Our finding demonstrates that the uncertainty is as high as 50%.

Improvements in model constants have been attempted as multi-parameter optimization problems without considering the physics of the flow. Poroseva et al. (2016) highlighted the uncertainties in the model using DNS data for low-Reynolds number Zero Pressure Gradient flows to suggest an improved RANS-DNS framework. Xiong et al. (2022) recommended optimizing the closure coefficients to improve the accuracy using statistical methods. Ling et al. (2016); Pan and Duraisamy (2018); Sotgiu et al. (2019); Li et al. (2022); Yan et al. (2022); Bounds et al. (2023); Heo et al. (2024) have leveraged neural networks and machine learning to train models using the DNS data. Wang et al. (2017) attempted physics-informed machine learning of the LES/DNS data to obtain better coefficients.

Barring Eisfeld (2022), who discussed the importance of equilibrium region in turbulence modeling at high Reynolds numbers, the context of equilibrium, or broadly flow physics, has escaped the eyes of other researchers. While evaluating the performance of machine learning algorithms, even Ling and Templeton (2015) have highlighted that the machine algorithms are opaque and physical insights are necessary.

Even though uncertainty in model constants has been studied extensively, to our knowledge, no recommendation has been made to update model constants that align RANS models with the state-of-the-art understanding of flow physics to improve their performance. The outcomes of statistics/ML studies have, at best, demonstrated the need to tighten the uncertainty. In the absence of consensus on the new value, the standard textbooks on turbulent flows (such as Pope (2000) and Durbin and Reif (2011)) have continued to recommend C_μ=0.09. However, considering the strong evidence, C_μ must be updated to a more physically appropriate value. Thus, we adopt a novel, yet simple methodology to evaluate C_μ as discussed in the following section.

5.3 Towards a new value of C_μ

The equilibrium assumption ($\mathcal{P} \approx \epsilon$) holds well within the limit of 10% beyond $y^+ = 30$, which marks the well-accepted onset of the logarithmic layer. Even though c^2 is not a constant, the average value of c^2 over the equilibrium region can provide a good estimate for C_μ.

We define a function g such that,

$$g = \begin{cases} c^2, & 0.9 \leq \mathcal{P}/\epsilon \leq 1.1 \\ 0, & \text{otherwise} \end{cases} \tag{5.11}$$

Then,

$$\overline{c^2} = \overline{g} \tag{5.12}$$

Here, $\overline{g}$ is the average of g in the range shown in Fig 5.3. Thus, using the value of c^2 obtained from Eq.(5.12) in Eq.(5.10), the required value of $\overline{C_\mu}$ for different Re_τ is obtained as shown in Fig. 5.5.

5.4 Results and Discussion

Fig 5.5 suggests that $\overline{C_\mu}$ approaches 0.06 at $Re_\tau = 5000$ and remains unchanged thereafter. Therefore, at sufficiently high Re_τ, $\overline{C_\mu}$ should become a constant i.e. $C_\mu = 0.06$, against the parameterization suggested by Launder and Sharma (1974) in terms of turbulent Reynolds number $Re_T = k^2/\nu\epsilon$. For low Reynolds numbers, c^2 corroborates the prevalent value of 0.3.

Townsend (1976) reported the average stress-intensity ratio $c^2 = 0.26$ for all canonical flows. The corresponding C_μ as per Townsend (1976)'s $c^2 = 0.26$ would be 0.067, which is in close agreement with the trend shown in Fig 5.5.

The impact of choosing $C_\mu = 0.06$ on predicting ν_T is shown in Fig 5.6. For $Re_\tau = 10000$, $C_\mu = 0.06$ provides a closer agreement with the exact (DNS). Even though the near-wall prediction is still compromised due to high S (Karimpour and Venayagamoorthy, 2013, 2014), it is much better in comparison to the classical value of $C_\mu = 0.09$. Also, the new value aligns with the

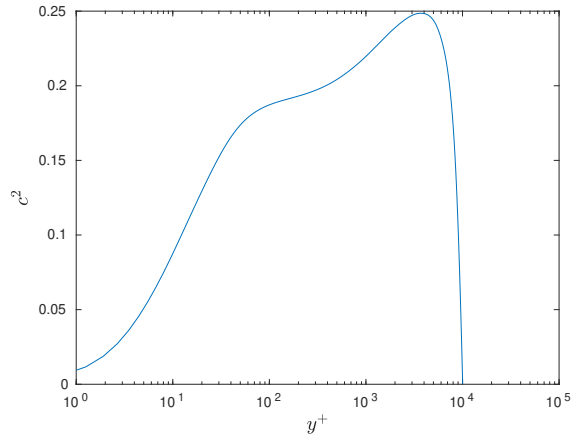

(a)

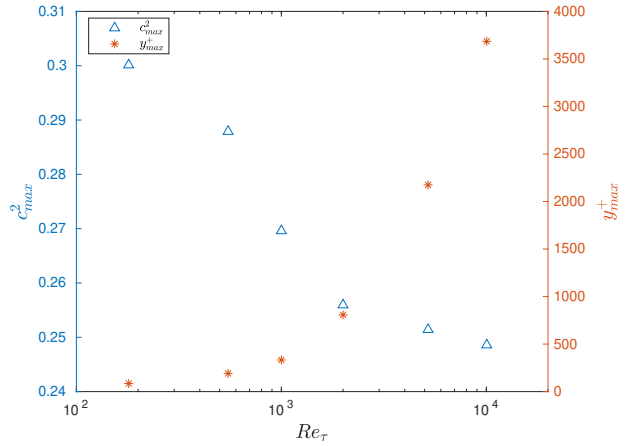

(b)

Figure 5.4: (a) Variation of $c^2 = |\overline{uw}|/k$ is plotted at $Re_\tau = 10000$ from DNS data (Hoyas et al., 2022) ; (b) The maximum values c^2 are plotted with increase in the Re_τ as given by the left vertical axis and their corresponding locations are also plotted as given by the right vertical axis.

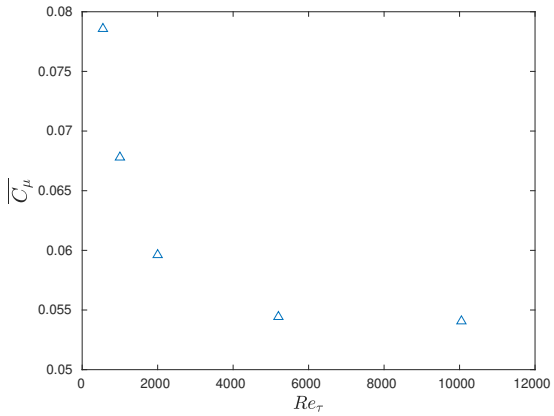

Figure 5.5: A plot of C_μ obtained using the value of c^2 averaged over the equilibrium region as shown in Fig 5.3.

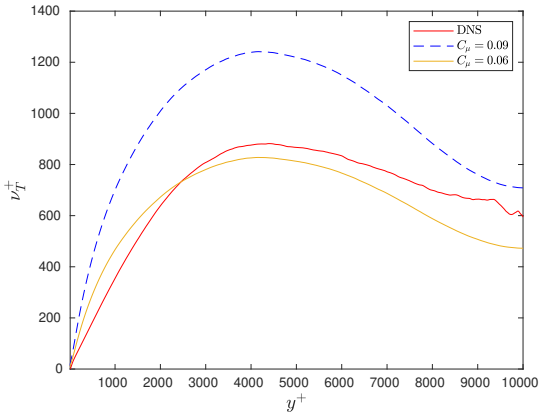

Figure 5.6: *A-priori* comparisons of ν_T with different values of C_μ using DNS data for $Re_\tau = 10000$ (Hoyas et al., 2022)

physics of the turbulent flows as revealed by recent DNS. In the atmospheric science community, c^2 is recommended as 0.17 for low Richardson number flows (Mauritsen et al., 2007; Wilson and Venayagamoorthy, 2015). However, because of the inevitable shear layer in the outer region of the flow, it is questionable whether a robust recommendation can be made using the atmospheric boundary layer data. Recently, Eisfeld (2022), in his analysis, used the experimental values of Bradshaw et al. (1967) for the turbulent boundary layer and Delville et al. (1987) for the plane mixing layer. While the turbulent boundary layer problem was at a very low Reynolds number, the values for the plane mixing layer have high uncertainties, leading to higher values of c^2. Against Shih et al. (1994)'s proposal of parameterizing C_μ and introducing additional constants, the reduction in C_μ can be captured by changing the constant from 0.09 to 0.06.

Physically, a higher C_μ amplifies the turbulent viscosity based on the calculated values of k and ϵ. In a coarse grid, k and ϵ are poorly resolved and the amplification of ν_T does not hamper the stability of the numerical code. However, in a finer mesh, k and ϵ are better resolved, and a higher C_μ destabilizes the code. Grid refinement in RANS models is primarily aimed at numerical accuracy. Ideally, a robust solution should be achievable on infinitely finer meshes, provided the other necessary numerical conditions (such as the Courant condition) are satisfied. However, obtaining grid independence in RANS models is challenging (Celik, 2003; Diskin et al., 2015). Improving closure constants could be a way to allow easier convergence with finer meshes.

A higher C_μ can also deteriorate the accuracy of the solution. For example, in a pollutant transport model, the model will show an early disappearance of the pollutant while it is still being transported (Mazarakis et al., 2016) due to artificial diffusion caused by higher ν_T. This discrepancy has so far been handled through the calibration of models. Even though re-tuning of other closure constants (such as $C_{\epsilon 1}$, $C_{\epsilon 2}$, σ_ϵ) will be required to ensure complete accuracy, updating the turbulent viscosity parameter C_μ should be prioritized to ensure alignment of the $k-\epsilon$ model to the flow physics.

The existence of an asymptotic limit of c^2, as shown in Fig 5.5 can be explained using boundedness of turbulent quantities (Busse, 1970). Since $c^2 = \overline{|uw|}/k$, $\overline{uw} \approx U_\tau^2\,(1 - z/h)$, where

U_τ, z, and h are the friction velocity, distance from the wall, and the depth respectively, we can deduce stress-intensity ratio, $c^2 \approx \frac{(1-z/h)}{\overline{k^+}}$. Recently, using the DNS data, Chen and Sreenivasan (2022) proposed a 'final state' of turbulence against the existing theory of endless variation. They argued that all wall quantities are bounded in the limit of an infinite Re_τ. Klewicki (2022) has supported this idea but has pushed for stringent DNS at higher Re_τ to confirm this theory. The bounds suggest an asymptotic limit of k^+. By similar reasoning, if $\lim_{Re_\tau \to \infty} \overline{k^+} = A(z/h)$, $\lim_{Re_\tau \to \infty} c^2 = \frac{(1-z/h)}{A(z/h)}$, where A is the asymptotic function of $\overline{k^+}$ over z. If all bounded quantities asymptote, then the equilibrium region $\mathbb{R}$ should also be identical. Thus, $\overline{c^2} = \overline{\frac{(1-z/h)}{A(z/h)}|_{\mathbb{R}}} = B$, where B is the asymptotic limit of c^2 in the equilibrium region. We do not yet know A and B, but the data suggests that such an asymptotic function is plausible. We find Chen and Sreenivasan (2022) 's theory intuitive and aligns with the trends shown by state-of-the-art DNS and experiments.

5.5 Limitations and future work

The standard $k-\epsilon$ model's performance deteriorates in detached boundary layers, adverse pressure gradients, and free-shear flows (Eisfeld, 2021). The values of C_μ could vary widely in free-shear flows as reported by Lefantzi et al. (2014). Thus, even though the methodology has wider applications, the findings of this paper are strictly applicable only to the attached wall-bounded turbulent flows. More experimental and DNS data are required to obtain a universal value of C_μ. Further, it is cautioned that merely changing C_μ to 0.06 might lead to inferior results because the other constants in the $k-\epsilon$ model have been tuned by fixing $C_\mu = 0.09$. Therefore, a wider comprehensive effort is required to re-tune the coefficients by setting C_μ to 0.06. This paper emphasizes that the parameter C_μ needs to be corrected first based on the latest DNS data. The fine-tuning of the model can be performed later once an agreement is achieved on the value of C_μ.

5.6 Conclusion

Using the data from DNS of highly turbulent channel flows, we have demonstrated that the current specification of turbulent viscosity parameter $C_\mu = 0.09$ in $k - \epsilon$ model overpredicts the turbulent viscosity ν_T. We revisit the original specification of C_μ based on stress intensity ratio $c^2 = |\overline{uw}|/k$ in the equilibrium region and find that even the maximum values of c^2 at high Reynolds number do not support the existing proposition of $C_\mu = 0.09$. We calculate a more appropriate value of $C_\mu = 0.06$ by averaging the stress intensity ratio c^2 in the equilibrium region with a tolerance of 10%. A test using the new value of C_μ shows closer agreement with the exact values of ν_T obtained from the DNS in channel flows. Analysis has been presented to support the proposed modification to the $k - \epsilon$ model using the latest findings in the literature on turbulence theory. The trend suggests an asymptotic value of C_μ closer to 0.06.

Chapter 6

Alternate scaling of mean velocity profiles in wall-bounded flows[5]

6.1 Introduction

As per the prevalent understanding of wall scaling, all wall-bounded flows are classified into near and outer wall regions. The near wall is scaled by parameters kinematic molecular viscosity ν and the friction velocity, U_*. The velocity scale is taken as U_*, and the corresponding length scale is given by $\delta_\nu = \nu/U_*$. Therefore, the near-wall scaling is given as, Therefore,

$$U^+ = f\left(\frac{zU_*}{\nu}\right) = f(z^+) \tag{6.1}$$

Here z is the distance from the wall.

Based on Eq. (6.1), the near-wall region is classified into the viscous sublayer and the buffer layer.

- Viscous Sublayer : Extends upto $z^+ \approx 5$ and scales as $U^+ = z^+$.
- Buffer Layer: The buffer layer is considered up to $z^+ \approx 30$ with the appropriate scaling yet to be fully understood.

The outer region comprises the log layer, which begins after the buffer layer, and the wake region close to the maximum flow depth in channels (for pipes, it is close to the centerline). The log layer is called the overlap region, where the inner and outer scales interact. The influence of flow scales and associated regions are shown in Fig 6.2. The log-law scaling for smooth wall-bounded flows is given by:

$$U^+ = \frac{1}{\kappa}\log(z^+) + B \tag{6.2}$$

[2]A significant portion of this study will be submitted to *JFM-Rapids* with co-author S.K.Venayagamoorthy.

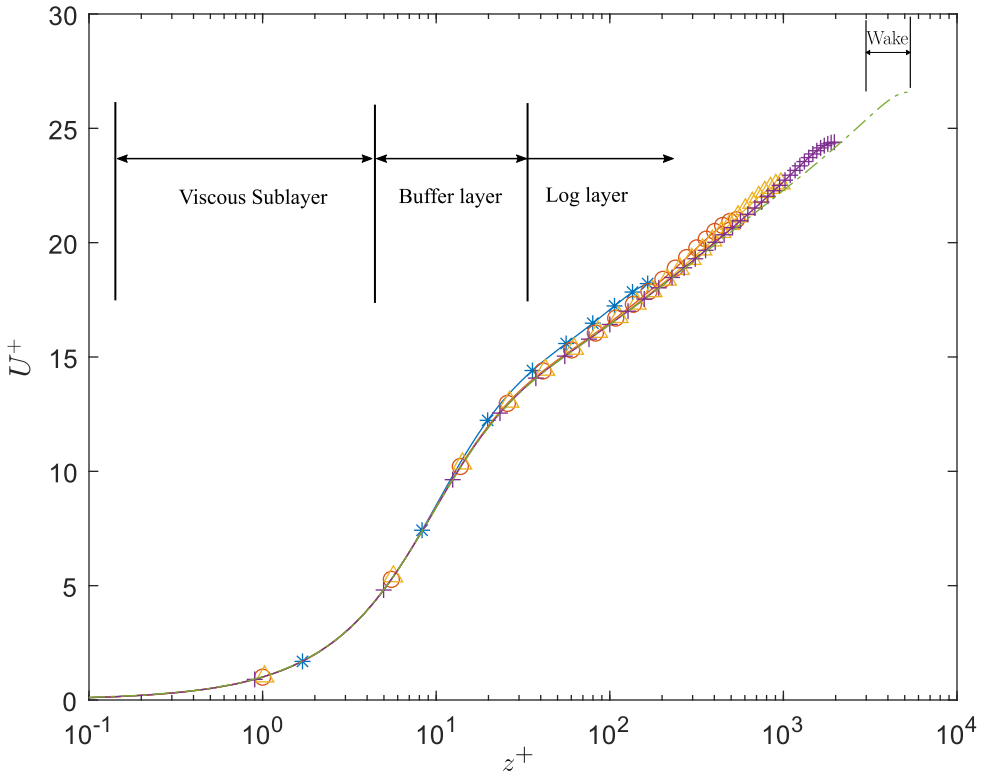

Figure 6.1: Classical scaling of wall-bounded turbulent profiles

Here, $U^+ = \dfrac{U}{U_*}$, $z^+ = \dfrac{zU_*}{\nu}$, κ is von-Karman's constant ($\approx$0.4) and B is the Townsend and Perry constant, typically taken as 5.5.

The development of the turbulent boundary layer in wall-bounded flows and the interaction of the two regions have not been fully understood. The inner wall scaling is based on the mixing length hypothesis. In this paper, a different approach is taken to understand the scaling of wall-bounded turbulence. We assume the outer region scales with the maximum free-stream velocity U_m. This could be the centerline velocity in pipe flows or surface velocity in open-channel flows. The inner-region scales with $U_* Re_\tau$. We hypothesize that both scales influence the flow, except at the extremes. This hypothesis is against Townsend (1961)'s hypothesis, which suggests that inner and outer flows become independent after the flows reach a certain Reynolds number.

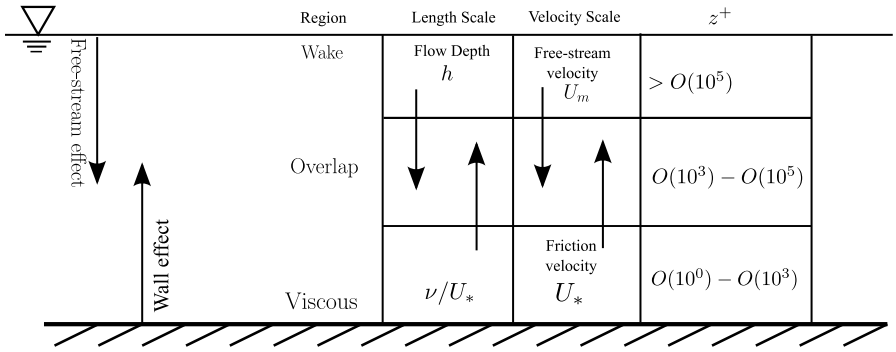

Figure 6.2: Classical scaling of wall-bounded turbulent profiles

6.2 Scaling parameters

It is hypothesized that the velocity profile can be considered as a projection of the inertial velocity scale U_m and the viscous velocity scale $U_*^2/(\nu/h) = U_* Re_\tau$. This comes from rearranging the empirical relationship $z^+ = U^+$. We will obtain the velocity at any depth $\varsigma = z/h$, where z is the wall-normal distance and h is the depth of the flow by considering a hyperbolic angle α defined such that $\tanh\alpha = \sqrt{1-\varsigma^2}$. The approach taken here is inspired by Lorentzian transformations in the hyperbolic space (Victoria and Caja, 2010). Then, the projection of U_m on the hyperbolic asymptotic plane will be given by $U_{fo} = U_m \cosh\alpha$. Now, the projection of the inner scale is not straightforward. We define an angle such that $\sinh\beta = \sqrt{1-\varsigma^2}$. The projection of $U_* Re_\tau$ can be obtained as $U_{fi} = U_* Re_\tau \coth^2\beta$.

Therefore, let us call the new scaled velocity as

$$U^{\otimes} = \frac{U}{U_f} = \frac{U}{U_{fo}} + \frac{U}{U_{fi}} \tag{6.3}$$

From (6.3),

$$\frac{1}{U_f} = \frac{1}{U_m \cosh\alpha} + \frac{1}{U_* Re_\tau \coth^2\beta} \tag{6.4}$$

The individual scaling factors have been plotted in Figs 6.3 for DNS profiles. It can be seen that the contribution of the inner velocity scale U_{fi} diminishes with an increase in Reynolds numbers. The outer scale dominates for most part of the flow except very near to the boundary.

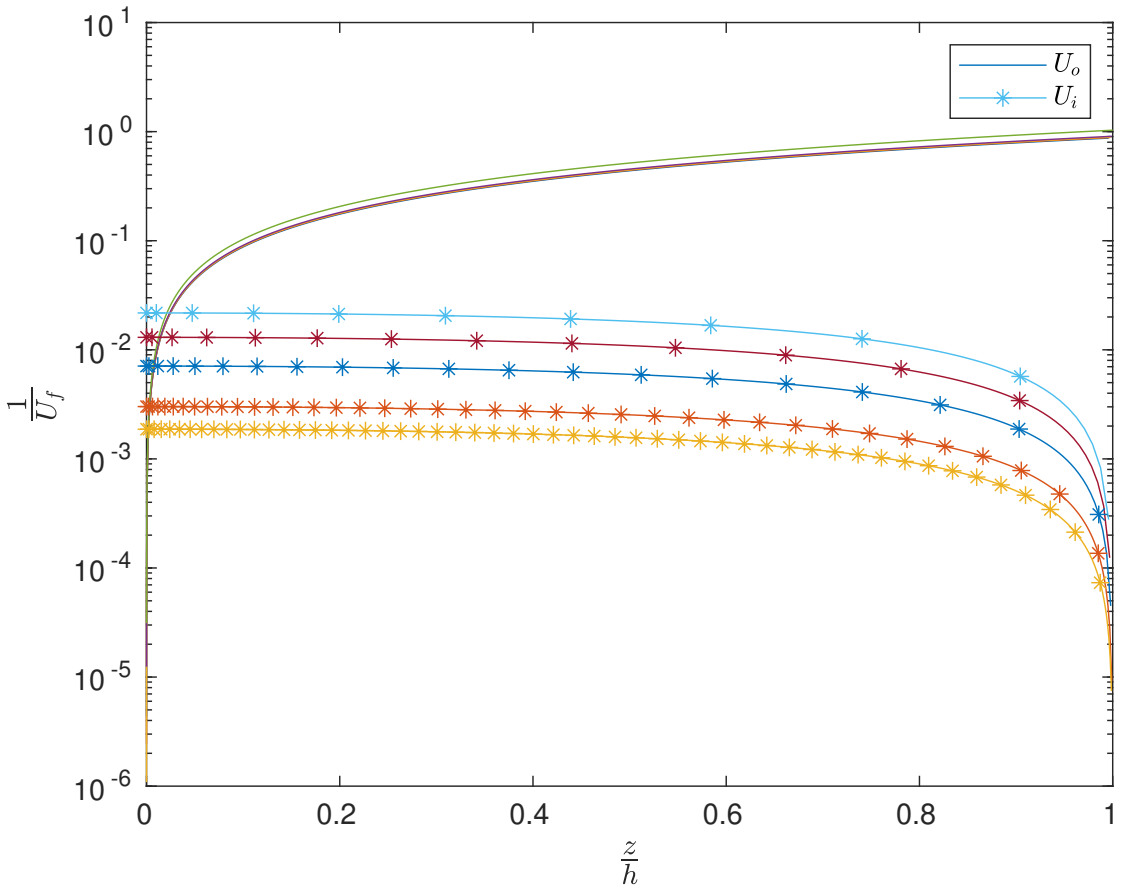

Figure 6.3: The plot of inner velocity scale U_{fi} and outer velocity scale U_{fo} calculated for DNS channel data for $Re_\tau \sim 550 - 10000$. The orange asterisk line represents $Re_\tau \approx 10000$ and the blue asterisk line represents $Re_\tau \approx 550$.

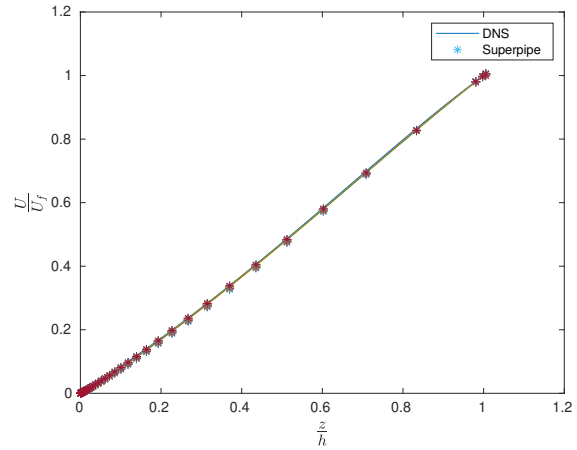

(a)

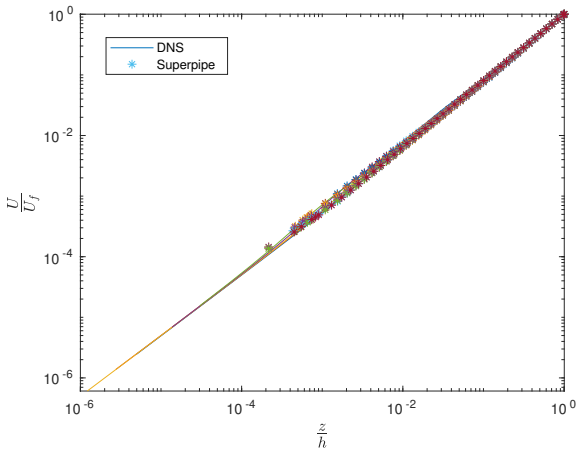

(b)

Figure 6.4: Plot of scaled velocity profiles using scaling factor U_f in (a) normal scale (b) log-scale for DNS datasets with $Re_\tau \sim 550 - 10000$ and superpipe data for $Re_\tau \sim 1900 - 98000$.

6.3 Results

Based on the individual scaling suggested in the previous sections, we take the DNS datasets provided by Lee and Moser (2015); Hoyas et al. (2022) and superpipe data by Zagarola and Smits (1998) and scale it using Eq.(6.4). The scaled velocity profiles are shown in Fig 6.4a and Fig 6.4b. All the velocity profiles collapse perfectly on one plot, thereby eliminating the need for κ and B. Using the log-log graph, the slope of the plot can be calculated as ≈ 1.075. Therefore, the resultant

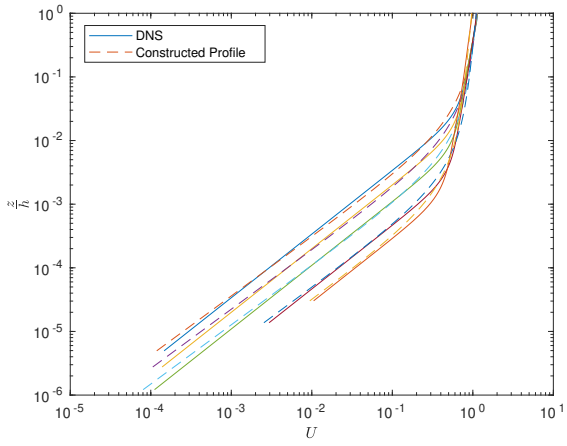

(a)

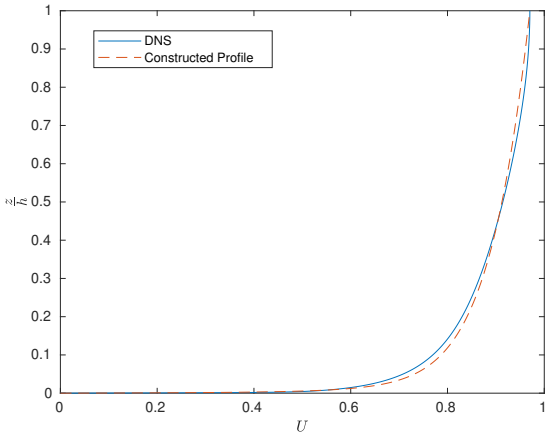

(b)

Figure 6.5: Plot of reconstructed velocity profiles using scaling factor U_f in (a) log-log scale for all DNS profiles with $Re_\tau \sim 550 - 10000$ (the blue lines denote $Re_\tau \approx 550$ and the orange denote $Re_\tau \approx 10000$) (b) for $Re_\tau \approx 10000$ on normal scale

velocity profile can be constructed using the following relationship.

$$U = U_f \varsigma^{1.075} \tag{6.5}$$

Using Eq.(6.5), a velocity profile is constructed for DNS channel data $Re_\tau \sim 550 - 10000$ as shown in Figs 6.5a and 6.5b. It can be seen the profiles are well reconstructed using the given formulation.

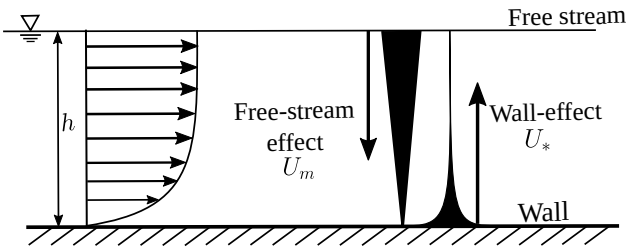

Figure 6.6: New conceptualization of inner and outer scale interactions in wall-bounded flows.

6.4 Discussion

This work highlights that the description of velocity profiles in wall-bounded regions is possible using a single mixed scaling factor. In this approach, we have eliminated the need to express the distance from the wall in terms of wall units. It was obvious that the near-wall region is affected by the Reynolds number, and a universal scaling law concealed that fact by defining wall units as local Reynolds numbers $z^+ = U_* z/\nu$. It is incorrect to call Eq (6.2) as a universal law because it operates in a very specific region. In Fig 6.5a, the log-log plot suggests regions of two slopes: one with the viscous effect and the other affected by free-stream velocity U_m.

The velocity scaling function emphasizes that the two scales add harmonically. At high enough Reynolds numbers, the term U_{fi} will diminish, and the velocity profiles can be approximately scaled by only U_m. This is the first work that has described the entire velocity using a single scaling function with minimal empiricism. The elegant mathematical relationship is not only simple but also elucidates the underlying flow-physics. Based on the findings of this paper, the conceptual understanding of wall-bounded flows can be better illustrated by Fig 6.6.

6.5 Limitations

The given equation has a small empiricism, as the slope of the log-log curve varies between 1 and 1.1. Further tightening of the construction can be done to obtain a perfect collapse with a 1:1 slope.

6.6 Conclusion

A new formulation of the velocity scaling function has been proposed using inspiration from Lorrentzian transformations and projection on hyperbolic space. This scaling function is constructed by first obtaining inner and outer velocity scales. The final velocity function scales the mean velocity profiles remarkably well for a large range of Re_τ. Further, the velocity profiles are reconstructed using the scaling function, and they show excellent agreement without the need for any arbitrary constants such as κ and B. This is the first single formulation for the entire velocity profile reported in the literature, which is simple enough to explain the underlying flow physics.

Chapter 7

Conclusions and future work

In this dissertation, data from direct numerical simulation, laboratory experiments, and RANS simulations have been used to address four standing challenges in wall-bounded turbulence. A contribution has been made to all three investigation methodologies employed in fluid mechanics and hydraulic engineering, i.e., laboratory experimental methodology, field measurements, and computational fluid dynamics, in the context of wall-bounded turbulence.

In chapter 1, the importance of wall-bounded flows in civil engineering applications has been discussed, and the relevance of the four important contributions has been highlighted. The relevant literature review has been incorporated in each of the following chapters.

In the first study described in chapter 2, an optical device was developed to enable particle-image velocimetry (PIV) in free-surface flows. This device helps conduct PIV experiments in a wide range of flow conditions where laser passage through the bottom of the flume is obstructed. The new device has been named a 'coupler'. Since the device interacted with the free surface, the influence of the coupler was evaluated on four regimes with different relative surface wave celerity. The chapter will be submitted to the journal - *Experiments in Fluids* for consideration for publication.

The third chapter (3) details the study on flow development in smooth channels. This work is significant in light of a raging debate in the scientific community concerning the adequacy of short laboratory flumes for experimental investigations. The study presented in this dissertation provides a simple method to obtain fully developed flow in short channels by suitably modifying the inlet and tripping the boundary layer by a sharp roughness element. The flow development was confirmed using the turbulent channel DNS data.

The next study further utilizes the turbulent channel DNS data to provide insights on measuring the friction velocity U_* in smooth turbulent channel flows. The details of this study are explained in Chapter 4. This study enables the measurement of friction velocity using the free-stream surface

velocity U_m and the depth of the channel h. It is useful for practicing engineers and laboratory experimentalists alike, who, hitherto, face enormous difficulty in calculating critical flow parameters such as U_*. The estimation of U_* was experimentally confirmed using laboratory experiments. This study has been published in *Journal of Hydraulic Engineering (ASCE)*.

In the fourth study described in Chapter 5, we show that a key parameter used to close the Reynolds-stress equations in the popular $k - \epsilon$ turbulence model is inappropriate in light of the latest DNS and experimental findings. A new value for the parameter C_μ has been suggested, along with some simulations that show improved model performance in terms of numerical fidelity.

In the final study discussed in chapter 6, a scaling law has been developed using an outer velocity scale U_m, length scale h, and inner velocity parameters U_* and ν. We show that the velocity profiles can be produced by using hyperbolic functions of local depth. This is a step forward in analytically understanding the contributions of inner and outer scales. Using such a scaling, in the limit of infinite Reynolds numbers, self-similar profiles can be obtained only in terms of the outer layer.

7.1 Key contributions

Among the four studies conducted, the key contributions to fluid mechanics and the hydraulics community are listed below:

1. A new device has been developed to extend particle-image velocimetry to laboratory flumes with an opaque bed by bringing a laser through the free surface. Thus, PIV can be effectively used to investigate flows with different bed configurations.
2. A methodology has been developed to utilize short laboratory flumes for experimental investigations against the prevalent thought in the research community that considers short flumes inadequate. The flow is engineered such that the flow development takes place quickly by tripping the boundary layer.
3. A methodology has been developed to allow accurate measurement of friction velocity in the field for smooth or quasi-smooth channel flows by obtaining an explicit relationship between

the freestream surface velocity U_m, viscosity ν, the channel depth h and the friction velocity U_*

4. Further, it has been shown that U_* has contribution from both outer scale velocity U_m and the inner scale velocity ν/h. This finding has implications for understanding inner-outer interactions in wall-bounded flows.
5. In computational fluid dynamics, it has been shown that the hitherto configuration of the widely popular $k-\epsilon$ model is incorrect. Such a configuration causes can cause early diffusion of tracers and numerical instability in finer meshes.
6. A new configuration of $k-\epsilon$ model has been suggested. A simple *a-posteriori* study demonstrates improved numerical stability of the code in the new configuration.
7. A new scaling law has been proposed to scale mean-velocity profiles in the wall-bounded flows. The new scaling law proves that at infinite Reynolds numbers, the profiles reach an asymptotic state.

The above findings significantly advance the state-of-the-art understanding of wall-bounded flows in smooth walls.

7.2 Future Work

The insights and methodologies detailed in this dissertation are developed for smooth boundary cases. The following would be valuable extensions of the work presented here:

- The design of the coupler suggested in chapter 2 can be further improved by streamlining the edges. While there may not be any significant improvement in measurements close to the wall, an improved coupler can improve the measurements close to the surface. The current design of coupler separates the flow due to sharp edges. A CFD study can also be conducted to obtain further details on the influence of the coupler on the flow.
- Development of flow remains a key concern for all laboratory flumes. In chapter 3, a mechanism to obtain fully developed flow, and a methodology to verify flow development has been illustrated for smooth walls. However, a similar methodology may be difficult for the rough

walls because DNS datasets for channel flows with rough walls at similar Reynolds numbers are not yet available. Further, the transition in the rough-bed channels may follow a mechanism different from that in smooth walls. Therefore, an exhaustive study to examine flow development in rough-wall channels after tripping the flow will be an invaluable contribution to the study of wall-bounded turbulent channel flows.

- A new methodology to estimate shear stress was developed in chapter 4. It is demonstrated that the friction velocity can be measured more effectively using the free-stream velocity and the depth of the flow. The inevitable opportunity is to extend the framework, i.e., leveraging free-stream velocity for obtaining the friction velocity U_*, to the rough walls. Rough walls introduce additional complexity due to flow separation caused by roughness elements, which must be incorporated in any future investigation. Such a contribution will improve the accuracy of bed-shear stress measurements in various natural channels.
- In chapter 5, it was shown that the current configuration of C_μ in the standard $k-\epsilon$ model is inappropriate. However, the values of C_μ could vary widely in other types of canonical flows. Therefore, more experimental and DNS data are required to obtain a universal value of C_μ. Further, merely changing C_μ to 0.06 might lead to inferior results because the other constants in the $k-\epsilon$ model have been tuned by fixing $C_\mu = 0.09$. Therefore, a wider comprehensive effort is required to re-tune the coefficients by setting C_μ to 0.06, which would be a natural extension of the work presented in this chapter.
- A new scaling law for wall-bounded flows has been proposed in chapter 6. The proposed scaling law is a significant improvement in the study of turbulent wall-bounded flows. While the inspiration for the work comes from the Lorentzian transformations, the exact mathematical dependence is currently not clear. Thus, a more mathematically rigorous explanation of the scaling law can help it extend to different wall configurations.

In summary, all the studies presented in this dissertation can be extended to the rough walls. Further, from the analytical perspective, a more generalizable and mathematically robust explanation of the semi-empirical relationships presented in this dissertation would be another relevant contri-

bution to the community. It will combine fluid mechanics, applied mathematics, and hydraulics engineering in a happy synergy to provide an elegant but comprehensive description of the flow phenomenon, which, in the words of Albert Einstein, will be *"simple, but not simpler."*[3]

[3]The exact quote is *"Everything should be made as simple as possible, but not simpler."*

Bibliography

Aberle, J., Rennie, C. D., Admiraal, D. M., and Muste, M. (2017). *Experimental Hydraulics: Methods, Instrumentation, Data Processing and Management: Volume II: Instrumentation and Measurement Techniques*. CRC Press.

Ackerman, J. D. and Hoover, T. M. (2001). Measurement of local bed shear stress in streams using a Preston-static tube. *Limnology and Oceanography*, 46(8):2080–2087.

Adrian, R. (1991). Particle-Imaging Techniques For Experimental Fluid-Mechanics. *Annual Review of Fluid Mechanics*, 23(1):261–304.

Adrian, R. J. and Westerweel, J. (2011). *Particle image velocimetry*. Number 30. Cambridge university press.

Amir, M., Nikora, V. I., and Stewart, M. T. (2014). Pressure forces on sediment particles in turbulent open-channel flow: A laboratory study. *Journal of Fluid Mechanics*, 757:458–497.

Bergeron, N. E. and Abrahams, A. D. (1992). Estimating shear velocity and roughness length from velocity profiles. *Water Resources Research*, 28(8):2155–2158.

Berk, T. and Coletti, F. (2020). Transport of inertial particles in high-Reynolds-number turbulent boundary layers. *Journal of Fluid Mechanics*, 903:18–19.

Biron, P. M., Lane, S. N., Roy, A. G., Bradbrook, K. F., and Richards, K. S. (1998). Sensitivity of bed shear stress estimated from vertical velocity profiles: The problem of sampling resolution. *Earth Surface Processes and Landforms*, 23(2):133–139.

Boikos, C., Siamidis, P., Oppo, S., Armengaud, A., Tsegas, G., Mellqvist, J., Conde, V., and Ntziachristos, L. (2024). Validating CFD modelling of ship plume dispersion in an urban environment with pollutant concentration measurements. *Atmospheric Environment*, 319:120261.

Bounds, C. P., Uddin, M., and Desai, S. (2023). Tuning of Turbulence Model Closure Coefficients Using an Explainability Based Machine Learning Algorithm. SAE Technical Paper 2023-01-0562, SAE International, Warrendale, PA. ISSN: 0148-7191, 2688-3627.

Bradshaw, P. (2013). *An introduction to turbulence and its measurement: thermodynamics and fluid mechanics series*. Elsevier.

Bradshaw, P., Ferriss, D. H., and Atwell, N. P. (1967). Calculation of boundary-layer development using the turbulent energy equation. *Journal of Fluid Mechanics*, 28(3):593–616. Publisher: Cambridge University Press.

Brandt, L. and Coletti, F. (2022). Particle-laden turbulence: progress and perspectives. *Annual Review of Fluid Mechanics*, 54(1):159–189.

Bush, R. H., Chyczewski, T. S., Duraisamy, K., Eisfeld, B., Rumsey, C. L., and Smith, B. R. (2019). Recommendations for future efforts in rans modeling and simulation. In *AIAA scitech 2019 forum*, page 0317.

Busse, F. H. (1970). Bounds for turbulent shear flow. *Journal of Fluid Mechanics*, 41(1):219–240.

Cameron, S. M., Nikora, V. I., and Stewart, M. T. (2017). Very-large-scale motions in rough-bed open-channel flow. *Journal of Fluid Mechanics*, 814:416–429.

Cameron, S. M., Nikora, V. I., and Witz, M. J. (2020). Entrainment of sediment particles by very large-scale motions. *Journal of Fluid Mechanics*, 888:A7.

Celik, I. (2003). RANS/LES/DES/DNS: The Future Prospects of Turbulence Modeling. *Journal of Fluids Engineering*, 127(5):829–830.

Champagne, F. H., Harris, V. G., and Corrsin, S. (1970). Experiments on nearly homogeneous turbulent shear flow. *Journal of Fluid Mechanics*, 41(1):81–139. Publisher: Cambridge University Press.

Chen, C. and He, L. (2023). Two-scale solution for tripped turbulent boundary layer. *Journal of Fluid Mechanics*, 955:A5.

Chen, X. and Sreenivasan, K. R. (2022). Law of bounded dissipation and its consequences in turbulent wall flows. *Journal of Fluid Mechanics*, 933:A20.

Chow, V. T. (1957). *Open-Channel Hydraulics*. Mcgraw International Book Company, Tokyo Japan.

Chow, V. T. (1959a). *Open-channel hydraulics*, volume 1. McGraw-Hill New York.

Chow, V. T. (1959b). *Open-channel hydraulics*. McGraw-Hill civil engineering series.

Clauser, F. H. (1954). Turbulent Boundary Layers in Adverse Pressure Gradients. *Journal of the Aeronautical Sciences*, 21(2):91–108.

Coleman, N. L. and Alonso, C. V. (1984). Two-dimensional channel flows over rough surfaces. *Journal of Hydraulic Engineering*, 110(7):1007–1008.

Coles, D. (1956). The law of the wake in the turbulent boundary layer. *Journal of Fluid Mechanics*, 1(2):191–226.

Corbett, D. M. (1943). Stream-gaging procedure, a manual describing methods and practices of the Geological Survey. Technical Report Water Supply 888, USGS.

Cotton, M., Graham, L., Ismael, J., and Launder, B. (1992). First steps in the use of strain and vorticity invariants in two-equation modelling. In *Proc. 5th Biennial CFD Colloquium UMIST*, volume 1, page 5.

Cotton, M. A. and Ismael, J. O. (1998). A strain parameter turbulence model and its application to homogeneous and thin shear flows. *International Journal of Heat and Fluid Flow*, 19(4):326–337.

Cox, D. T., Kobayashi, N., and Okayasu, A. (1996). Bottom shear stress in the surf zone. *Journal of Geophysical Research C: Oceans*, 101(C6):14337–14348.

Das, S., Balachandar, R., and Barron, R. M. (2022a). Effect of free surface perturbation on fully developed smooth open channel flow. *Journal of Hydraulic Research*, 60(3):363–375.

Das, S., Balachandar, R., and Barron, R. M. (2022b). Generation and characterization of fully developed state in open channel flow. *Journal of Fluid Mechanics*, 934:A35.

Deissler, R. G. (1950). Analytical and experimental investigation of adiabatic turbulent flow in smooth tubes. Technical report.

Delville, J., Chahine, Z., and Bonnet, J. P. (1987). Experimental Study of an Incompressible, Plane Mixing Layer by Temporal and Spectral Analysis. In Comte-Bellot, G. and Mathieu, J., editors, *Advances in Turbulence*, pages 435–444, Berlin, Heidelberg. Springer.

Diskin, B., Thomas, J. L., Rumsey, C. L., and Schwöppe, A. (2015). Grid Convergence for Turbulent Flows (Invited). *53rd AIAA Aerospace Sciences Meeting*.

Duraisamy, K., Iaccarino, G., and Xiao, H. (2019). Turbulence Modeling in the Age of Data. *Annual Review of Fluid Mechanics*, 51(1):357–377.

Durbin, P. and Shih, T.-P. (2005). An overview of turbulence modeling. In Sunden, B. and Faghri, M., editors, *WIT Transactions on State of the Art in Science and Engineering*, volume 1, pages 1–29. WIT Press, 1 edition. ISSN: 1755-8336.

Durbin, P. A. (2018). Some Recent Developments in Turbulence Closure Modeling. *Annual Review of Fluid Mechanics*, 50(Volume 50, 2018):77–103. Publisher: Annual Reviews.

Durbin, P. A. and Reif, B. A. P. (2011). *Statistical theory and modeling for turbulent flows*. Wiley, Chichester, West Sussex, 2nd ed edition. OCLC: ocn634739167.

Durst, F., Melling, A., and Whitelaw, J. H. (1981). *Principles and practice of laser-Doppler anemometry*. Number BOOK. Academic press.

Edeling, W. N., Cinnella, P., Dwight, R. P., and Bijl, H. (2014). Bayesian estimates of parameter variability in the k–ϵ turbulence model. *Journal of Computational Physics*, 258:73–94.

Eisfeld, B. (2021). Characteristics of Incompressible Free Shear Flows and Implications for Turbulence Modeling. *AIAA Journal*, 59(1):180–195. Publisher: American Institute of Aeronautics and Astronautics.

Eisfeld, B. (2022). The importance of turbulent equilibrium for Reynolds-stress modeling. *Physics of Fluids*, 34(2):025123.

Elsinga, G. E. and Westerweel, J. (2011). Tomographic-PIV measurement of the flow around a zigzag boundary layer trip. *Experiments in Fluids*, 52(4).

Emory, M., Larsson, J., and Iaccarino, G. (2013). Modeling of structural uncertainties in Reynolds-averaged Navier-Stokes closures. *Physics of Fluids*, 25(11):110822.

Ettema, R. (2006). Hunter Rouse—His Work in Retrospect. *Journal of Hydraulic Engineering*, 132(12):1248–1258. Publisher: American Society of Civil Engineers.

Fernholz, H. H., Janke, G., Schober, M., Wagner, P. M., and Warnack, D. (1996). New developments and applications of skin-friction measuring techniques. *Measurement Science and Technology*, 7(10):1396.

Foucaut, J.-M. and Stanislas, M. (2002). Some considerations on the accuracy and frequency response of some derivative filters applied to particle image velocimetry vector fields. *Measurement Science and Technology*, 13(7):1058.

Frei, D. and Thomann, H. (1980). Direct measurements of skin friction in a turbulent boundary layer with a strong adverse pressure gradient. *Journal of Fluid Mechanics*, 101(1):79–95.

Frostick, L., McLelland, S. J., Mercer, T. G., et al. (2011). *Users guide to physical modelling and experimentation - IAHR Design Manual*. CRC Press Taylor & Francis group Leiden.

Gaudio, R., Miglio, A., and Dey, S. (2010). Non-universality of von Kármán's κ in fluvial streams. *Journal of Hydraulic Research*, 48(5):658–663.

Guo, J. (2014). Modified log-wake-law for smooth rectangular open channel flow. *Journal of Hydraulic Research*, 52(1):121–128.

Guo, J. and Julien, P. Y. (2005). Shear Stress in Smooth Rectangular Open-Channel Flows. *Journal of Hydraulic Engineering*, 131(1):30–37.

Guo, J., Julien, P. Y., and Meroney, R. N. (2005). Modified log-wake law for zero-pressure-gradient turbulent boundary layers. *Journal of Hydraulic Research*, 43(4):421–430.

Gurka, R., Liberzon, A., Hefetz, D., Rubinstein, D., and Shavit, U. (1999). Computation of pressure distribution using piv velocity data. In *Workshop on particle image velocimetry*, volume 2, pages 1–6.

Hanjalic, K. (2005). Will RANS Survive LES? A View of Perspectives. *Journal of Fluids Engineering*, 127(5):831–839.

Haritonidis, J. H. (1989). The measurement of wall shear stress. In Gad-el-Hak, M., editor, *Advances in Fluid Mechanics Measurements*, pages 229–261. Springer Berlin Heidelberg, Berlin, Heidelberg.

Harlow, F. H. and Nakayama, P. I. (1968). Transport of turbulence energy decay rate. Technical report, Los Alamos National Lab.(LANL), Los Alamos, NM (United States).

Harris, V. G., Graham, J. a. H., and Corrsin, S. (1977). Further experiments in nearly homogeneous turbulent shear flow. *Journal of Fluid Mechanics*, 81(4):657–687. Publisher: Cambridge University Press.

Heo, S., Yun, Y., Jeong, M., and Jee, S. (2024). Simulation of supersonic axisymmetric base flow with a data-driven turbulence model. *Aerospace Science and Technology*, 147:109014.

Hoyas, S., Oberlack, M., Alcántara-Ávila, F., Kraheberger, S. V., and Laux, J. (2022). Wall turbulence at high friction Reynolds numbers. *Physical Review Fluids*, 7(1):014602.

Hutchins, N. and Marusic, I. (2007). Evidence of very long meandering features in the logarithmic region of turbulent boundary layers. *Journal of Fluid Mechanics*, 579:1–28.

Jiménez, J. (2013). Near-wall turbulence. *Physics of Fluids*, 25(10):101302.

Johnson, E. D. and Cowen, E. A. (2017). Estimating bed shear stress from remotely measured surface turbulent dissipation fields in open channel flows. *Water Resources Research*, 53(3):1982–1996.

Jones, W. and Launder, B. (1973). The calculation of low-Reynolds-number phenomena with a two-equation model of turbulence. *International Journal of Heat and Mass Transfer*, 16(6):1119–1130.

Jones, W. P. and Launder, B. E. (1972). The prediction of laminarization with a two-equation model of turbulence. *International Journal of Heat and Mass Transfer*, 15(2):301–314.

Karimpour, F. and Venayagamoorthy, S. K. (2013). Some insights for the prediction of near-wall turbulence. *Journal of Fluid Mechanics*, 723:126–139.

Karimpour, F. and Venayagamoorthy, S. K. (2014). A revisit of the equilibrium assumption for predicting near-wall turbulence. *Journal of Fluid Mechanics*, 760:304–312.

Kartha, V. C. and Leutheusser, H. J. (1970). Distribution of Tractive Force in Open Channels. *Journal of the Hydraulics Division*, 96(7):1469–1483.

Kim, J., Moin, P., and Moser, R. (1987). Turbulence statistics in fully developed channel flow at low Reynolds number. *Journal of Fluid Mechanics*, 177:133–166.

Klewicki, J. C. (2022). Bounded dissipation predicts finite asymptotic state of near-wall turbulence. *Journal of Fluid Mechanics*, 940:F1.

Kolmogorov, A. N. (1941). Equations of turbulent motion in an incompressible fluid. In *Dokl. Akad. Nauk SSSR*, volume 30, pages 299–303.

Kundu, P. K., Cohen, I. M., and Dowling, D. R. (2015). *Fluid mechanics*. Academic press.

Landreth, C. and Adrian, R. (1988). Measurement and refinement of velocity data using high image density analysis in particle image velocimetry. In *4th International Symposium on Applications of Laser Anemometry to Fluid Mechanics*, pages 6–14.

Latzko, H. (1944). Heat transfer in a turbulent liquid or gas stream. *Zeitschrift für angewandte Mathematik und Mechanik*, 1(NACA-TM-1068).

Launder, B., Morse, A., Rodi, W., and Spalding, D. (1973). Prediction of free shear flows: a comparison of the performance of six turbulence models. *NASA. Langley Res. Center Free Turbulent Shear Flows, Vol. 1*.

Launder, B. and Spalding, D. (1974). The numerical computation of turbulent flows. *Computer Methods in Applied Mechanics and Engineering*, 3(2):269–289.

Launder, B. E. and Sharma, B. I. (1974). Application of the energy-dissipation model of turbulence to the calculation of flow near a spinning disc. *Letters in Heat and Mass Transfer*, 1(2):131–137.

Lee, K., Ho, H. C., Marian, M., and Wu, C. H. (2014). Uncertainty in open channel discharge measurements acquired with StreamPro ADCP. *Journal of Hydrology*, 509:101–114.

Lee, M. and Moser, R. D. (2015). Direct numerical simulation of turbulent channel flow up to $Re\tau \approx 5200$. *Journal of Fluid Mechanics*, 774:395–415.

Lefantzi, S., Ray, J., Arunajatesan, S., and Dechant, L. (2014). Estimation of k-ϵ parameters using surrogate models and jet-in-crossflow data. Technical Report SAND2015-0707, Sandia National Lab. (SNL-CA), Livermore, CA (United States); Sandia National Lab. (SNL-NM), Albuquerque, NM (United States).

Li, C.-H. (1965). Turbulent Flow in the Entry Region. *Theses and Dissertations*.

Li, J.-P., Tang, D.-G., Yi, C., and Yan, C. (2022). Data-augmented turbulence modeling by reconstructing Reynolds stress discrepancies for adverse-pressure-gradient flows. *Physics of Fluids*, 34(4):045110.

Lien, K., Monty, J., Chong, M., and Ooi, A. (2004). The Entrance Length for Fully Developed Turbulent Channel Flow.

Ling, J., Kurzawski, A., and Templeton, J. (2016). Reynolds averaged turbulence modelling using deep neural networks with embedded invariance. *Journal of Fluid Mechanics*, 807:155–166.

Ling, J. and Templeton, J. (2015). Evaluation of machine learning algorithms for prediction of regions of high Reynolds averaged Navier Stokes uncertainty. *Physics of Fluids*, 27(8):085103.

Mauritsen, T., Svensson, G., Zilitinkevich, S. S., Esau, I., Enger, L., and Grisogono, B. (2007). A Total Turbulent Energy Closure Model for Neutrally and Stably Stratified Atmospheric Boundary Layers. *Journal of the Atmospheric Sciences*, 64(11):4113–4126. Publisher: American Meteorological Society Section: Journal of the Atmospheric Sciences.

Mazarakis, N., Kaloudis, E., Nazos, A., and Nikas, K.-S. P. (2016). Les and rans comparison of flow and pollutant dispersion in urban environment. *International Journal of Environmental Studies*, 73(1):48–65.

Mishra, H. and Venayagamoorthy, S. K. (2024). New Method to Calculate Friction Velocity in Smooth Channel Flows Using Direct Numerical Simulation Data. *Journal of Hydraulic Engineering*, 150(4):04024019.

Monkewitz, P. A. (2022). Asymptotics of streamwise Reynolds stress in wall turbulence. *Journal of Fluid Mechanics*, 931:A18.

Morlock, S. E. (1996). Evaluation of Acoustic Doppler Current Profiler Measurements of River Discharge. *U.S. Geological Survey Water-Resources Investigations Report 95–4218*, page 37.

Morrison, J. F. (2007). The interaction between inner and outer regions of turbulent wall-bounded flow. *Philosophical Transactions of the Royal Society A: Mathematical, Physical and Engineering Sciences*, 365(1852):683–698.

Muste, M., Lyn, D. A., Admiraal, D., Ettema, R., Nikora, V., and García, M. H. (2017). *Experimental Hydraulics: Methods, Instrumentation, Data Processing and Management: Volume I: Fundamentals and Methods*. CRC Press.

Muste, M., Yu, K., Pratt, T., and Abraham, D. (2004). Practical aspects of ADCP data use for quantification of mean river flow characteristics; Part II: Fixed-vessel measurements. *Flow Measurement and Instrumentation*, 15(1):17–28.

Nagib, H. M. and Chauhan, K. A. (2008). Variations of von Kármán coefficient in canonical flows. *Physics of Fluids*, 20(10):101518.

Nezu, I. and Nakagawa, H. (2017). *Turbulence in open-channel flows*. Routledge.

Nezu, I. and Rodi, W. (1986). Open-channel Flow Measurements with a Laser Doppler Anemometer. *Journal of Hydraulic Engineering*, 112(5):335–355.

Nikora, V., Nokes, R., Veale, W., Davidson, M., and Jirka, G. H. (2007). Large-scale turbulent structure of uniform shallow free-surface flows. *Environmental Fluid Mechanics*, 7(2):159–172.

Pan, S. and Duraisamy, K. (2018). Data-Driven Discovery of Closure Models. *SIAM Journal on Applied Dynamical Systems*, 17(4):2381–2413. Publisher: Society for Industrial and Applied Mathematics.

Patel, N., Mohebbi, A., Jan, C.-D., and Guo, J. (2020). Maximum Shear-Stress Method for Stable Channel Design. *Journal of Hydraulic Engineering*, 146(12):04020082.

Pieterse, A., Puleo, J. A., McKenna, T. E., and Aiken, R. A. (2015). Near-bed shear stress, turbulence production and dissipation in a shallow and narrow tidal channel. *Earth Surface Processes and Landforms*, 40(15).

Pope, N. D., Widdows, J., and Brinsley, M. D. (2006). Estimation of bed shear stress using the turbulent kinetic energy approach-A comparison of annular flume and field data. *Continental Shelf Research*, 26(8):959–970.

Pope, S. B. (2000). *Turbulent flows*. Cambridge university press.

Poroseva, S. V., Colmenares F., J. D., and Murman, S. M. (2016). On the accuracy of RANS simulations with DNS data. *Physics of Fluids*, 28(11):115102.

Prandtl, L. (1945). Ueber ein neues formelsystem fur die ausgebildete turbulenz. nach. ges. wiss. gottingen, math. *Phys. Kl*, pages 6–18.

Prooijen, B., Booij, R., and Uijttewaal, W. (2000). Measurement and analysis methods of large scale horizontal coherent structures in a wide shallow channel.

Raffel, M., Willert, C. E., Scarano, F., Kähler, C. J., Wereley, S. T., and Kompenhans, J. (2018). *Particle image velocimetry: a practical guide*. Springer.

Raju, K. G. R., Asawa, G. L., and Mishra, H. K. (2000). Flow-Establishment Length in Rectangular Channels and Ducts. *Journal of Hydraulic Engineering*, 126(7):533–539.

Raupach, M. R., Thom, A. S., and Edwards, I. (1980). A wind-tunnel study of turbulent flow close to regularly arrayed rough surfaces. *Boundary-Layer Meteorology*, 18(4):373–397.

Replogle, J. A. and Chow, V. T. (1966). Tractive-Force Distribution in Open Channels. *Journal of the Hydraulics Division*, 92(2):169–191.

Reynolds, W. (1987). Fundamentals of turbulence for turbulence modeling and simulation. *Lecture Notes for Von Karman Institute Agard Report*, 755:005793.

Rodi, W. (1972). The prediction of free turbulent boundary layers by use of a two-equation model of turbulence. *Ph. D. Thesis, University of London*.

Rodi, W. (2017). Turbulence Modeling and Simulation in Hydraulics: A Historical Review. *Journal of Hydraulic Engineering*, 143(5):03117001. Publisher: American Society of Civil Engineers.

Rouse, H. (1946). Elementary mechanics of fluids. *(No Title)*.

Rousseau, G. and Ancey, C. (2020). Scanning piv of turbulent flows over and through rough porous beds using refractive index matching. *Experiments in Fluids*, 61(8):1–24.

Schrijer, F., Scarano, F., and Van Oudheusden, B. (2006). Application of piv in a mach 7 double-ramp flow. *Experiments in fluids*, 41(2):353–363.

Schultz, M. P. and Flack, K. A. (2013). Reynolds-number scaling of turbulent channel flow. *Physics of Fluids*, 25(2).

Shayan, H. K., Farhoudi, J., and Vatankhah, A. (2021). Experimental and field verifications of radial gates as flow measurement structures. *Water Supply*.

Shih, T.-H., Liou, W. W., Shabbir, A., Yang, Z., and Zhu, J. (1994). A New K-epsilon Eddy Viscosity Model for High Reynolds Number Turbulent Flows: Model Development and Validation. Technical Report CMOTT-94-6. NTRS Author Affiliations: NASA Lewis Research Center NTRS Document ID: 19950005029 NTRS Research Center: Legacy CDMS (CDMS).

Shih, T.-H., Liou, W. W., Shabbir, A., Yang, Z., and Zhu, J. (1995). A new k-ϵ eddy viscosity model for high reynolds number turbulent flows. *Computers & Fluids*, 24(3):227–238.

Silvestri, A., Ghanadi, F., Arjomandi, M., Cazzolato, B., and Zander, A. (2017). The Application of Different Tripping Techniques to Determine the Characteristics of the Turbulent Boundary Layer Over a Flat Plate. *Journal of Fluids Engineering*, 140(011204).

Sime, L. C., Ferguson, R. I., and Church, M. (2007). Estimating shear stress from moving boat acoustic Doppler velocity measurements in a large gravel bed river. *Water Resources Research*, 43(3).

Simpson, M. and Oltmann, R. (1993). Discharge-measurement system using an acoustic Doppler current profiler with applications to large rivers and estuaries.

Sinclair, J. M., Venayagamoorthy, S. K., and Gates, T. K. (2022). Some Insights on Flow over Sharp-Crested Weirs Using Computational Fluid Dynamics: Implications for Enhanced Flow Measurement. *Journal of Irrigation and Drainage Engineering*, 148(6):04022011. Publisher: American Society of Civil Engineers.

Smits, A. J., McKeon, B. J., and Marusic, I. (2011). High–Reynolds Number Wall Turbulence. *Annual Review of Fluid Mechanics*, 43(1):353–375.

Sotgiu, C., Weigand, B., Semmler, K., and Wellinger, P. (2019). Towards a general data-driven explicit algebraic Reynolds stress prediction framework. *International Journal of Heat and Fluid Flow*, 79:108454.

Suga, K. (1995). *Development and Application of a Non-Linear Eddy-Viscosity Model Sensitized to Stress and Strain Invariants*. Ph.D., The University of Manchester (United Kingdom), England. ISBN: 9798426841444.

Tavoularis, S. and Corrsin, S. (1981). Experiments in nearly homogenous turbulent shear flow with a uniform mean temperature gradient. Part 1. *Journal of Fluid Mechanics*, 104:311–347. Publisher: Cambridge University Press.

Townsend, A. (1976). *The structure of turbulent shear flow*. Cambridge university press.

Townsend, A. A. (1951). The structure of the turbulent boundary layer. *Mathematical Proceedings of the Cambridge Philosophical Society*, 47(2):375–395.

Townsend, A. A. (1961). Equilibrium layers and wall turbulence. *Journal of Fluid Mechanics*, 11(1):97–120.

Vassilicos, J. C. (2015). Dissipation in Turbulent Flows. *Annual Review of Fluid Mechanics*, 47(1):95–114. _eprint: https://doi.org/10.1146/annurev-fluid-010814-014637.

Victoria, M. A. J. and Caja, M. S. (2010). An introduction to lorentzian geometry and its applications. *XVI Escola de Geometria Diferencial, IME, USP*.

Viollet, P.-L. (2017). *Water Engineering inAncient Civilizations: 5,000 Years of History*. CRC Press.

Volino, R. J. and Schultz, M. P. (2018). Determination of wall shear stress from mean velocity and Reynolds shear stress profiles. *Physical Review Fluids*, 3(3):034606.

Wang, J.-X., Sun, R., and Xiao, H. (2016). Quantification of uncertainties in turbulence modeling: A comparison of physics-based and random matrix theoretic approaches. *International Journal of Heat and Fluid Flow*, 62:577–592.

Wang, J.-X., Wu, J.-L., and Xiao, H. (2017). Physics-informed machine learning approach for reconstructing Reynolds stress modeling discrepancies based on DNS data. *Physical Review Fluids*, 2(3):034603. Publisher: American Physical Society.

Wang, Y., Lam, K. M., and Lu, Y. (2018). Settling velocity of fine heavy particles in turbulent open channel flow. *Physics of Fluids*, 30(9):095106.

Westerweel, J., Elsinga, G. E., and Adrian, R. J. (2013). Particle image velocimetry for complex and turbulent flows. 45:409–436.

Wilcock, P. R. (1996). Estimating local bed shear stress from velocity observations. *Water Resources Research*, 32(11):3361–3366.

Wilkerson, G., Sharma, S., and Sapkota, D. (2019). Length for Uniform Flow Development in a Rough Laboratory Flume. *Journal of Hydraulic Engineering*, 145(1):06018018.

Wilson, B. M. and Smith, B. L. (2013). Uncertainty on piv mean and fluctuating velocity due to bias and random errors. *Measurement Science and Technology*, 24(3):035302.

Wilson, J. M. and Venayagamoorthy, S. K. (2015). A Shear-Based Parameterization of Turbulent Mixing in the Stable Atmospheric Boundary Layer. *Journal of the Atmospheric Sciences*, 72(5):1713–1726.

Womack, K. M., Meneveau, C., and Schultz, M. P. (2019). Comprehensive shear stress analysis of turbulent boundary layer profiles. *Journal of Fluid Mechanics*, 879:360–389.

Xiong, M., Chen, B., Zhang, H., and Qian, Y. (2022). Study on Accuracy of CFD Simulations of Wind Environment around High-Rise Buildings: A Comparative Study of k-ϵ Turbulence Models Based on Polyhedral Meshes and Wind Tunnel Experiments. *Applied Sciences*, 12(14):7105. Number: 14 Publisher: Multidisciplinary Digital Publishing Institute.

Xu, J., Sun, G., and Xu, D. (2020). Distribution of stress intensity ratio in canonical turbulent flows and converging-diverging channel. *Acta Astronautica*, 166:342–349.

Yakhot, V. and Orszag, S. A. (1986). Renormalization group analysis of turbulence. I. Basic theory. *Journal of Scientific Computing*, 1(1):3–51.

Yan, C., Zhang, Y., and Chen, H. (2022). Data augmented turbulence modeling for three-dimensional separation flows. *Physics of Fluids*, 34(7):075101.

Yang, S.-Q. (2010). Depth-Averaged Shear Stress and Velocity in Open-Channel Flows. *Journal of Hydraulic Engineering*, 136(11):952–958.

Yao, J., Chen, X., and Hussain, F. (2022). Direct numerical simulation of turbulent open channel flows at moderately high Reynolds numbers. *Journal of Fluid Mechanics*, 953:A19.

Ye, Q., Schrijer, F. F. J., and Scarano, F. (2018). On Reynolds number dependence of micro-ramp-induced transition. *Journal of Fluid Mechanics*, 837:597–626.

Yen, B. C. (2002). Open Channel Flow Resistance. *Journal of Hydraulic Engineering*, 128(1):20–39. Publisher: American Society of Civil Engineers.

Zagarola, M. V. and Smits, A. J. (1998). Mean-flow scaling of turbulent pipe flow. *Journal of Fluid Mechanics*, 373:33–79.

Zampiron, A., Cameron, S., and Nikora, V. (2021). Momentum and energy transfer in open-channel flow over streamwise ridges. *Journal of Fluid Mechanics*, 915:A42.

Zampiron, A., Cameron, S. M., Stewart, M. T., Marusic, I., and Nikora, V. I. (2023). Flow development in rough-bed open channels: Mean velocities, turbulence statistics, velocity spectra, and secondary currents. *Journal of Hydraulic Research*, 61(1):133–144.

ZJ You, B. Y. (2007). Direct measurement of bottom shear stress under water waves. *J Coast Res*, SI 50:1132–1136.